High-Throughput Screening of High-Entropy Alloys for Advanced Nuclear Applications

By

Michael Moorehead

A dissertation submitted in partial fulfillment of

the requirements for the degree of

Doctor of Philosophy

(Nuclear Engineering and Engineering Physics)

at the

UNIVERSITY OF WISCONSIN-MADISON

2021

Date of final oral examination: 10/27/2021

The dissertation is approved by the following member of the Final Oral Committee:

Adrien Couet, Associate Professor, Engineering Physics
Dane Morgan, Professor, Materials Science and Engineering
John Perepezko, Professor, Materials Science and Engineering
Kumar Sridharan, Professor, Engineering Physics
Dan Thoma, Professor, Materials Science and Engineering

Abstract

New materials, including high-entropy alloys (HEAs), are being investigated to satisfy demanding requirements for next-generation nuclear reactors. Unfortunately, the alloy discovery and development process for nuclear materials is prohibitively slow, even relative to other industries. This work covers the development and application of new high-throughput techniques to synthesize, irradiate, and characterize novel alloys for such applications. Using a LENS MR-7 directed energy deposition (DED) 3D metal printer, a process is developed in which alloys of arbitrary compositions are rapidly produced in regular arrays of "bulk" coupons. These compositional arrays have been heat treated and mechanically polished in parallel before being irradiated with heavy ions at the University of Wisconsin-Madison Ion Beam Laboratory (IBL). To accommodate the large sample arrays, an automated high-throughput irradiation system was developed and installed in the IBL, equipped with an IR laser to locally heat individual samples, which has since been used to irradiate nearly 100 samples to end-of-life damage levels for core components in proposed advanced reactors. Using automated nanoindentation and optical profilometry, the hardening and swelling of many Cr-Fe-Mn-Ni HEAs has been measured and trends in the irradiation response as a function of composition are examined. Of the elements in the Cr-Fe-Mn-Ni system, Cr and Ni appear to affect the swelling behavior most predominantly, with swelling increasing monotonically with increasing Cr concentration while swelling increases with Ni concentration up to ~30 at% before rapidly dropping with continued Ni additions until approaching pure Ni. Trends in swelling behavior are in good agreement with previous ion irradiation studies of Cr-Fe-Ni alloys in literature, which also serves to validate the overall high-throughput methodology employed in this work. Using the techniques described herein, immense time savings over traditional techniques are realized such that a single compositional array of 25 alloy coupons can by synthesized, heat treated, mechanically polished, irradiated, and characterized in less than a week.

Acknowledgements

First and foremost, I would like to thank my parents – were it not for them, I would not be here to write these acknowledgements. Whether through nature or nurture, they are ultimately responsible for the intellectual curiosity I carry with me today and have always gone out of their way to support my ambitions. In a similar vein, I would like to thank my wife, Samantha, who has been by my side for more than 10 years and made sacrifices to follow me halfway across the country to a new state for me to pursue higher education, all while tolerating my twisted sense of humor. For my family, by blood and by law, I am grateful.

However, familial gratitude alone is insufficient to progress the field of nuclear materials research, and in that endeavor, I must also extend my sincere thanks to my advisor, Adrien Couet. From day one, Adrien has provided professional and personal support to each of his students, working tirelessly to foster an environment which produces a deeper appreciation and fundamental understanding of the physical phenomena which govern our universe. Adrien has been able to strike a delicate balance of challenging each of his students while maintaining a candor and openness to new ideas that promotes innovative thinking and engineering, and I cherish my time as a member of his research group.

Of course, research does not occur in a vacuum – at least not in the metaphorical sense – and in my time at UW-Madison I have had the pleasure of working alongside countless talented minds of all ages, including every member, past and present, of the MaDCoR research group as well as each of my committee members: Kumar Sridharan, Dan Thoma, John Perepezko, Dane Morgan, and the members of each of their research groups. Were I to list the individual names and deeds of each colleague who I have shared a positive experience with, I would have enough material to write an additional dissertation, so instead, I beg your forgiveness as I extend my heartfelt gratitude to each of you collectively: thank you.

Table of Contents

List of Tables

List of Figures

Nomenclature

AM – additive manufacturing

BCC – body-centered cubic

CALPHAD – calculation of phase diagrams

CCA – complex concentrated alloy

CTF- combinatorial thin film

DED – directed energy deposition

DPA – displacements per atom

EBR-II – Experimental Breeder Reactor II

EDM – electric-discharge machining

EDS – energy-dispersive X-ray spectroscopy

FCC – face-centered cubic

FIB – focused ion beam

HCP – hexagonal close-packed

HEA – high entropy alloy

HIP – hot isostatic pressing

HTP -high-throughput

HTS – high-throughput screening

IBL – (UW-Madison) Ion Beam Laboratory

IR – infrared

KP – Kinchen-Pease (model)

LENS – laser engineered net shaping

LWR – light-water reactor

MD – molecular dynamics

ODS – oxide-dispersion strengthened

PID – proportional-integral-derivative (control)

PKA – primary knock-on atom

PWR – pressurized-water reactor

RIS – radiation-induced segregation

RPM – revolutions per minute

SEM – scanning electron microscopy

SFR – sodium-cooled fast-neutron reactor

SIA – self-interstitial atom

TEM – transmission electron microscopy

TWR -travelling wave reactor

XRD – X-ray diffraction

XRF – X-ray fluorescence

1 Background and Motivation

1.1 World Energy Landscape

The year 2020 was defined by the spread of a novel coronavirus (SARS-COV-2) – a virus which can attack the human respiratory system and cause a variety of symptoms with possibly deadly consequences as part of a disease collectively known as COVID-19. COVID-19 has touched every country in the world, causing many countries to close their boarders, limit transportation, and impose nationwide lockdowns while individuals are either encouraged or mandated to wear masks, socially distance, and work remotely to prevent the spread of the virus. As of this writing, the World Health Organization (WHO) reports the more than 4.5 million people have died from COVID-19 and associated complications since the onset of the pandemic [1], while the Centers for Disease Control (CDC) reports more than 650,000 people have died within the United States alone [2]. Yet, despite this shock to the global system, requiring governments to take sometimes draconian measures and citizens to make drastic changes to their day-to-day lives, global energy demand and CO_2 emissions only decreased by 4% and 6%, respectively, and both are expected to rebound to pre-pandemic levels by the end of 2021 [3]. This limited decline and rapid recovery of energy demand and CO_2 emission serves as a testament to the resilience of humans in the face of both changing and adverse conditions; however, it also serves as a foreboding reminder of the extent of human dependence on carbon-intensive energy resources and the magnitude of the changes required to curb anthropogenic climate change. The Intergovernmental Panel on Climate Change (IPCC), the United Nations (UN) body dedicated to assessing the scientific basis of climate change, has stated that the near-linear relationship between cumulative CO_2 emissions and maximum global surface temperature implies that stabilizing human-induced global temperature increase requires reducing CO_2 emissions to net zero [4]. Thus, even the collective international response to the COVID-19 pandemic is dwarfed by the changes required to address the ongoing climate crisis.

As the world population grows, more developing countries are becoming industrialized and more developed countries are becoming increasingly electrified, driven in part by an increasingly computer-centric economy, ubiquity of consumer electronics, and electric ground transportation growth which collectively lead to an increase in electricity demand even as more efficient technologies are implemented [3]. However, even under the threat of global climate change, the vast majority of the added electricity capacity since the turn of the century has been produced by burning additional carbonaceous fuels, primarily natural gas, thereby producing more greenhouse gas emissions. While renewable resources such as wind and solar power are capable of producing electricity without CO_2 emissions once constructed, their generation intermediacy and their requisite geographic footprint intrinsically limit their usability for large scale power generation, at least without substantial advances in energy storage technologies.

In comparison to solar and wind, nuclear power offers the ability to generate large amounts of power continuously and while actually producing *less* greenhouse emissions. Figure 1 shows the greenhouse gas emission lifecycle assessment for various types of power generation systems [5]. Even when accounting for power plant construction, operation, and decommissioning as well as upstream and downstream processes including exploration, extraction, processing, waste treatment, disposal, and indirect emissions from manufacturing of materials and infrastructure, nuclear power produces the least greenhouse gas emissions per unit energy of nearly every power source, with the exception of run-of-river hydroelectric (i.e., no major reservoirs).

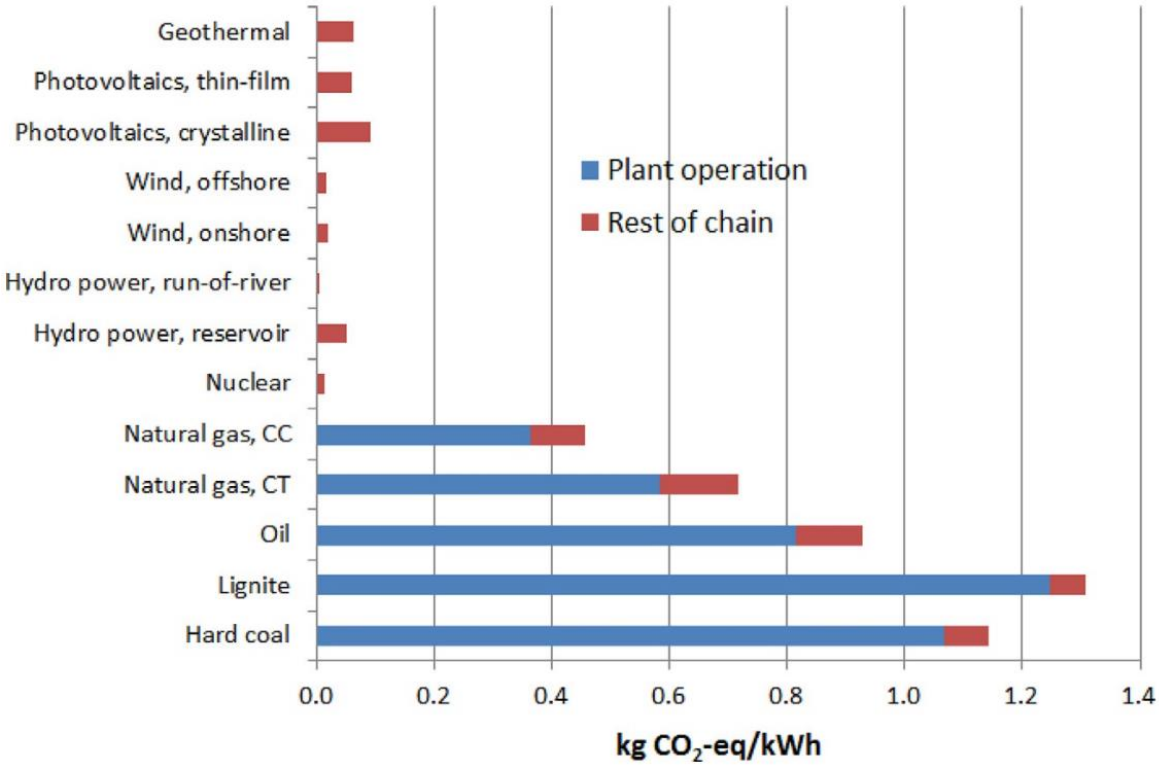

Figure 1*: Greenhouse gas emissions from power plant operation and from the rest of chain for different electricity generation systems kg of CO_2-equivalents (100 years) per kWh_e. Emissions total includes power plant construction, operation, and decommissioning as well as upstream and downstream processes including exploration, extraction, processing, waste treatment, disposal, and indirect emissions from manufacturing of materials and infrastructure [5].*

Much like wind and solar, the greenhouse gas emissions of nuclear are not directly emitted as part of the power generation process, rather they are primarily the result of the initial energy expended to construct the power plant and produce the nuclear fuel. Of all the energy expended to produce a nuclear fuel assembly, more than 70% is attributed to the uranium enrichment process [6]. Natural uranium typically contains ~0.72% ^{235}U by mass, which is fissile (easily fissioned by slow neutrons) with the remainder consisting almost entirely of ^{238}U, which is merely fissionable (only capable of undergoing fission from fast neutrons) [7]. While it is possible to construct nuclear reactors which operate using natural uranium, reactor designs can be simplified and shrunken by increasing the concentration of ^{235}U in the fuel element via enriching. Since different isotopes of uranium have identical chemical properties, rendering all chemical separations techniques useless, enrichment requires exploiting the minute difference in mass between the ^{235}U and ^{238}U nuclei, which typically requires largescale energy-intensive processes. The most widely used

method for enriching uranium at present is the use of gas centrifuges, wherein gaseous UF_6 is loaded and spun at incredible speeds. Since fluorine is a monoisotopic element, the difference in mass between UF_6 molecules is attributable only to differences in the mass of the uranium atoms they contain. Thus, as the gas centrifuges spin, the heavier ^{238}U-bearing molecules are pushed preferentially to the periphery of the centrifuge while the lighter ^{235}U-bearing molecules preferentially migrate inward where it can be separated. However, this centrifugal driving force is largely counteracted by the entropic tendency of gases to mix so the separation efficiency of a single centrifuge is vanishingly small, requiring large arrays of centrifuges to be running in series in order to achieve sufficiently high enrichment for use in commercial light-water reactors (LWRs). Such energy-intensive processing is what accounts for the majority of greenhouse gas emissions from nuclear power generation – assuming the electricity being used to run the enrichment facility is being produced by fossil fuels, which is the case for most countries.

It remains possible to reduce the need for enriching new uranium, however this requires the reprocessing/recycling of spent nuclear fuel which has been effectively banned at the commercial scale in the United States since 1977 due to proliferation concerns [8]. Over the lifecycle of a nuclear fuel rod inside a reactor, much of the ^{235}U, so painstakingly enriched, goes unfissioned and a substantial portion of the ^{238}U has been transmuted into fissile transuranic (i.e., beyond U on the periodic table) isotopes which themselves can be used to sustain a nuclear chain reaction. Through reprocessing, uranium and other fissile transuranic isotopes can be chemically separated from the spent fuel and be blended with fresh uranium to be fabricated into new fuel rods, reducing the need for new uranium enrichment while also greatly reducing the decay time needed for the activity of spent nuclear fuel to decay back down to that of natural uranium - less than a thousand years versus several hundred thousand years. To illustrate this, Figure 2 shows the predicted activity of spent nuclear fuel constituents over a period of one million years [9]. In the first ~100 years after a spent nuclear fuel rod is removed, the total radioactivity of the rod is dominated by contributions from fission products and activation products. However, shortly after this time, the radioactivity from the fission products drops precipitously and the remaining radioactivity of the spent fuel rod is attributed to the

presence of actinides (elements 89-103), and their daughter isotopes, which originated from the transmutation of ^{238}U during normal reactor operation. Thus, if the actinides are removed from the spent fuel, the long-term storage requirements for spent nuclear fuel are greatly reduced and the actinides themselves can be used as new fuel for a nuclear reactor where their fissioning will produce more energy than that which was required to chemically separate them.

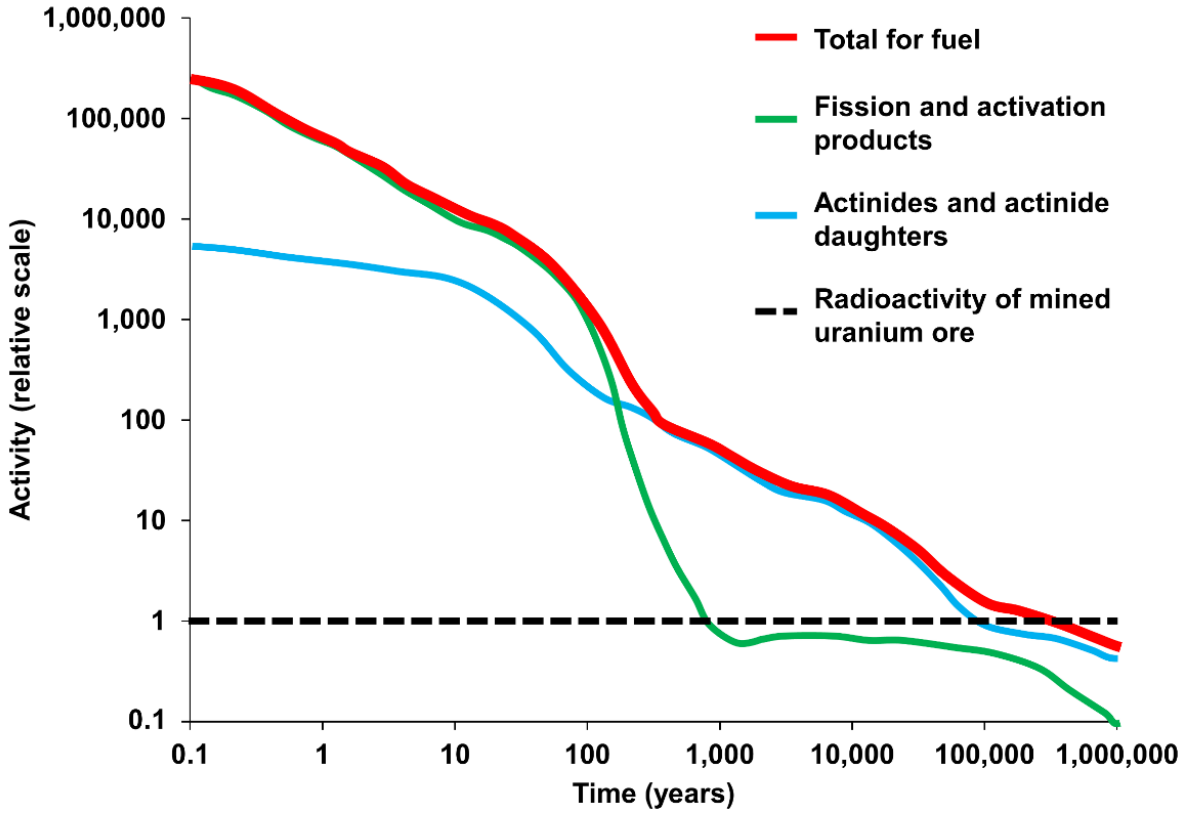

Figure 2*: Relative activity of spent nuclear fuel of type SVEA 64 with a burnup of 38 MWd/kg U. The activity is dominated during the first 100 years by fission products, thereafter by actinides. Adapted from [9].*

While many of the actinide isotopes present in spent fuel can be readily fissioned using neutrons of nearly any speed (e.g., ^{239}Pu, ^{241}Pu, ^{245}Cm), many of the other actinides require neutrons moving above a certain speed to be readily fissioned (e.g., ^{240}Pu, ^{241}Am, ^{243}Am) [10]. To efficiently fission these isotopes, nuclear reactors which operate primarily using fast neutrons are necessary. Since the fission probability (i.e., cross section) of many actinide isotopes increases substantially when interacting with slower moving

neutrons, as is the case for ^{235}U, nearly all commercial nuclear reactors today are designed to quickly slow down neutrons born from fission down to energy levels comparable to the thermal vibrations of the surround reactor materials (~0.025 eV). To produce a large population of these *thermal* neutrons, such reactors typically are filled with low-Z moderating materials, such as water and graphite, which can efficiently reduce the energy of interacting neutrons with only a few scattering events as compared to heavier materials such as steel or lead. However, advanced reactor designs using *fast* neutrons have been demonstrated as early as 1951 [11]. Rather than slow down neutrons through the use of moderators, fast-neutron reactors operate with neutron energies averaging near 2 MeV, which enables the fissioning of all relevant actinide isotopes with net energy gain. Since water is not usable as a primary coolant for such reactors, as it would serve to moderate the neutron population, fast-neutron reactors use other coolants such as molten sodium, molten lead, molten salts (fluorides and chlorides), and helium. The use of such coolants allows fast-neutron reactors to achieve substantially higher operating temperatures, and thus higher Carnot efficiencies, than their water-cooled counterparts all while operating at near atmospheric pressure, thus improving safety margins. Moreover, fast-neutron reactors can be made passively safe as exemplified by the EBR-II reactor, a sodium-cooled fast-neutron reactor which in 1985 was demonstrated to passively shut itself down from full power, without operator or automated intervention, following a simulated station blackout and critical systems failure including loss of power to the primary pumps, loss of power to the secondary pumps, loss of power to the auxiliary pumps, and loss of coolant flow, all while the reactor scram mechanism was disabled [12].

While advanced fast-neutron reactors boast improved efficiencies, passive safety mechanisms, and the ability to recycle spent nuclear fuel from the current reactor fleet, they are not without their drawbacks. Firstly, the most practical drawback is cost. In addition to the large upfront investments and the regulatory red tape traditional reactors are subject to, advanced reactors suffer from a lack of established supply chain for reactor components and greater regulatory scrutiny/uncertainty since the U.S. Nuclear Regulatory Commission (NRC) only has experience in the licensing of LWRs. Moreover, advanced reactors require

subjecting materials to much harsher environments than LWRs in the current fleet, and few materials are certified to operate such conditions, which consequently is the focus of the next section.

1.2 Material Challenges in Nuclear Environments

Nearly all baseload power plants have the same basic principles of operation – produce heat, boil water, spin turbine, produce electricity – with the exception of hydropower which uses the potential energy of water to spin a turbine while it remains in its liquid state. Rather than burning hydrocarbons to produce heat (or extracting heat from underground in the case of geothermal), nuclear power production relies on bringing large quantities of fissile material into close proximity with one another such that the fissioning of one atom, producing 2-3 free neutrons, leads to exactly one additional atom fissioning with the remaining neutrons either escaping the reactor or being absorbed elsewhere within the reactor. Managing the neutron economy within the reactor is thus vital for safe and reliable reactor operation, and care must be taken in choosing which materials to construct a reactor out of since different materials can have vastly different interactions with neutrons. Figure 3 shows a schematic of a pressurized-water reactor (PWR), common within the U.S. reactor fleet, with the different materials used in each subsystem indicated. While most of the structural materials consist of various grades of stainless steel, note that within the reactor core, the fuel claddings are constructed out of zirconium alloys – rarely used in any other industrial application. The use of Zr-based alloys is motivated by management of the neutron economy. As neutrons are slowed down through moderation in the reactor, the probability of the neutron being absorbed increases with decreasing velocity (~1/v), ignoring any resonances. This means that in order to ensure at least one neutron from each fission is able to go on and trigger another fission before being absorbed, materials within the core that separate the fuel elements must be as transparent as possible. As it so happens, ^{90}Zr, the most predominant Zr isotope, has both a full proton and neutron shell (Z=40, N=50), where 40 is considered a semi-magic number and 50 a magic number [13], in the nuclear physics sense. As such, with its full nuclear shells, it is not energetically favorable for ^{90}Zr to gain an additional neutron and thus the neutron absorption cross section for ^{90}Zr is miniscule (~0.1 barns) compared to many other elements.

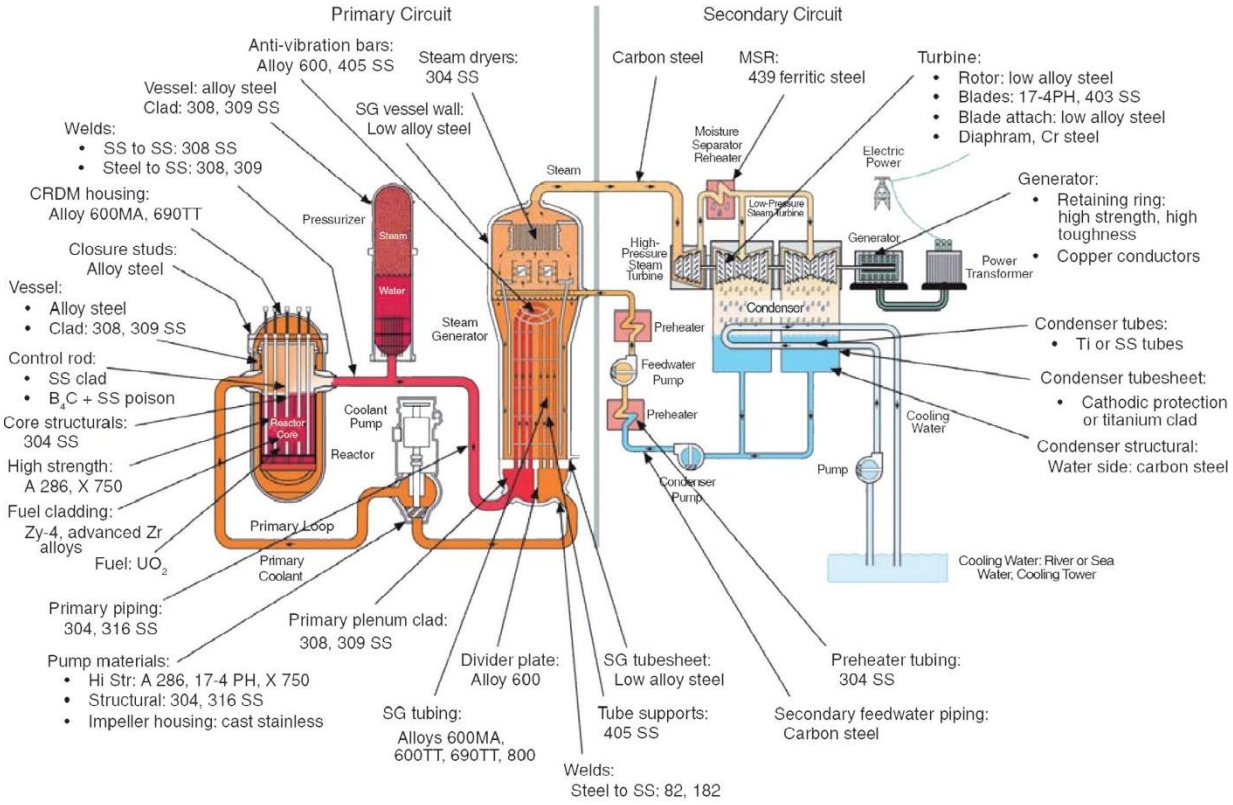

***Figure 3**: Diagram of pressurized-water reactor (PWR) showing material selections made for each subsystem [14].*

Though Zr stands out for its low neutron capture cross section, it also has some serious shortcomings for a structural material. Most notably, pure Zr has abysmal corrosion resistance in an aqueous environment requiring it to be alloyed with other elements to provide enough corrosion resistance for use in a nuclear reactor [15]. However, even with alloying additions to improve corrosion resistance, oxidation and hydrogen pickup of Zr is still the life-limiting condition of nuclear fuel elements used today and under accident conditions, runaway oxidation of zirconium and the associated hydrogen evolution can produce catastrophic consequences (e.g., the 2011 Fukushima Daiichi incident [16]). Moreover, the design criteria for advanced reactor technologies can differ substantially from that of traditional light-water reactors. For example, since LWRs rely on water to moderate the neutrons, any power transient that raises the water temperature will have the effect of reducing the density of the water (thermal expansion for small transients and potentially steam bubbles for large transients) which in effect reduces the moderating capability of the

reactor and reduces the fission rate, thus serving as a negative feedback mechanism to prevent the power transient from growing exponentially. By contrast, many advanced reactors operate using unmoderated fast neutrons, meaning the primary effect of the coolant (e.g., molten sodium) on the neutron population is to absorb neutrons; this means that during a power transient which raises the coolant temperature, the coolant becomes less dense and absorbs neutrons less efficiently which can serve to *increase* the reactivity of the system instead [17]. To counteract this positive coolant-temperature feedback mechanism, many advanced reactor designs rely on other feedback mechanisms including (among others) the thermal expansion of reactor vessel and internals, which can increase neutron leakage out of the system, to provide a net negative temperature feedback mechanism. For such reactors, greater emphasis is placed on maintaining core geometry and less emphasis is placed on maximizing the neutron population (which is in abundance), which has led to zirconium falling out of favor for fast reactor designs given the poor creep resistance (both thermal and irradiation-enhanced) of zirconium and its alloys at high temperatures as compared to many stainless steels [18]. Added to this is rather unique phenomenon of irradiation growth which most Zr fuel claddings are susceptible to, whereby in the absence of applied stress a Zr tube will grow in length under neutron irradiation, due to both the anisotropic hexagonal close-packed (HCP) crystal structure of Zr combined with the textured microstructure from the fabrication process (pilgering); this phenomenon arises from the preferential habitation of interstitial defect loops on the prismatic lattice planes and vacancy defect loops on the basal lattice planes which can lead to growth normal to the prismatic planes and contraction normal to the basal planes [19]. Since stainless steels primarily consist of isotropic face-centered cubic (FCC) and body-centered cubic (BCC) phases, they are not prone to irradiation growth.

While Zr alloys may not be suitable for most advanced reactor applications, transitioning to fuel claddings which are less transparent to neutrons comes with tradeoffs as well. In addition to penalizing the neutron economy in the reactor core, materials which interact with neutrons more frequently will accumulate radiation damage faster, which can manifest itself in many different ways almost all of which are detrimental to the performance of the material. When a neutron passes into a material, it can either be

absorbed by a nucleus in the host material, scatter off a nucleus in the host material, or pass through completely unaffected. In the case of absorption or scattering, the neutron can impart a substantial amount of energy to the host lattice by producing a primary knock-on atom (PKA) which has more than enough energy to knock adjacent atoms off of their lattice sites which continues as part of a damage cascade. To illustrate this, Figure 4 shows the results from a Molecular Dynamics (MD) simulation where a damage cascade is produced in a Au crystal lattice using a 10-keV PKA [20]. Within one picosecond, hundreds of atoms are knocked from their lattice sites and the local temperature rises well above the melting point of the material – this stage is referred to as the "heat spike" or "thermal spike" within the damage cascade. Then, over tens of picoseconds, displaced atoms quickly settle into new lattice sites in a nanoscale game of musical chairs as the heat diffuses out to the surrounding material. Once the heat is dissipated, only a few vacancies and self-interstitial atoms (SIAs) remain. Since the average energy of a fission-born neutron is ~2 MeV and only a small fraction of the neutron energy is imparted to the lattice during a scattering event (due to satisfying conservation of momentum), a single neutron could plausibly produce hundreds of such damage cascades before slowing to thermal energies and being absorbed.

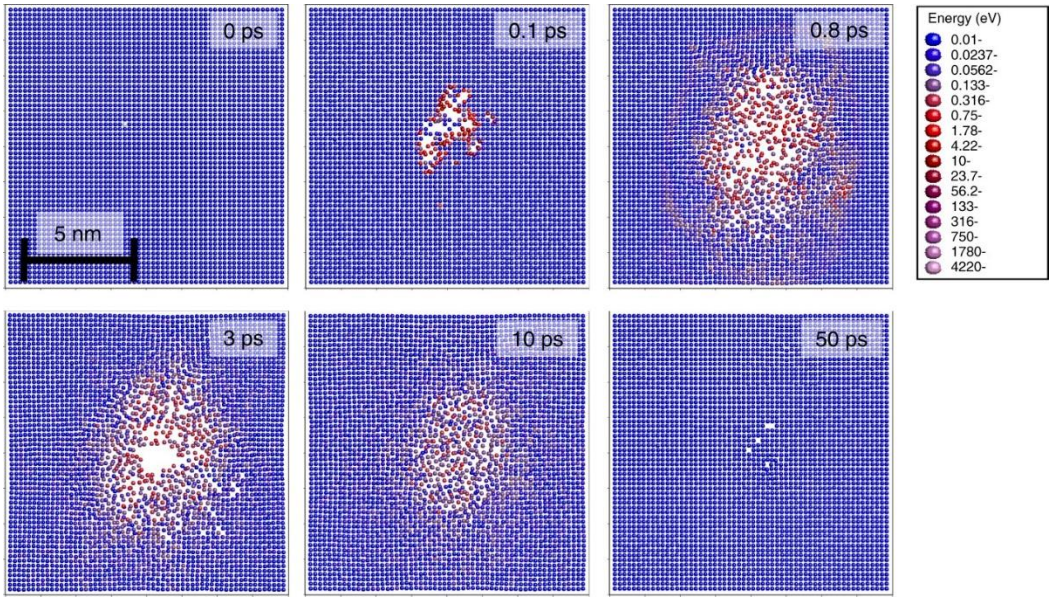

Figure 4*: Molecular Dynamics (MD) simulation of a damage cascade produced from a 10-keV primary knock-on atom (PKA) in an Au crystal lattice. Note the number of defects produced versus the surviving number of defects [20].*

Given the violent nature of the damage cascade, it is tempting to imagine that a material being bombarded by fast neutrons on the order of 10^{15} cm^2/s (as was the case for EBR-II [21]) would be quickly annihilated under such conditions. However, besides some potentially minor ballistic mixing which can contribute to the dissolution of precipitates [22, 23], the damage cascade itself does cause much harm to the host material since the vast majority of the created defects are quickly annealed away, rather, it is the few surviving point defects which cause the most harm and can lead to engineering challenges. As a material is irradiated surviving point defects from damage cascades begin to accumulate and the defect concentrations rise well above their equilibrium values. The surviving vacancies and SIAs have three possible means to reduce their energy within the crystal lattice: they can diffuse off to sinks such as grain boundaries and free surfaces, similar point defects can cluster together to form extended defects, or differing defects can recombine with each other and annihilate. The mechanism that is most active depends primarily on the homologous temperature of the material (i.e., the temperature of the material relative to its melting point). To illustrate this, Figure 5 shows examples of representative microstructures in irradiated materials as a function of irradiation temperature [24]. At extremely low temperatures ($<0.1T_m$) , both interstitial defects and vacancies remain nearly immobile, so as more and more irradiation damage is imparted to the material, ordered phases including ceramics and intermetallic compounds can be amorphized, while in metals small defect clusters known as “black-dot defects” may arise, so named after their appearance when view under a transmission electron microscope (TEM), in areas where damage cascades overlap. Irradiation damage can quickly saturate at these temperatures as the higher concentrations of both interstitial defects and vacancies throughout the material greatly improve the defect recombination rate such that subsequent damage cascades do not produce a net gain of defects. At slightly warmer irradiation temperatures (~0.1-$0.2T_m$), SIAs gain some mobility allowing them to form larger clusters which can collapse into interstitial dislocation loops (extra discs of atoms in between close-packed planes) which grow in both size and number as a function of irradiation dose and may slowly start to interact and agglomerate with each other forming networks of dislocations; vacancies are still largely immobile at these temperatures. Between ~0.2-$0.3T_m$, SIAs begin diffusing over longer ranges to grain boundaries while vacancies remain sluggish, but can begin

to form clusters which serve as nuclei for voids and bubbles (where fission gas and helium from α-decay can accumulate). From ~0.3-0.6T_m, both SIAs and vacancies can diffuse, however there is still a substantial difference in diffusion rate and behavior of the defects in the material. SIAs quickly diffuse to sinks which causes the concentration of SIAs in the bulk to quickly level off while vacancy concentration continues to grow for substantially longer until vacancy production is balanced by annihilation at sinks. Due to the differences in diffusion rates and the different biases of sinks (namely the preference for SIAs to diffuse to dislocations over vacancies tendency to do), and as the concentration of vacancies rises more voids and gas bubble begin to nucleate and grow inside the material, which serve as sinks for new vacancies. The formation of and growth of these voids leads to "void swelling" of the material which can lead to macroscopic changes volume of reactor components. Additionally, the diffusion of both interstitial defects and vacancies to the grain boundaries can lead to preferential enrichment or depletion of elements around the grain boundary (depending on whether the diffusion of a given element is dominated by an interstitial or vacancy hopping mechanism, and the relative sizes of each atom in the system). This radiation-induced segregation (RIS) can lead to changes in the oxidation and corrosion properties of a material, by redistributing chromium for example, which can give rise to phenomena such as irradiation-assisted stress corrosion cracking (IASCC) as well as radiation-induced precipitation at the grain boundaries, promoted by changes in local chemistry as well as irradiation-enhanced diffusion [25]. At temperatures much above ~0.6T_m, both SIAs and vacancies are highly mobile which combined with a higher thermal equilibrium concentration of vacancies decreases the supersaturation of vacancies in the bulk leads inhibits void formation and can promote thermal emission of vacancies from clusters. Additionally, thermal diffusion is able to smooth out concentration gradients that would be produces from RIS. However, enhanced thermal diffusion also acts to accelerate creep at these temperatures and the added mobility of helium-vacancy complexes can lead to the formation of He bubbles along grain boundaries which greatly reduce the strength of the affected grain boundaries [26].

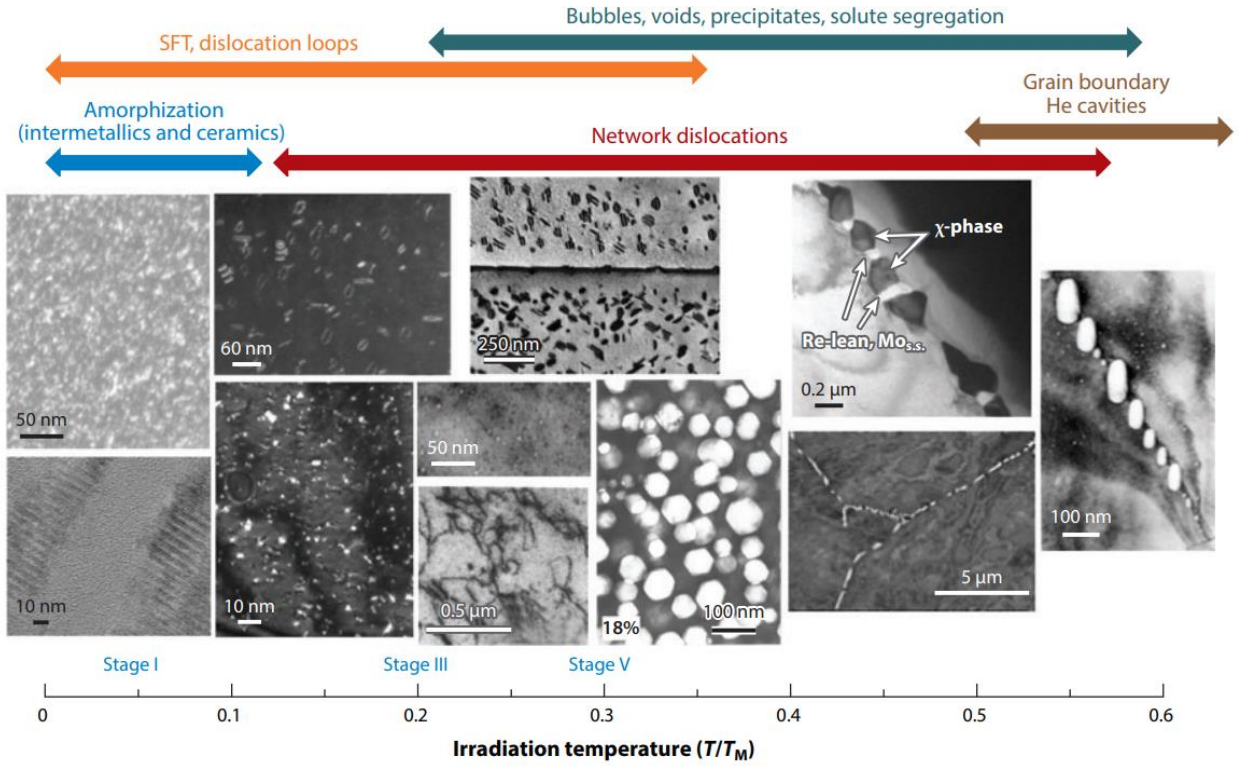

Figure 5*: Examples of representative microstructures in irradiated materials as a function of irradiation temperature [24].*

Changes in microstructure at the nanoscale and mesoscale, including void swelling, dislocation loop formation, and RIS, can lead to changes in dimensions and mechanical properties at the engineering scale. To illustrate this, Figure 6a shows the increase in size of a section of 20% cold-worked 316 stainless steel cladding after being exposed to a fast fluence of $1.5*10^{23}$ n/cm^2 at 533 °C in EBR-II [27] while Figure 6b shows an example of severe embrittlement the same steel subjected to a thermal aging treatment to promote carbide precipitation prior to irradiation to the same fast fluence at 400 °C. Here the effects of both void swelling and irradiation embrittlement are apparent, as both tubes have swelled isotropically more than 10% while the steel tube irradiated at 400 °C shattered while being held in a vise during sample preparation as part of the post irradiation examination. Indeed, these are not the dimensions nor mechanical properties the materials had prior to entering the reactor, and evolution of material properties and component dimensions can jeopardize the maintenance of coolable reactor geometries and thus the safe and predictable operation of nuclear reactors.

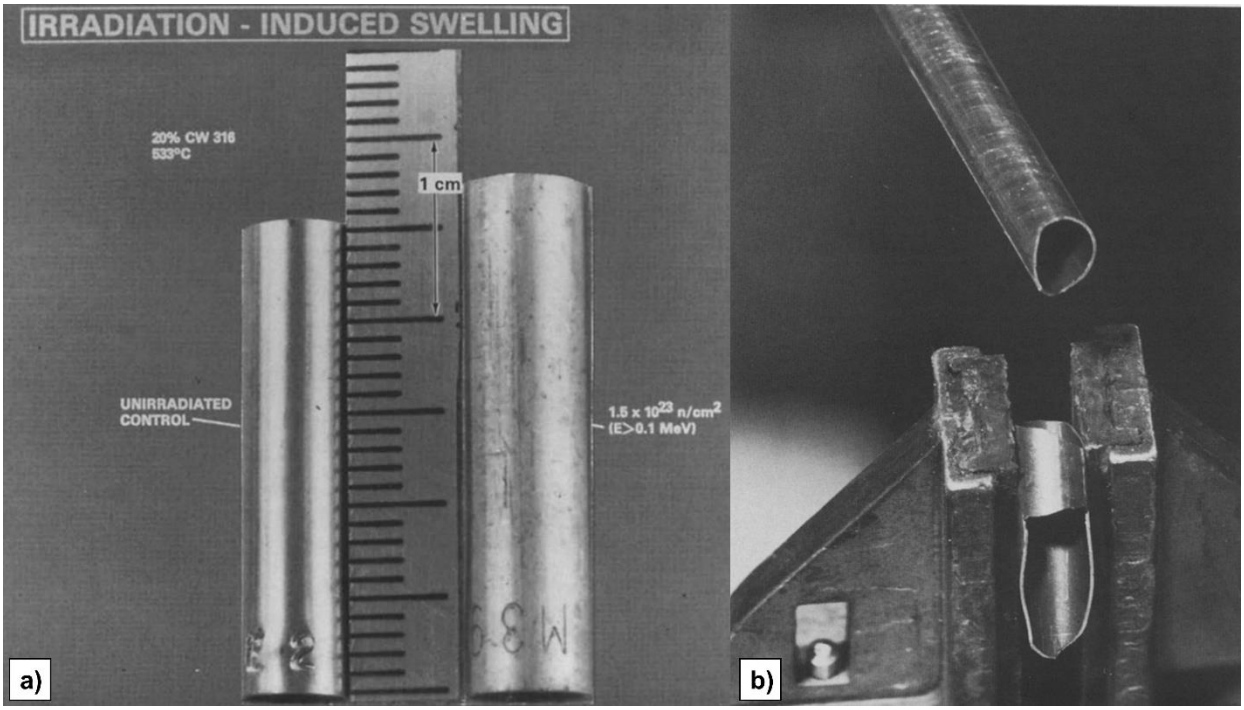

Figure 6*: a) Dimensional changes resulting from void swelling in 20% cold-worked 316 stainless steel, irradiated to a fast fluence of 1.5*10^{23} n/cm^2 at 533 °C in EBR-II [27]. b) Example of severe embrittlement in 20% cold-worked 316 stainless steel subjected to an aging treatment before irradiation the same fast fluence at 400 °C in EBR-II [28]; the tube in this case shattered when mounted in a vise during sample preparation.*

Besides increasing dimensional allowances and adding large plenums to fuel rods to accommodate the production of fission gas without being excessively pressurized, there are few engineering solutions available to accommodate the changing dimensions and properties of materials within a nuclear reactor. Instead of addressing the effects after the fact, preventing excessive void swelling and irradiation embrittlement requires targeting the root cause of these phenomena, which is the generation and agglomeration of point defects into extended defect structures such as voids and dislocations loops under irradiation. Typically, since parameters such as dose, dose rate, and temperature are set by the design of the reactor, the most straightforward way to improve the irradiation tolerance of a material is by increasing its density of defect sinks. The primary defect sinks in bulk materials (i.e., ignoring surface effects) are dislocations, precipitate interfaces, and grain boundaries – each of which can be controlled through alloy selection and metallurgical processing. Increasing the density of defect sinks works to mitigate effects of

irradiation damage by decreasing the distance a defect is required to diffuse before it is annihilated. By decreasing this distance, the steady-state concentrations of SIA defects and vacancies within a material under irradiation can be decreased, ideally such that defect fluxes to extended defects, such as voids, are small enough to prevent them from nucleating and growing. To increase the density of dislocations within material, cold working can be applied, wherein a material is plastically deformed without being heated to temperatures sufficiently high enough induce recrystallization. Indeed, cold working amounts up to 30% thickness reduction have been shown to improve the void swelling behavior of 316 stainless steel in fast-neutron environments by prolonging the incubation before void swelling accelerates to steady state linear rate versus the dose [29]. Extensive coldworking can also be used as a means of producing nano-grained materials, for instance in austenitic stainless steels [30], in lieu of more exotic processing techniques [31, 32]. To increase the total interfacial area between the matrix and precipitates without substantially altering the composition of the alloy, insoluble nanoscale particles can be added to the materials to make a fine dispersion of defect sinks throughout the material. Being that oxides are the most common insoluble particle added to such materials, and oxygen is often already present as an impurity in most metals, these alloys are referred to as oxide-dispersion strengthened (ODS) alloys, and such alloys have been shown to have improved resistance to void swelling [33]. Moreover, these engineered microstructural features can be combined with one another and act synergistically with one another, as is the case with ODS alloys where the oxide precipitates can help pin grain boundaries and preserve nano-grained structures.

The primary challenge with relying on such heavily engineered microstructures to provide irradiation tolerance is that many of these features are not thermally stable at high temperatures, let alone under conditions with irradiation-enhanced diffusion. By increasing the interfacial area within a material through additions of dislocations, oxide dispersions, and nano-grain refinement, the increase in surface energy caused by the presence of these features can produce a large driving force favoring their annihilation. Dislocations can be annealed out and both the grains in nanocrystalline materials and the particles in ODS alloys may coarsen over time via Ostwald ripening [34] or be dissolved by ballistic mixing. Material

selection is also intrinsically dependent on the application environments which can vary substantially across different reactor designs. To demonstrate the demanding environmental conditions materials in advanced reactors can be subjected to, Figure 7 illustrates the ranges of operating temperatures, corrosive environments, and lifetime irradiation damages of several advanced reactor concepts [35]. Here, the unit displacement(s) per atom (dpa) is used – a unit intended to standardize the description of the irradiation damage in parted to materials regardless of dose rate, particle energy, or particle species (e.g., proton, neutron, heavy ion, electron) – where after 1 dpa of irradiation damage, every atom in a given volume of material has been displaced on average once. In LWRs in the current reactor fleet, fuel cladding materials can reach tens of dpa by their end-of-life within the reactor, while in comparison many advanced reactors are anticipated to subject materials to between 100 and 200 dpa. One particularly ambitious reactor design, the traveling wave reactor (TWR) proposed by Terrapower, intends on subjecting fuel cladding materials to approximately 600 dpa of irradiation damage over the lifetime of the core [36].

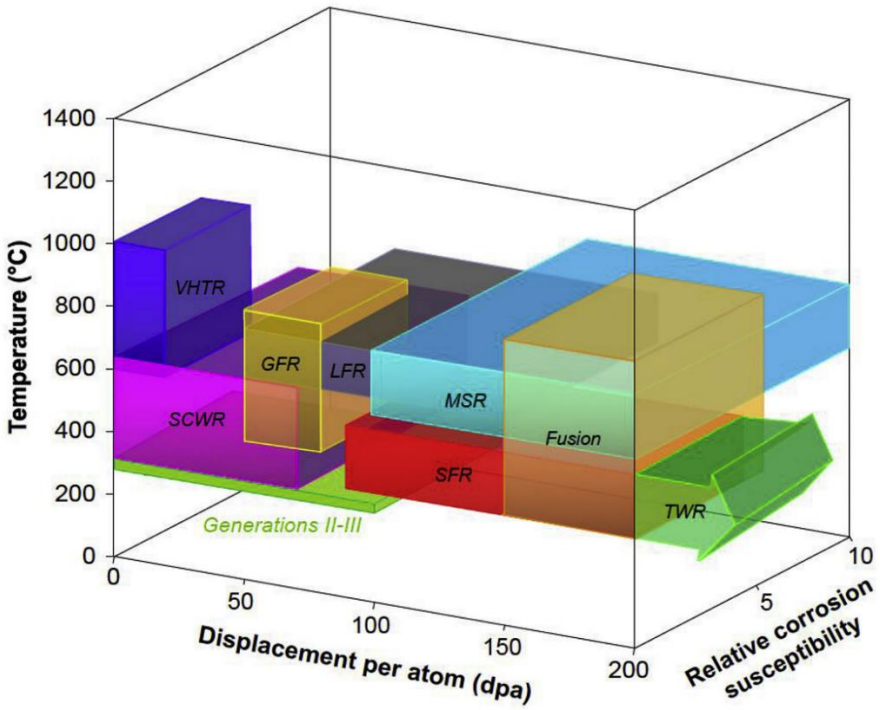

***Figure 7**: Temperature, irradiation damage, and corrosive conditions for various reactor designs, including supercritical-water reactors (SCWRs), very-high-temperature reactors (VHTRs), gas-cooled fast reactors (GFRs), lead-cooled fast reactors (LFRs), sodium-cooled fast reactors (SFRs), molten-salt reactors (MSRs), fusion reactors, and the traveling wave reactor (TWR) – an SFR variant [35].*

Since many advanced reactor designs push and often exceed the limits of materials historically used to construct nuclear reactors, commercial realization of such reactors will require the use of materials beyond that which has been currently ASME code-qualified for high-temperature nuclear reactors – a list which currently includes a grand total of six alloys following the new addition of Alloy 617 [37]. Additionally, of the alloys that are ASME code-qualified for high-temperature nuclear reactors, none were designed specifically for nuclear applications and have instead been borrowed from use in other industries. As a result, reactor designers and researchers have been prompted to consider more out-of-the-box choices in materials for such reactors. Serendipitously, this search for new material candidates, accelerated by growing commercial interest in advanced reactor development, has coincided with the explosive growth in research interest in a novel class of materials which, among other properties, have been shown to exhibit enhanced irradiation tolerance. The subject of the next section will focus on investigations into the development and properties of this novel class of materials, known as high-entropy alloys.

1.3 Rise of High-Entropy Alloys

As opposed to the majority of industrially relevant alloys used today (steels, aluminum alloys, titanium alloys, etc.), high-entropy alloys (HEAs) represent a fundamental departure from conventional metallurgy methodologies. Whereas conventional alloys are typically comprised of one or two principal elements with their properties tweaked by adding small alloying additions, HEAs consist of several principal elements often present in near equimolar quantities. The result is a material with a structure and properties that are not dictated primarily by a single element, but rather behave as an average of each primary constituent element. Beginning with two seminal papers in 2004, researchers Brian Cantor and Jien-Wei Yeh independently stumbled onto a trend in research which would grow exponentially over the next 15 years, as shown in Figure 8 by the growth in the number of articles featuring HEAs published each year. In his paper, Cantor arc melted several alloys containing many elements in equiatomic ratios, including one 20-component ingot, with 5 at% each of Mn, Cr, Fe, Co, Ni, Cu, Ag, W, Mo, Nb, Al, Cd, Sn, Pb, Bi, Zn, Ge, Si, Sb, and Mg [38]. It was discovered that in the case of the equimolar 20-component alloy,

far fewer phases formed than what was thermodynamically possible, per the Gibbs phase rule, and that within the ingot, a solid-solution phase of nearly equimolar Co-Cr-Fe-Mn-Ni had formed. Cantor then arc melted down a separate ingot of equimolar Co-Cr-Fe-Mn-Ni and found using X-ray diffraction (XRD) that the alloy exhibited a single, disordered FCC crystal structure – this alloy would go on to be referred to as the Cantor alloy or Cantor's alloy in literature [39, 40]. At the same time, Yeh et al. were examining CoCrCuFeNi, also found to be single-phase FCC, and the effects of Al additions on the transformation from FCC to BCC [41]. Motivating their alloy design was a pursuit of maximizing the configurational entropy in expanded alloy systems in the hope that this increase in entropy would be sufficient to suppress the formation of intermetallic compounds, which are often deleterious to the mechanical properties of materials. Yeh is credited with coining the term "high-entropy alloy", which he originally defined as equimolar alloys of five or more principal elements.

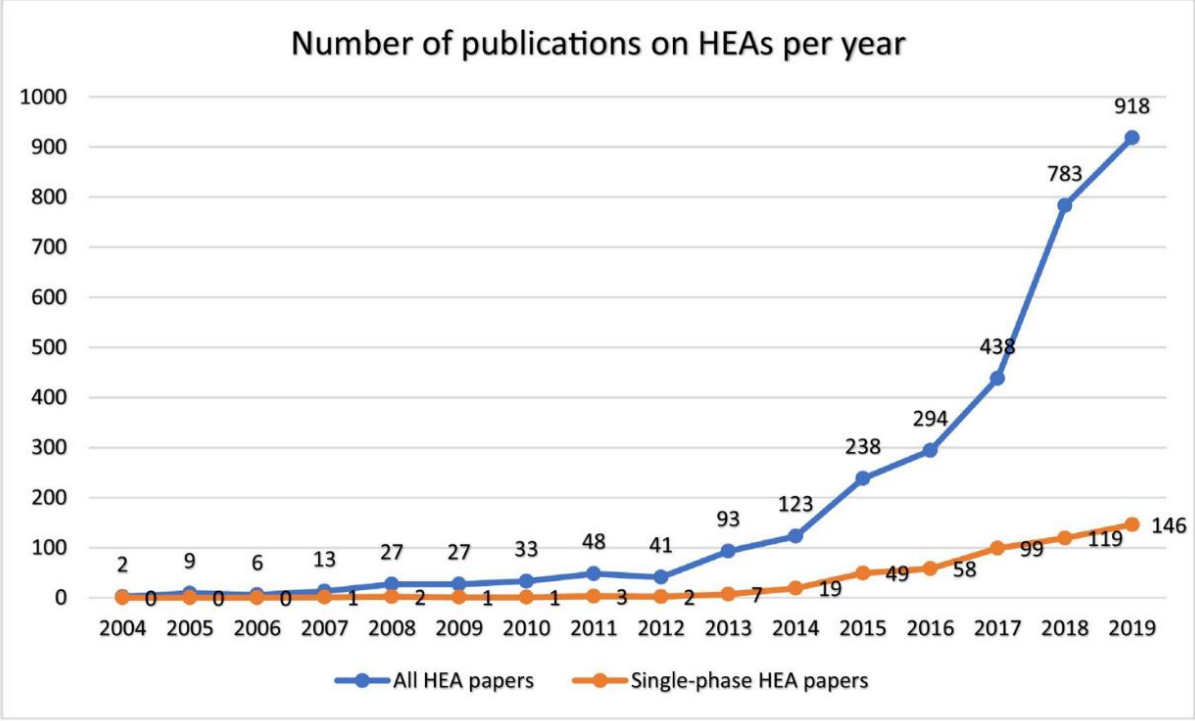

***Figure 8**: Number of articles featuring HEAs published each year since 2004. Note that this article was submitted for publication before the end of 2019 [42].*

Note: Regarding nomenclature, as there appears to be no universally agreed upon standard, alloy compositions will hereinafter be written as their constituent elements in alphabetical order. For equimolar compositions, the alloys will simply be referred to as a string of their constituent elements symbols (e.g., CoCrFeMnNi), for non-equimolar compositions, subscripts will be added to denote the atomic percent of each constituent element (e.g., $Co_{10}Cr_{15}Fe_{35}Mn_{20}Ni_{20}$). Additionally, for the sake of completeness, Table 1.1 lists several terms that have been used to categorize the alloys compositionally in and around the realm of HEAs. Each of these terms uses different criteria to categorize alloys which can be more or less restrictive depending on which source is defining it. Typically, the definitions use number of elements, ratio of elements, configurational entropy, total entropy, enthalpy of mixing, atomic radius mismatch, etc. to refer to a set of alloy systems, however as a result, many of the definitions overlap and some definitions are more exclusive than others. At their core, each definition seeks to envelope the region of composition space in the center of a phase diagram while eliminating the dilute solutions at the edges. Additionally, these definitions have evolved and, in some cases, relaxed over time. For example, while HEAs were initially defined as equiatomic alloys with five or more components, this was quickly broadened to five or more components ranging it concentration between 5-35 at% [41], which has since been expanded to include four elements and even some three element systems [43]. In some cases, it has been suggested that to be an HEA, the system must be a single-phase solid solution, however, since the entropy term in the Gibbs free energy is temperature dependent, this criteria is also arbitrarily temperature dependent since as temperatures approach absolute zero, the entropy contribution to the Gibbs free energy vanishes [44].

Table 1.1: *Alloy nomenclature from literature.*

Name	Reference
Baseless Alloys	[44]
Complex Concentrated Alloys (CCAs)	[45]
Compositionally Complex Alloys (CCAs)	[46]
Entropic Alloys	[47]
Equiatomic Multicomponent Alloys	[38]
High-Entropy Alloys (HEAs)	[41]
Medium-Entropy Alloys (MEAs)	[48]
Multicomponent Alloys	[38]
Multi-Principal Element Alloys (MPEAs)	[49]
Multinary Alloys	[50]
Single-Phase Concentrated Solid-Solution Alloys (SP-CSAs)	[51]

To avoid becoming entangled in the ever-evolving nomenclature, an approach similar to that of Miracle and Senkov [52] has been taken within this text to include the greatest number of alloys that still capture the *spirit* of what it is to have a multi-principal component system whose properties are not dictated by any one primary element. Thus, as "high-entropy alloy" (HEA) is the term most often used to describe such systems, *any alloy with no element present in greater concentration than 35 at% will be referred to hereinafter as an HEA*. This should simplify the naming and still include concentrated ternary systems and systems that have elements present less than 5 at%, while still excluding binaries and many industrial alloys today that can be compositionally complex such as stainless steels and nickel-based super alloys. To describe alloys which have more than 35 at% of one element but still less than 50% of said element, the broader term "complex concentrated alloys" (CCAs) will be employed. While this unfortunately shares its acronym with compositionally complex alloys, there is no formal distinction between the two and thus they could be used interchangeably anyway.

Though an alloy need not be a single-phase solid solution to be considered an HEA, much of the research in the area is focused on finding such alloys. There are reasons for this both from a standpoint of scientific understanding and of practicality. Thermodynamically speaking, under ambient conditions the most stable phase (or phases) of a system are dictated by the Gibbs free energy of mixing, given below, where ΔH_{mix} is the enthalpy of mixing, T is temperature, and ΔS_{mix} is the entropy of mixing:

$$\Delta G_{mix} = \Delta H_{mix} - T\Delta S_{mix}$$

The most stable configuration is achieved when the Gibbs free energy is minimized. In most conventional alloys, the phases present are often dictated by heat of mixing, ΔH_{mix}. If ΔH_{mix} for the solid-solution phase is largely positive, the system will tend to phase separate as it not energetically favorable for atoms of different species to mix with one another. If ΔH_{mix} for any of the ordered phases is largely negative, the system will often form ordered compounds, such as intermetallic phases, so as to ensure atoms of different species are located next to one another. It is also possible that one phase is more energetically favorable than all others, but due to a non-negligible and positive ΔH_{mix} the system can lower its energy by separating continuously into two regions sharing the same crystal structure but with disparate compositions, as is the case in a spinodal decomposition. These different microstructural outcomes are summarized in Figure 9, which schematically shows how different shapes and sizes of the Gibbs free energy curves can produce different combinations of thermodynamically stable phases. The allure of HEAs, however, is that due to the compositional complexity arising from having several principal components, the system will typically have a very large ΔS_{mix} term which can dominate over the ΔH_{mix} term any ordered phases over relevant temperature ranges leading to a single disordered solid-solution phase being the most thermodynamically stable.

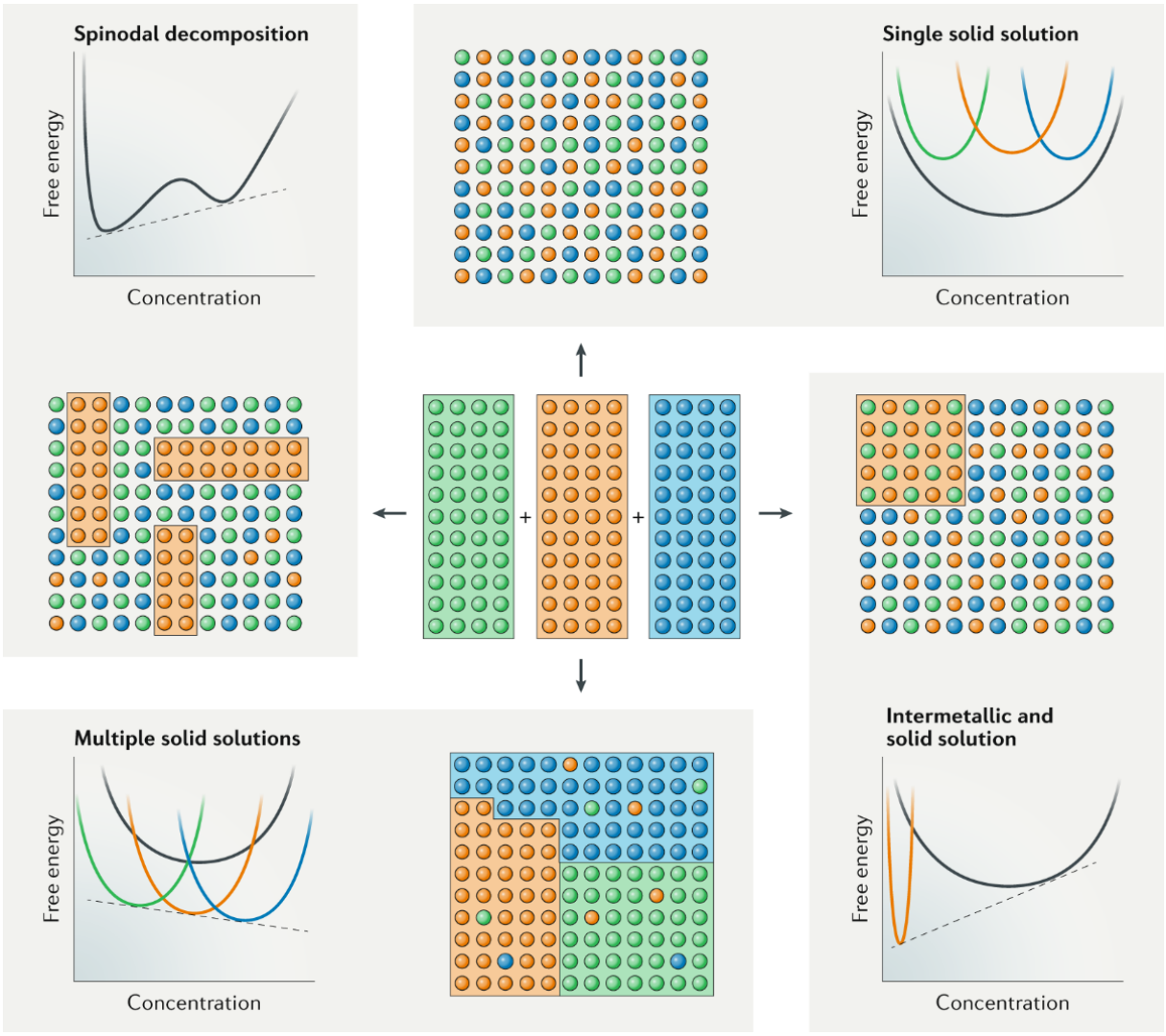

Figure 9*: Some of the possible reactions that can occur when three different elements, represented by the red, blue and green spheres, are mixed in equal proportions, including spinodal decomposition, formation of single or multiple solid solutions or precipitation of an intermetallic compound in a solid solution [53].*

Due to the compositional complexity of HEAs which exist in a phase space distant from our dilute-solution approximations, their properties can be difficult to predict. This makes studying single-phase HEAs, to isolate the mechanisms that give rise to their properties, more tractable, and perhaps insightful, than beginning with a multiphase HEA that will add additional layers of complexity. Consequently, several criteria have been used to predict single-phase solid-solution HEAs and often incorporate the relative magnitude of ΔS_{mix} and ΔH_{mix}, as well as other more traditional means of predicting solid solubility such

as the Hume-Rothery rules. Table 1.2 summarizes some of the criteria commonly found in literature, in no particular order.

Table 1.2: *List of criteria commonly used to predict single-phase HEAs.*

Criteria	Definition	Value Range Suggesting Solid Solution HEA	Reference
ΔS_{mix}	$-R\sum_{i=1}^{n} x_i \ln(x_i)$	$11 \leq \Delta S_{mix} \leq 19.5$ J/(K·mol)	[54]
ΔH_{mix}	$\sum_{i=1,j>i}^{n} 4\Delta H_{ij} c_i c_j$	$-22 \leq \Delta H_{mix} \leq 7$ kJ/mol	[54]
Ω	$\frac{T_{melt}\Delta S_{mix}}{\lvert\Delta H_{mix}\rvert}$	Ω >1.1	[55]
δ	$\sqrt{\sum_{i=1}^{n} x_i\left(1-\frac{r_i}{\sum_{j=1}^{n} x_j r_j}\right)^2}$	δ <6.6%	[56]
Δχ	$\sqrt{\sum_{i=1}^{n} x_i\left(\chi_i-\sum_{j=1}^{n} x_j\chi_j\right)^2}$	Δχ <0.133	[57]
Φ	$\frac{\Delta G_{mix}^{SS}}{-\lvert\Delta G_{mix}^{max}\rvert}$	Φ >1	[58]
γ	$\frac{1-\sqrt{\frac{(r_{smallest}-\bar{r})^2-\bar{r}^2}{(r_{smallest}-\bar{r})^2}}}{1-\sqrt{\frac{(r_{largest}-\bar{r})^2-\bar{r}^2}{(r_{largest}-\bar{r})^2}}}$	γ <1.175	[59]
α_2	$\sum_{i=1}^{n}\sum_{j\geq 1}^{n} \frac{x_i x_j (r_i + r_j + 2\bar{r})}{2\bar{r}}$	α_2 <0.06	[60]
VEC	$\sum_{i=1}^{n} x_i VEC_i$	BCC: VEC <6.87 BCC+FCC: 6.87< VEC <8.0 FCC: VEC >8.0	[61]

R – ideal-gas constant

r_i – atomic (metallic) radius

T_{melt} – melting temperature

VEC – valence electron concentration

x_i – mole fraction

χ_i – Pauling electronegativity

To summarize, ΔS_{mix}, ΔH_{mix}, Ω, and Φ derive their predictive capabilities from thermodynamics whereas δ, $\Delta\chi$, γ, α_2, and VEC to use the Hume-Rothery rules as the basis for their justification. From the arguments previously made, one would expect there to be no lower bound for ΔH_{mix} and no upper bound for ΔS_{mix} in the range of acceptable values for the solid solution phase, since ideally minimizing ΔH_{mix} and maximizing ΔS_{mix} would yield the most negative Gibbs free energy making the solid solution the most stable phase. However, these ranges are based on empirical observations as simply having a large entropy term or low enthalpy term does not preclude the formation of other phases – though having values that satisfy both terms will generally increase the likelihood of forming a solid solution. In contrast to empirical observations, Ω and Φ form predictions based on the relative ratios of ΔS_{mix}, ΔH_{mix}, and T_{melt}. Ω is one of the most common parameters used to predict solid solutions in HEAs in part because of its ease of calculation as well as its straightforward interpretation: if ΔH_{mix} is larger in magnitude than $T_{melt}\Delta S_{mix}$ and positive, the system will phase separate; if ΔH_{mix} is larger in magnitude than $T_{melt}\Delta S_{mix}$ and negative, the system would likely be more susceptible to forming a single ordered phase. This approach may be a useful back-of-the-envelope calculation; however, it does have some shortcomings. For example, it does not include the possible formation of any intermetallic phases.

Though Ω is able elucidate whether the disordered solid-solution phase is more stable than two disordered solid-solution phases or one entirely ordered phase, there are a variety of different two- and three-component intermetallics that may reduce the overall Gibbs free energy of the system by forming. To include this, King devised the Φ criteria which takes into account the ratio between the free energy of the solid-solution phase (ΔG_{mix}^{SS}) and the largest free-energy magnitude of any other phase that could form including intermetallics ($|\Delta G_{mix}^{max}|$). As such, a system with Φ greater than one indicates that the disordered solid solution is the *single*-most stable phase. However, while the disordered solid solution may be the single-most stable phase, this still leaves the possibility for secondary phases to form alongside the primary solid-solution phase which may reduce the overall energy of the system, as illustrated previously in Figure 9. Merely the presence of an additional phase that is more stable than the disordered solid solution at any composition runs the risk of precipitating out in some fraction depending on the composition of the overall system. Unfortunately, the Φ criteria only takes into account ΔG_{mix} of phases at the composition of the overall system and thus does not capture the possibility of second phases precipitating out in smaller fractions.

Indeed, there are many thermodynamic and chemical considerations that need to be taken into account to successfully predict single-phase HEA compositions, thus no one of the aforementioned criteria is a failsafe predictor. That is, however, not to detract from their value, as many of the single-phase compositions discovered (e.g. CoCrFeMnNi, MoNbTaW, etc.) satisfy most if not all of these criteria. Additionally, compositions that fall outside of the parameter space defined by these criteria have been shown by and large to phase separate, as shown in Figure 10, meaning that these criteria are effective at narrowing the search for single-phase compositions. In summary, the empirical criteria for determining single-phase HEA compositions are useful for eliminating compositions that will likely phase separate but are still prone to generating false positives; generally, these criteria are more guidelines than actual rules.

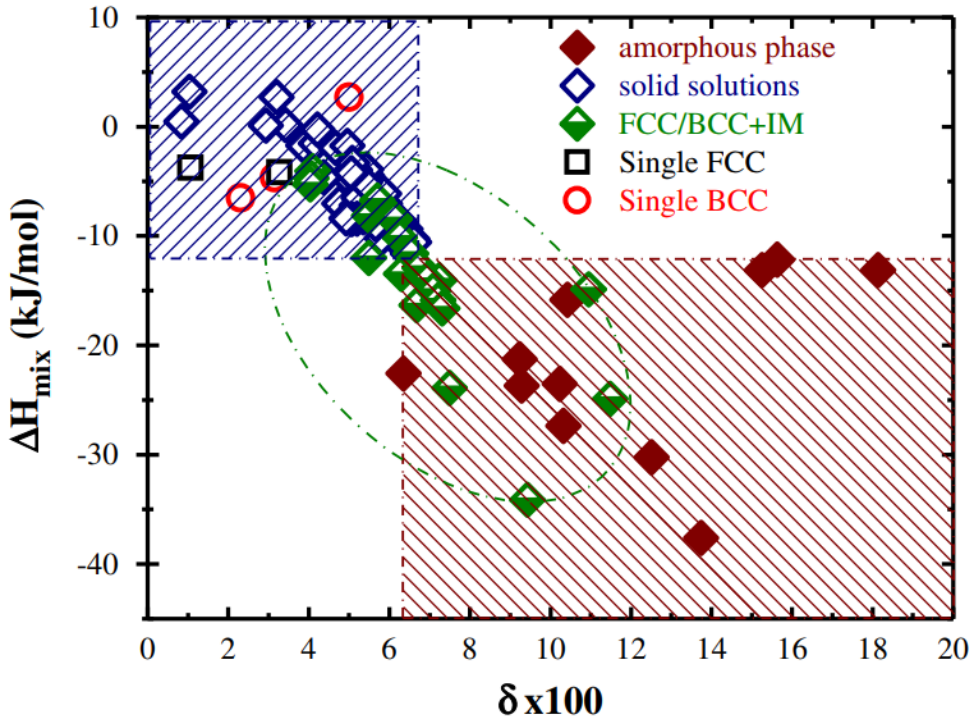

***Figure 10**: Phase content of several as-cast HEA compositions plotted with respect to single-phase prediction criteria [62].*

1.4 High-Entropy Alloys for Advanced Nuclear Applications

High-entropy alloys have been demonstrated to exhibit a broad range of promising properties for both structural materials and functional materials including markedly higher yield strengths than Ni-based superalloys at high temperatures [63], fracture toughness comparable to the best cryogenic steels at low temperatures [64], high-temperature oxidation resistance [65], and superplastic behavior [66], as well as efficient catalysis of H_2 and CO_2 [67] and the largest magnetocaloric effect experimentally observed in a material [68]. But by far, the most relevant and intriguing property of HEAs for nuclear application is their microstructural response to irradiation damage. Many experimental studies have shown that certain HEA compositions outperform their less compositionally complex counterparts under irradiation [51, 69-75], especially when comparing void swelling behavior. To illustrate this, Figure 11 shows the relative swelling amount of different equimolar HEAs and CCAs subjected to 3-MeV Ni ion irradiation to a fluence of 5E16 ions/cm^2, corresponding to a peak damage of 53 dpa, at an irradiation temperature of 500 °C. Here it can

be seen, for example in Figure 11a, that with increasing compositional complexity (Ni→NiCo→NiCoCr→NiCoFeCrMn) the amount of void swelling decreases from ~7% down to nearly immeasurable. While the differences in void swelling behavior are striking, the mechanistic reason for these differences in behavior remains unclear.

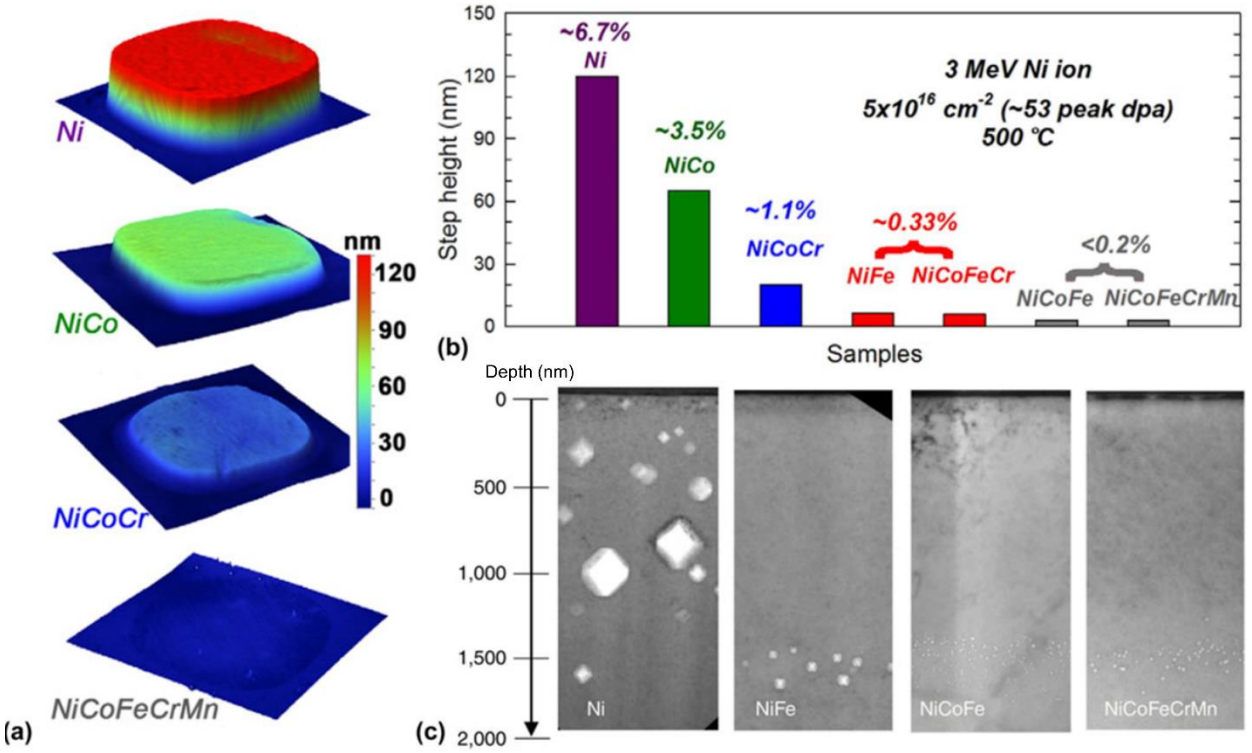

***Figure 11**: Void swelling in equimolar Co-Cr-Fe-Mn-Ni-based HEAs and CCAs following 3-MeV Ni ion irradiation at 500 °C to fluence of 5E16 ions/cm^2, with a peak damage level of 53 dpa, as measured by a-b) optical profilometry and c) transmission electron microscopy (TEM). Adapted from [76].*

To understand the origins of the apparent irradiation tolerance exhibited by HEAs, many mechanisms have been proposed in literature, which will be described in chronological order over the evolution of irradiation damage in a material as follows:

- **More recombination during damage cascade.** From the Kinchin-Pease (KP) model, the number of defects produced from a single PKA is only dependent on the ratio of the PKA energy to the displacement energy (the energy required to form a vacancy/SIA pair) [77, 78]. As such, it follows that the number of defects produced from a PKA of a given energy should be the same in an HEA as in a

pure metal if their displacement energies are comparable, which is already a charitable assumption since some simulations have shown HEAs have a *lower* displacement energy than pure metals [79]. If the number of defects initially created during the damage cascade in an HEA is equal to or greater than a pure metal, one possibility for the apparent irradiation tolerance of HEAs is that more recombination of these point defects occurs before the heat dissipates from the damage cascade and quenches in the surviving defects. Since the length scales and timescales of the damage cascade are prohibitively short for experimental observation, support for this proposed mechanism comes primarily from simulation. Specifically of interest is the increase in phonon scattering in HEAs and CCAs relative to pure or less compositionally complex metals. While electrons are the primary heat carriers in metals under most circumstances, during the damage cascade, energy is imparted directly to the ions and heat transport is dictated primarily by phonons rather than electrons, based on the difference between the lattice and electronic heat capacities [80, 81]. Since populating a lattice with different elements leads to greater phonon scattering, based on the difference in masses and interatomic forces between the different atom species, HEAs and CCAs would be expected to have lower lattice thermal conductivity [82]. During the damage cascade, a lower lattice thermal conductivity would imply that the heat deposited during the damage cascade remains localized longer before being dissipated in the surrounding material, which would allow more time for recombination of point defects to occur before the surviving defects are quenched in. Indeed, differences in lattice thermal conductivity have been used to explain the difference in void swelling behavior of Ni, NiCo, and NiFe [83, 84], visible in Figure 11b. However, simulations from other studies have shown similar and sometimes *more* surviving point defects following the damage cascade in HEAs compares to less complex alloys [79, 85], so it remains unclear if enhanced recombination exists in HEAs, and if so, to what extent it improves the overall irradiation resistance of the material.

- **Sluggish diffusion of point defects.** Since the coinage of the term “high-entropy alloy,” including the first paper to use the name, HEAs have been suspected to exhibit “sluggish diffusion” [41]. However,

the general assertion of the sluggish diffusion hypothesis in the literature without extensive experimental evidence has produced some contention within the HEA community on the topic [86]. Indeed, there are both experimental results and simulations that appear to demonstrate sluggish diffusion in the form of greater migration energies in HEAs versus pure metals (when normalizing to the homologous temperature) [87, 88], however these are outweighed by the number of studies which report a lack of evidence for universal sluggish diffusion in HEAs [89-93]. Nevertheless, sluggish diffusion of point defects has been suggested as a possible explanation for the enhanced irradiation resistance experimentally observed in several HEAs. The primary hypothesis supporting sluggish diffusion is that the potential energy landscape within an HEA lattice will exhibit more peaks and valleys due to the differences in mass, interatomic forces, and lattice strain caused by presence of different atomic species occupying the same crystal lattice. Such potential energy valleys, specifically, could serve as "trapping sites" for diffusing point defects which would retard the formation of extended defects (e.g., vacancy clusters and SIA clusters) and instead the concentration of both SIAs and vacancies within the material would be greater, thus producing more sites for recombination to occur and leading to a greater rate of recombination from subsequent damage cascades. In essence, the link between sluggish diffusion of point defects and enhanced irradiation tolerance draws parallels to the very-low-temperature regime of irradiation damage evolution (Figure 5) where in the absence of long-range diffusion, point-defect concentrations saturate and extended radiation-induced defects, such as voids, never form.

- **Broadening/overlapping defect migration energies.** Perhaps more nuanced than universal sluggish diffusion of point defects, another proposed mechanism posits that the chemical complexity of HEAs and CCAs leads to distributions of migration energies for SIAs and vacancies, which may overlap enabling enhanced defect recombination (or at least mitigate the clustering of like defects into extended structures like voids and dislocations). Since experimentally there is no clear way to measure the distribution of defect migration energies, only the effective migration energy, support for this mechanism comes almost exclusively from modeling and simulation. Indeed, many atomistic

simulations have shown, primarily using binary systems, that increasing chemical complexity and solute concentration leads to a broadening distribution of defect migration energies due to the variety of different local atomic configurations in disordered solid solutions [94-97]. Specifically, these distributions of migration energies tend to be skewed towards slowing down the diffusion of SIAs and speeding of the diffusion of vacancies [95, 97]. By reducing the discrepancy between the diffusion rates of interstitials and vacancies, the difference in concentration between these defects is also reduced which should increase recombination rates, since the probability of recombination is maximized when the concentrations of SIAs and vacancies are equal. However, it is unclear whether such enhanced recombination is attributable to the presence of a distribution of migration energies, or merely a reduction in the average and minimum vacancy migration energies, since migration pathways with higher energy barriers are less likely to be accessed, for example by SIAs.

- **Sluggish diffusion of interstitial loops/clusters.** By far the easiest mechanism to observed experimentally, is the possible sluggish diffusion of interstitial dislocation loops and clusters. Rather than attempting to observe the diffusion of individual point defects or capture phenomena which occur on the order of picoseconds, as is the case with damage cascades, dislocation loops and clusters are large enough and move slow enough to be readily resolved through transmission electron microscopy (TEM). Since the rapid fleeing of interstitial atoms from the site of the damage cascade off to sinks such as grain boundaries contributes to the buildup of a vacancy supersaturation in a material, if interstitial atoms instead clustered together into relatively immobile dislocation loops or clusters near the damage cascade, the probability of recombination would be improved. Indeed, in several of the ion irradiation studies where reduced void swelling was observed in HEAs and CCAs, such as those highlighted in Figure 11, interstitial dislocation loops are observed throughout the irradiated region with small voids occurring deep in the material near the peak irradiation damage, as compared to less complex metals such as pure Ni where voids are found throughout the irradiated region and dislocations are only found deep inside the material in the form of dislocation networks [98, 99]. These experimental results are also in good agreement with Molecular Dynamics simulations, which predict interstitial

clusters and dislocation loops diffusing easily in 1D in pure metals (e.g., Ni) as compared to more compositionally complex alloys (e.g., NiFe, NiCo) in which interstitials clusters and dislocation loops diffuse more slowly and meander in 3D space [98]. While promising, this phenomenon has only been observed in equimolar FCC solid solutions from the Co-Cr-Fe-Mn-Ni system, thus more experimental and modeling work is necessary to determine whether such processes also play a significant role in different crystal structures and chemical systems.

While each of the above proposed mechanisms has been supported by some form of modeling and simulation, it still remains unclear which mechanism plays a dominant role in determining the performance of HEAs under irradiation. Moreover, each mechanism faces similar shortcomings and limitations, namely, the lack of experimental data. From the limited number of experimental studies that have explored the irradiation response of HEAs and CCAs, the vast majority focus on equimolar CoCrFeMnNi, or its equimolar derivatives (e.g., NiFe, NiCo). Such an approach makes isolating the effects of a single element on the irradiation response of HEAs and CCAs even more challenging, let alone the effects of multiple elements interacting, and leaves the near infinite number of non-equimolar HEA and CCA composition combinations unexplored. However, exploring a broad range of compositions quickly becomes a practical challenge given the amount of time required to synthesis, prepare, irradiate, and characterize even one new alloy using traditional metallurgical techniques, thus beginning with equimolar alloy compositions is often seen as a logical first step, but still remains a major compromise.

Even in the absence of daunting numbers of possible alloy compositions, certifying new materials for high-temperature nuclear applications remains an inordinately time-consuming process, as evidenced by only one new material becoming code-certified in the last 30 years [37]. Typically, modeling and simulation can be employed to provide insight and narrow the work scope in such situations, however HEAs and CCAs pose additional challenges for many of the techniques. In the case of atomistic, first-principles modeling, disordered solid solutions can be particularly computationally expensive to model in order to accurately produce the physics of a randomized assortment of atoms. Typically, in order to achieve adequate

statistical certainty, larger groups of atoms and/or many configurations of atoms must be simulated as compared to pure metals or ordered structures (e.g., oxides, intermetallics) which can result in substantially more computation time/power requirements. An alternative to atomistic modeling in many cases is to use continuum-level modeling informed by empirical databases, such as CALculation of PHAse Diagrams (CALPHAD), which can offer immense time savings. However, HEAs and CCAs occupy the center of the alloy composition space while most historical alloy data exists on the periphery, requiring large extrapolations to make predictions about the properties of these alloys. Such models will often also rely on regular- and dilute-solution approximations when calculating properties, which can lead to greater uncertainties in the results since HEAs and CCAs by definition occupy the region of the composition space where these assumptions are the least accurate. Thus, even modeling and simulation suffers from the lack of experimental data on HEAs and CCAs and the speed at which it can be generated. To efficiently explore the HEA composition space and eventually develop optimized alloys for advanced nuclear applications, new high-throughput experimental techniques must be developed.

1.5 High-Throughput Methodology

The term, "high-throughput," is inherently a relative and contemporary term much like "high-speed" or "advanced" in that it compares the throughput of a proposed process to that of what is most commonly used currently. What is considered *high-throughput* today may not be tomorrow. However, in addition to the comparative function, the term also connotes parallelization, automation, and often major gains in speed and efficiency, potentially at the cost of fidelity or completeness. High-throughput methodologies also tend to embody the Pareto principle, whereby 80% of the problem can be solved with 20% of the total required effort while the remaining 20% of the problem will consume 80% of the total required effort. As such, high-throughput methodologies are best suited for screening applications where a large array of samples can be quickly examined to determine macroscopic trends and be able to make informed down-selections before more labor-intensive techniques are applied. The prototypical example of the high-throughput methodology in action is the high-throughput screening (HTS) technique developed by the pharmaceutical industry to

search for potentially effective drug candidates. Beginning in the 1980s, automated screening techniques were developed using 96-well plates, each containing a mixture of human cells and unique chemical compound to test for interactions with [100]. While initial HTS techniques were limited to <10,000 test a day, prone to robotics/automation reliability issues, and output datasets which required substantial human involvement to process, shortly after the turn of the century the HTS process had become fully automated, screening millions of compound with little to no human oversight, producing dozens of leads, and bringing multiple drugs to market [101]. While high-throughput, automated research will always remain imperfect, the many orders of magnitude increase in speed and efficiency is generally seen to outweigh the marginal gains in accuracy or reductions in false positives/negatives afforded by more meticulous testing performed by humans – who are also imperfect.

The success of the high-throughput methodology championed by the pharmaceutical industry has caught the attention of other industries and communities who also wish to accelerate their processing and screening techniques, including the alloy development community. Since the processing conditions of proteins and organic molecules generally differ from that of steels and superalloys, alternative high-throughput techniques have been employed to quickly synthesize and evaluate metal alloys. One of the oldest high-throughput techniques used for alloy development is the use of diffusion multiples. Diffusion multiples are formed by pressing multiple materials together and heating them in an inert environment to bond the materials together and allow elements from each material to interdiffuse with one another. Historically, diffusion multiples containing two or three elements have been used widely to determine diffusion coefficients and construct phase diagrams for new materials. However, in addition to determining diffusion kinetics of element A in element B (and vice versa), if elements A and B both have a similar crystal structure and mutual solubility then a continuous gradient of A-B alloys can be formed within the diffusion couple. Since many modern characterization techniques are able to probe small volumes of material ($\lessapprox 1\ \mu m^3$), by probing these chemically graded regions, properties such as hardness, elastic modulus, and thermal conductivity can be measured for many different alloy compositions within a single

sample [102]. While such techniques are most easily applied to two- and three-element diffusion multiples (i.e., diffusion couples, triplets, respectively) due to geometric limitations, it is also possible apply these techniques to higher order systems, such as high-entropy alloys. Figure 12 provides one such example, in which a five-element diffusion multiple is formed at the triple point of two binary, equimolar alloys (FeMn and CoNi) and pure Cr to examine the compositional neighbors of the Cantor alloy (CoCrFeMnNi) [103].

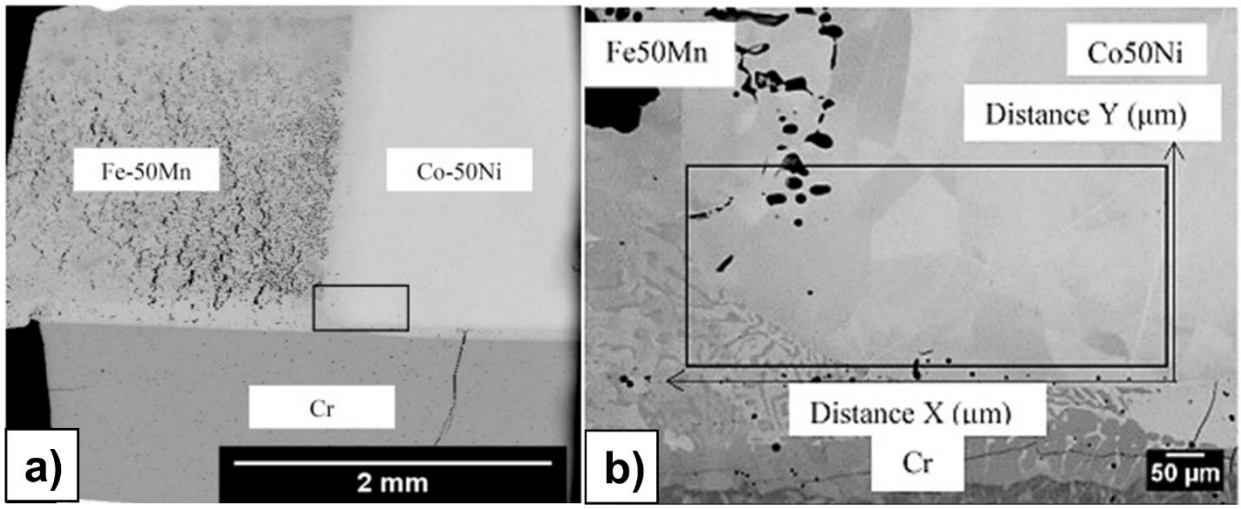

***Figure 12**: SEM imaging of a Co-Cr-Fe-Mn-Ni diffusion multiple produced at the triple point of binary equimolar FeMn and CoNi with Cr at a) low magnification and b) high magnification. Adapted from [103]*

While diffusion multiples are able to produce many different alloy compositions, they are limited by which elemental combinations can be used and by their difficulty, or inability, to produce specific, desired alloyed compositions. For example, should two or more elements form an intermetallic compound at their interface, such a compound can prevent the formation of a smooth compositional gradient across the interface. Additionally, if the interdiffusion coefficients between two elements in the diffusion couple are vastly different, the net flux of atoms across the interface can lead to Kirkendall voiding in one of the materials [104], which can impact many of the properties of the material (e.g., mechanical properties) which one may wish to test. Lastly, by relying on diffusion to naturally occur to produce the compositional gradients necessary to make this a high-throughput alloy synthesis technique, the experimenter is left to the mercy of nature regarding the smoothness or the sharpness of the compositional gradient, which can further

complicate the characterization process. To avoid relying on diffusion alone to produce compositional gradients, other high-throughput synthesis techniques have been developed which allow researchers to arbitrarily select the compositional range they wish to produce. One such technique that achieves this is combinatorial thin-film (CTF) synthesis. CTF synthesis, illustrated in Figure 13, uses sputter guns at off-normal angles to the substrate to deposit gradients of material across the substrate. By adjusting the positions and angles of the sputter guns and the substrate relative to one another, a researcher can select the range of compositions that are desired and then produce a thin film whose composition smoothly varies across the substrate, with each location containing a unique alloy composition. CTF synthesis has been used to produce "materials libraries" which have been successfully used to search for alloys across large compositional ranges and map properties including shape-memory transition hysteresis, catalytic activity, and hydrogen storage capacity, as well as mechanical and optical properties [105]. Owing to their compositional flexibility and smooth, controllable gradients, CTFs are already being used to explore the HEA composition space [50, 106, 107]. However, even CTFs struggle to meet the needs of mapping the irradiation response of materials, specifically, due to the nanocrystalline nature of thin films. With columnar grains only tens of nanometers in diameter [107], the high density of grain boundaries in CTF materials will likely serve as such a potent sink for irradiation-induced defects, that voids and extended defect structures would be unlikely to form and any variation as a function of composition would likely be obfuscated.

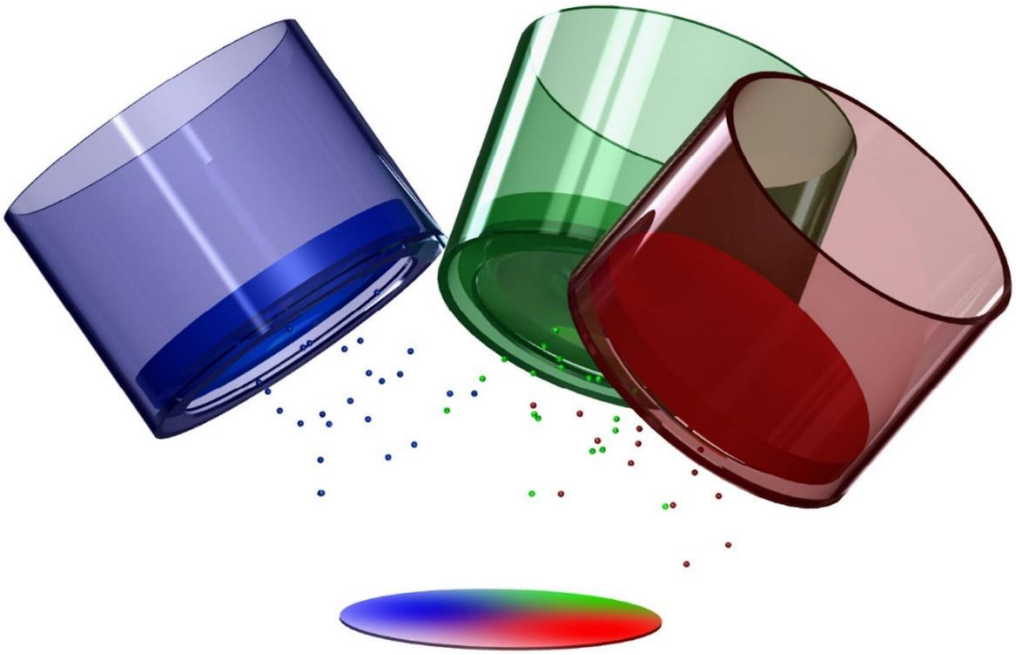

Figure 13*: Combinatorial thin-film (CTF) synthesis, wherein multiple sputter guns at off-normal angles to the substrate deposit gradients of material to produce a compositionally graded wafer [105].*

Unfortunately, neither diffusion multiples nor combinatorial thin films are particularly well suited for studying the microstructural evolution of materials under irradiation. In fact, any high-throughput synthesis technique which relies on compositional gradients is unlikely to be compatible with irradiation studies. Microstructural evolution under irradiation is dictated by the generation and diffusion of point defects (e.g., vacancies), meaning that any diffusion resulting from an engineered compositional gradient could become convoluted with the diffusion of defects generated under irradiation – potentially altering how the material performs under irradiation as compared to the same alloy in the absence of a compositional gradient. Indeed, the ideal high-throughput synthesis technique for irradiation studies would allow for samples of discrete, uniform compositions to be produced with microstructures comparable to that of traditionally manufactured materials. Currently the only other high-throughput synthesis techniques which are able to meet these criteria are multi-well arc melters, which can be filled with many different elemental mixtures to be melted in a single session, and rapid alloy prototyping (RAP), which uses a series of molds, and a vacuum induction melting (VIM) furnace outfitted with a load lock to enable multiple alloys to be cast during the same operation [108]. Unfortunately, both of these techniques would be considered to be on

the lower end of “high-throughput” in that they both require the precisely weighing of precursor materials beforehand which can be time consuming. Moreover, even if such techniques were used to produce large quantities of individual samples, the subsequent irradiation of the samples, for example at an ion accelerator facility, would still have to be performed one-by-one. Thus, high-throughput synthesis alone does not solve the challenge of screening materials for nuclear applications, high-throughput irradiation techniques must also be developed, and both the synthesis and irradiation techniques must be compatible with one another.

1.6 Addressing the Challenge

With the threat of anthropogenic climate change looming large alongside a growing demand for energy, the need for reliable, non-carbon-intensive power generation is enormous – and nuclear power will need to play a major role in the solution. With the development of advanced reactor technologies, including sodium-cooled fast neutron reactors and molten-salt reactors, net-zero-carbon energy generation can be realized while simultaneously recycling spent fuel from the current reactor fleet thereby reducing the volume of high-level radioactive waste which requires storage in a geological repository. While such advanced reactors offer both safety and efficiency gains, they come at the cost of subject materials to environmental conditions which are harsher than that of any reactor currently in the US fleet. Specifically, higher temperatures and higher irradiation damage levels are likely to push current code-qualified materials into a regime of increased void swelling while in-reactor, which can lead to mechanical failure and jeopardize the ability to maintain a coolable reactor geometry. To meet these material demands, new materials are being searched for and a particular set of alloys, high-entropy alloys (HEAs), appears to exhibit promising characteristics under irradiation – namely an increased resistance to void swelling. Developing new alloys and qualifying them for nuclear applications is an exceedingly time-consuming process, and HEAs have the misfortune of occupying the center of the alloy composition space, where there is the least experimental data to rely on and where models and simulations encounter the greatest levels of uncertainty. To rapidly explore and generate data on novel alloy compositions, high-throughput techniques

have been previously deployed and met with great success in mapping out the properties of a large range of alloy compositions, including HEAs. However, due to the unique material requirements for performing representative irradiation experiments, no current high-throughput techniques are suited for examining the microstructural evolution of materials under irradiation.

To fill this technological gap, the work hereinafter details the development of a new high-throughput methodology for rapidly producing alloys of arbitrary compositions, in arbitrary geometries, and with microstructures amenable for studying the effects of alloy composition on the irradiation response of a material. Since high-throughput synthesis alone does not alleviate the time-consuming process of alloy development for nuclear applications, systems enabling high-throughput irradiation experiments have been successfully designed, constructed, and tested at the University of Wisconsin-Madison Ion Beam Laboratory. Lastly, to complete the process of accelerating the alloy screening process, high-throughput and automated characterization techniques have been applied to examine the microstructural response of nearly 100 alloys after having been synthesized and irradiated using these newly developed techniques.

Each subsequent chapter has been adapted from a journal article written (first author) by Michael Moorehead, which has either been published or is in submission, as noted at the beginning of each chapter. Funding for this research was provided in part by the DOE Office of Nuclear Energy's Nuclear Energy University Program (DE-NE0008678, DE-NE0009001). This research was also funded in part by a fellowship program sponsored by the Nuclear Regulatory Commission (NRC) and was made possible with support from an NEUP Infrastructure grant and from continued support from the Nuclear Science User Facilities (NSUF) program. Additive manufacturing work using the LENS MR-7 was made possible through funding from the Grainger Institute for Engineering and NSF DMREF award #1728933. Use of facilities and instrumentation at the UW-Madison Wisconsin Centers for Nanoscale Technology (wcnt.wisc.edu) was partially supported by the NSF through the University of Wisconsin-Madison Materials Research Science and Engineering Center (DMR-1720415).

2 In situ Alloying via Additive Manufacturing

This chapter features direct content from the following journal article(s) first-authored by the PhD candidate:

M. Moorehead, K. Bertsch, M. Niezgoda, C. Parkin, M. Elbakhshwan, K. Sridharan, C. Zhang, D. Thoma, A. Couet, **High-throughput synthesis of Mo-Nb-Ta-W high-entropy alloys via additive manufacturing**, Materials & Design, 187 (2020) 108358.

2.1 Introduction and Motivation

Unlike conventional alloys, which typically comprises a single primary element with minor alloying elements added to modify the properties, HEAs are composed of multiple principal elements often in near-equimolar ratios. An alloy is commonly considered to be an HEA if it has multiple principal elements present in concentrations between 5 at% - 35 at% [41]. Beyond novelty, HEAs have gained interest for their promising properties including enhanced irradiation resistance [76], high-temperature strength [109], and corrosion resistance [110]. Individual HEAs have previously been synthesized using arc melting [111], spark plasma sintering (SPS) [112], mechanical alloying (MA) [113], and physical vapor deposition (PVD) [114], among other classical metallurgical techniques. However, the vast space of possible compositional variants under the HEA definition makes synthesis, characterization, modeling, and optimization of HEA compositions impractical using conventional methods. Development of accelerated, high-throughput techniques for the production and screening of novel alloys, such as HEAs, is thereby necessary if the development of compositionally complex alloys is to progress efficiently.

To date, most high-throughput alloy synthesis techniques rely on producing compositional gradients to form a range of alloy compositions, as is the case for diffusion multiples [102, 103], combinatorial thin films [115-118], additively manufactured gradients [45, 119, 120], combustion synthesis [121], and in situ nanotip melting [122]. Inherently, this limits the usability of these materials for materials

testing and characterization since a single composition of interest typically only exists in a vanishingly thin 1D line or 2D plane. Moreover, the chemically graded structures are thermodynamically unstable which minimizes their utility for testing at elevated temperatures where diffusion is no longer negligible. More recent work has sought to produce arrays of discrete material compositions by depositing varying amounts of a single elemental powder onto a metallic substrate and alloying the powder into the substrate by laser melting [123], however, such techniques are limited to producing patches of alloyed material at the surface of the substrate whose compositions cannot be varied independently from the substrate material. Consequently, the need exists for high-throughput synthesis techniques capable of producing bulk (3D) samples of freely chosen compositions, with microstructures that more closely resemble that of industrial materials.

Using HEAs as a venue for developing such high-throughput techniques, this work seeks to extend high-throughput materials synthesis to bulk materials such that it may be coupled with existing high-throughput characterization and modeling techniques. Specifically, implementation of additive manufacturing and the further development of in situ alloying techniques have enabled the *printing* of different HEA compositions, in 3D-component arrays, on a single build plate. The printing of such arrays on a single plate has enabled the use of high-throughput microstructural characterization techniques, the results of which will be presented herein, in addition to enabling future high-throughput testing of compositional arrays.

2.2 Methods and Materials

To rapidly produce arrays of different HEA compositions, additive manufacturing in the form of directed energy deposition (DED) was performed using an Optomec LENS MR-7, schematically represented in Figure 14. The LENS MR-7 is a powder-based metals 3D printer operating in a closed chamber filled with argon and fed by four independently controlled powder hoppers. Powders from each hopper are drawn into a gas line of flowing argon by the rotation of an auger located at the base of each hopper. These powders are aggregated in a central gas line and consequently mixed by the turbulent gas

flow during transit to the printhead. At the printhead, the mixed powder is sprayed out by four nozzles, with rotational symmetry about the optic axis of the printhead, where it encounters a laser impinging on the surface of the build plate. The laser, with an approximate spot size of 600 μm and focal point ~380 μm below the surface, forms a melt pool on the surface of the build plate where incoming powder heated by the laser becomes incorporated. This melt pool can then be dragged across the surface of the build plate, by moving the stage it is affixed to, leaving behind solidified material in its wake. A continuous solid/liquid interface is maintained as the laser moves along the build path, and cooling rates in excess of 10^3 K/s can be obtained in 3D geometries [124]. By steering the path of the laser across the surface of the build plate through stage movements, material can be deposited in arbitrary geometries.

For this research, hoppers in the LENS MR-7 were each filled with a single elemental powder, either Mo, Nb, Ta, or W. These elements were selected to produce compositions near that of the four-component equimolar HEA MoNbTaW, which has been previously shown to form a single-phase solid solution [125, 126]. Furthermore, this alloy is predicted to be stable over a broad temperature range [127, 128], reducing the likelihood of phase transformations, which can cause changes in geometry and additional stresses in the printed part. The choice of Mo-Nb-Ta-W alloys, while not specifically being proposed as candidate materials for any proposed reactor designs, serves as a stress test for the in situ alloying fabrication process; by using metals with the highest melting points on the periodic table, if the process is successful, it should be able to accommodate many other alloy systems with less demanding processing requirements. Lastly and most importantly, by maintaining separation of elemental powders prior to printing, access to any linear combination of the four elements is achievable.

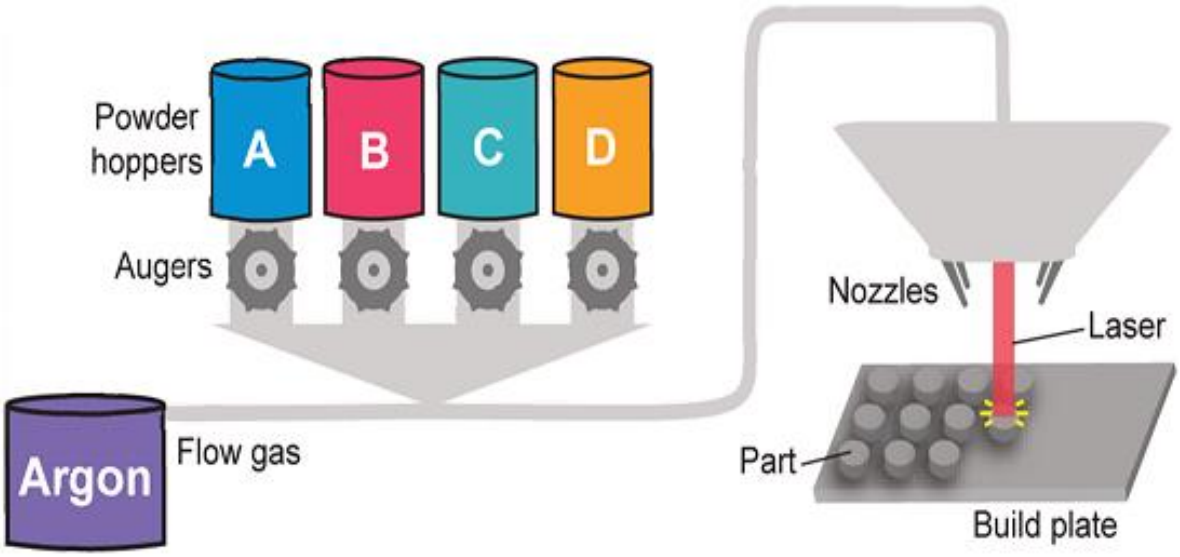

***Figure 14**: Schematic illustration of the LENS MR-7 system used in this study.*

Plasma spheroidized Mo, Nb, Ta, and W powders, each in the size range of ~45 μm – 150 μm (-100/+325 mesh), were procured from the company HC Starck and the morphology and size distribution can be seen in Figure 15. While broad size ranges of powders and the presence of irregularly shaped powders have been linked to defects, including lack-of-fusion porosity, in additively manufactured parts using powder-bed techniques [129, 130], it is still unclear that this relationship applies to parts manufactured through DED techniques, which feature blown powder, higher laser powers, and slower scan speeds. For this work, the size range of powders recommended by the LENS manufacturer was used to ensure proper functioning of the powder handling components.

Nominal dimensions of the printed parts were 6.35 x 6.35 x 3.175 mm, comprised of five print layers each with a hatch spacing of 0.381 mm; the hatch pattern was rotated 60° between each layer. The Z step size was 0.254 mm, however in practice the deposited layer height was approximately twice this, depending on composition. To ensure sufficient homogeneity, after the final deposition pass, a remelting pass was performed whereby the laser was rastered across the sample surface without being fed powders from the hoppers. Deposition passes were performed with a laser power of 800 W and a scan speed of 25.4 cm/min and remelting passes were performed with a laser power of 1000 W and a scan speed of 177.8

cm/min. The increased scan speed was found to be necessary to avoid high back reflection from the laser. The total time required to set the composition of, print, and remelt a single sample stub was less than five minutes. All sample stubs were printed onto 316 stainless steel build plates (100 x 100 x 6.35 mm). The argon atmosphere was sampled continuously throughout each printing campaign, and the measured oxygen concentration was reduced to <10 ppm before printing. However, after the onset of printing, the measured oxygen concentration quickly dropped to <1 ppm, due to oxygen gettering by the printed material, and remained at this level for the duration of each printing campaign.

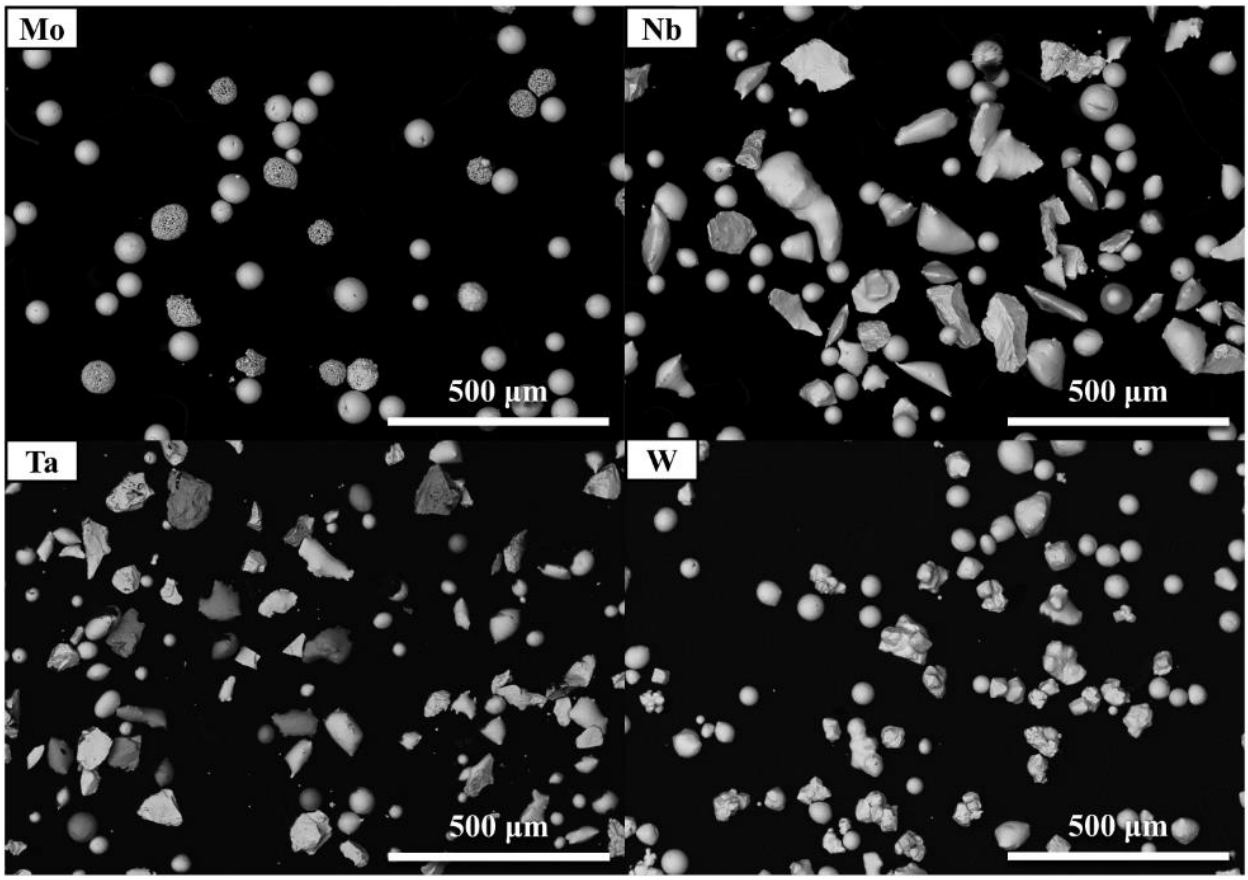

Figure 15*: Backscatter SEM images of Mo, Nb, Ta, and W powders used in this study, sourced from HC Starck.*

In this work, calibrations were performed to measure the mass flow rate of each elemental powder as a function of auger RPM for their respective hoppers, the results of which were used in final build composition predictions. Three printing iterations producing a total of 40 sample stubs were performed. 31

samples are included in the analysis hereinafter as the remaining samples were produced as part of other parameter optimization experiments. In each iteration, all printing parameters were kept constant except the powder hopper RPM, which was varied to produce different compositions while maintaining a total atomic flow rate of ~0.1 mol/min (~12-15 g/min) for each composition.

Arrays of printed samples were imaged using a JEOL JSM-6610 scanning electron microscope (SEM) at the Wisconsin Nanoscale Imaging and Analysis Center, equipped with energy-dispersive X-ray spectroscopy (EDS) for chemical analysis. Phase identification was performed using X-ray diffraction (XRD) with a Bruker D8 Discover. Lattice parameters were calculated from extrapolation of the Nelson-Riley function using collected XRD data [131]. All initial microstructural characterization (XRD, SEM, EDS, etc.) was performed non-destructively without removing samples from the build plate. After initial characterization, 2-3 samples from each build plate were removed and polished for more in-depth microstructural and chemical analysis using SEM and EDS.

For comparison of the additively manufactured microstructure with that of conventional metallurgy, a ~50-g ingot of the equimolar MoNbTaW HEA was cast using an Arcast Arc200 arc melter. Precursor materials were elemental foils of Mo and Ta, small billets of Nb, and W wire, all >99.9% in purity. The cast ingot was flipped and remelted multiple times to ensure macroscopic chemical homogeneity.

In addition to experimental work, high-throughput computational methods were employed to assess the phase stability of the HEA compositions produced via additive manufacturing. The CALPHAD (CALculation of PHAse Diagrams) approach was chosen for its relative accuracy and computational efficiency in calculating equilibrium phases by applying an energy-minimization procedure to large thermodynamic databases of Gibbs energies, as a function of temperature, pressure, and composition [132, 133]. Specifically, the computation software, PanDat^{TM} [134], equipped with a high-throughput calculation (HTC) tool, was used to develop quaternary phase diagrams in the Mo-Nb-Ta-W composition space.

2.3 Results

For reference, pictures of the build plates from each printing iteration are shown in Figure 16. The top surfaces of the printed sample stubs were found to be wavy, but smooth and reflective suggesting minimal oxidation has occurred during synthesis. The height variation within a single stub is not thought to be substantial enough to impact chemical or crystallographic measurements by energy-dispersive spectroscopy (EDS) or X-ray diffraction (XRD), however samples would likely need to be mirror polished for meaningful further irradiation, corrosion, and mechanical testing.

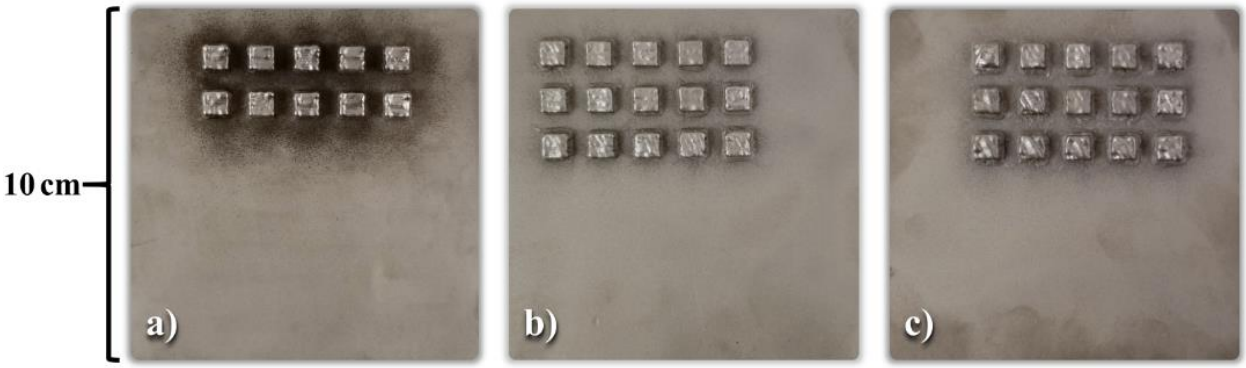

Figure 16*: Build plates featuring Mo-Nb-Ta-W arrays from the a) first, b) second, and c) third printing iterations. Note: for clarity, build plates from the second and third iterations were sand blasted before imaging.*

2.3.1 Compositional Predictions

One challenge of alloying elemental powders in situ is controlling the final composition of the built part. The difficulty is that several variables such as elemental vapor pressure, powder geometry, powder reflectivity, elemental mixing enthalpies, etc. can affect how the powders absorb energy from the laser and how much of the material enters the melt pool and mixes. The result is that often the composition of the powder exiting the nozzles of the 3D printer is not necessarily the composition of the final part. As such, multiple iterations of printing and prediction refinement were necessary to narrow the gap between actual compositions (measured from EDS line scans across the sample surface) and predicted compositions, the results of which are shown in Figure 17.

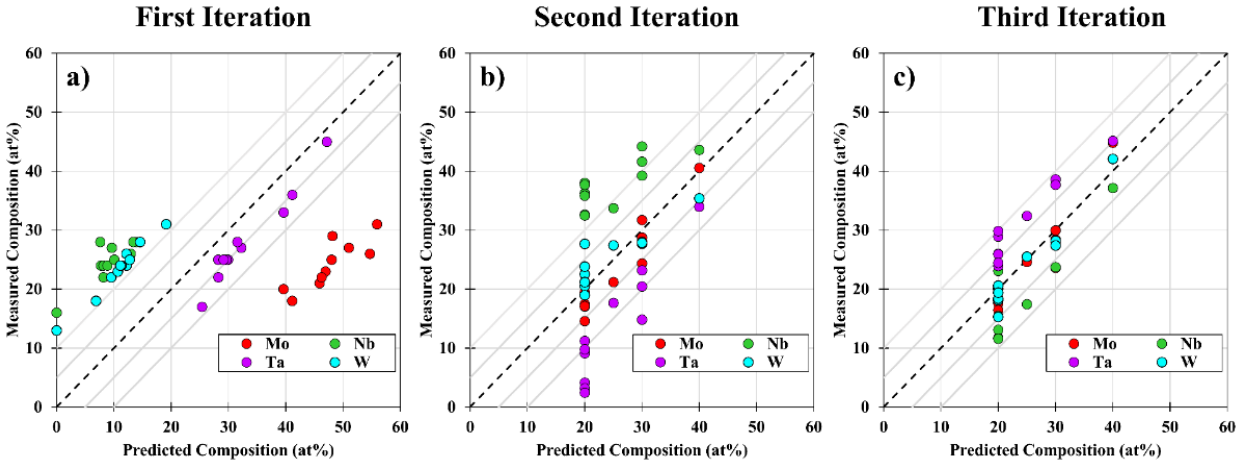

Figure 17*: Measured composition of additively manufactured sample stubs versus the predicted composition for the a) first, b) second, and c) third printing iterations. The black dashed line denotes a 1:1 prediction while the light gray lines adjacent are ±5-at% and ±10-at% contours.*

First Iteration

The predicted compositions for the first printing iteration were based solely on the mass flow rate versus powder hopper RPM calibrations, performed separately for each element. The result of each powder calibration experiment is a relationship shown by Eq. (1).

$$\dot{m}_i = \alpha_i * (RPM)_i + \beta_i \quad (1)$$

Here, $\dot{m}_i$ is the mass flow rate of element *i* which is related to the RPM selected for that powder hopper by experimentally determined coefficients α_i and β_i. While a non-zero value for β_i would not seem intuitive (as this would imply a non-zero mass flow rate while the powder hopper is idle), most of the elements studied had value for β_i whose magnitude was non-negligible. Possible reasons for this include a potential minimum RPM for the stepper motor which would be necessary for smooth, continuous auger rotation. From the mass flow rate measurements, the mass fraction, w_i, of species *i* in the incoming powder is simply the ratio of the mass flow rate of species *i* over the total mass flow rate as shown in Eq. (2).

$$w_i = \frac{\dot{m}_i}{\sum_{i=1}^{n} \dot{m}_i} = \frac{\alpha_i * (RPM)_i + \beta_i}{\sum_{i=1}^{n} [\alpha_i * (RPM)_i + \beta_i]} \quad (2)$$

Similarly, from Eq. (2), using M_i as the molar mass, the atomic fraction, x_i, of species *i* can be written as shown in Eq. (3).

$$x_i = \frac{M_i * \dot{m}_i}{\sum_{i=1}^{n} M_i * \dot{m}_i} = \frac{M_i * [\alpha_i * (RPM)_i + \beta_i]}{\sum_{i=1}^{n} M_i * [\alpha_i * (RPM)_i + \beta_i]} \quad (3)$$

For the first printing iteration, compositions near the equimolar MoNbTaW composition were explored by varying the powder hopper RPMs using Eq. (1). These measured sample compositions were compared retroactively to the compositions predicted using Eq. (3) and are shown in Figure 17a. Here it can be seen that the actual sample compositions are greatly depleted in Mo and enriched in Nb and W compared to the predictions. While likely caused by several phenomena occurring in concert, previous studies have observed similar trends with Mo and Nb, which were attributed to the relatively high vapor pressure of Mo leading to volatilization as well as the relatively low melting point of Nb leading to preferential melting [135]. The enrichment of W, however, is not easily explained by trends in melting point or vapor pressure and may instead be a result of other extrinsic characteristics of the W powder, such as the morphology or reflectivity, though this remains speculative at this point.

Second Iteration

Rather than mounting a bottom-up campaign to determine the powder and system characteristics that give rise to the discrepancies between the predicted and measured sample stub compositions, a top-down approach was taken by lumping all of the effects into a single fitting term, *R*, dubbed the *retention rate*. Using this fitting parameter, the predicted atomic fraction of each element in the printed material can be written as shown in Eq. (4).

$$x_i = \frac{R_i * M_i * \dot{m}_i}{\sum_{i=1}^{n} R_i * M_i * \dot{m}_i} = \frac{R_i * M_i * [\alpha_i * (RPM)_i + \beta_i]}{\sum_{i=1}^{n} R_i * M_i * [\alpha_i * (RPM)_i + \beta_i]} \; ; where \; 0 \leq R_i \leq 1 \quad (4)$$

The retention rate for each element was then calculated by performing a least-squares fit on Eq. (4) using the measured compositions from the first printing iteration, α_i and β_i values from the mass flow rate calibration experiments, and input RPMs.

For the second iteration, all possible compositions of the $A_{20}B_{30}C_{20}D_{30}$ type (e.g. $Mo_{20}Nb_{30}Ta_{20}W_{30}$, $Mo_{30}Nb_{30}Ta_{20}W_{20}$, etc.), the $A_{20}B_{20}C_{20}D_{40}$ type (e.g. $Mo_{20}Nb_{20}Ta_{20}W_{40}$, $Mo_{20}Nb_{40}Ta_{20}W_{20}$, etc.), and the equimolar composition were targeted. Using R_i values calculated from applying Eq. (4) to the data from the first printing iteration, the RPMs necessary to achieve these final compositions were calculated proactively and used for printing the second iteration. Comparison of the measured compositions and the predicted compositions for the second iteration are shown in Figure 17b. Here the data is organized into columns (a direct result of the targeted compositions) and improvements have been made over the first iteration: Mo and W are within ±10 at% for all targeted compositions and while Nb is overrepresented and Ta is underrepresented, there are several compositions which also fall within the ±10 at% range.

Third Iteration

While the second iteration provided better predictability over using powder flow rate measurements alone (compare Figure 17a and Figure 17b), there is still substantial variation in the actual final compositions with respect to their predictions. To further improve the predictive capability, for the third iteration the previous experimentally determined mass flow rate coefficients (α_i and β_i) in addition to the retention rate (R_i) were used as fitting parameters; additionally, the constraint of $0 \leq R_i \leq 1$ was removed. To refine these fitting parameters, the least-squares fit of Eq.4 was then repeated using input RPMs and measured compositions from the second iteration. With the fitting parameters redefined, RPMs necessary to produce the same target compositions from the second iteration were calculated and used for printing the third iteration.

Following the same procedure as before, the actual compositions of each sample stub were measured using EDS and compared to the predicted compositions, the results of which are shown in Figure

17c. Here a marked improvement is seen in the predictability: both Mo and W are within ±5 at% for all targeted compositions and both Nb and Ta are within ±10 at% for all targeted compositions. The RPMs used for each printed stub, as well as the predicted and measured chemical compositions, are given explicitly in Table 7.1 in the Appendix.

2.3.2 Surface Morphology and Chemical Analysis

The as-fabricated top surface of each sample stub was imaged using SEM. Both the as-fabricated top surface and the polished top surface of a sample stub near the equimolar MoNbTaW composition are shown in Figure 18a and Figure 18b, respectively. The as-fabricated surface morphology exhibits a weld-like pattern that shares the same dimensions and directionality as the remelting raster pattern. After mechanical polishing, the grain structure is revealed and exhibits a cellular solidification structure within the grains. Additionally, most of the sample stubs exhibited minor intergranular cracking, likely caused by the thermal stresses from cooling from temperatures greater than 3500 °C (necessary to melt tungsten) to room temperature in seconds. Importantly, little to no retained unmelted powder was observed in the remelted region on the top surface of the sample which validates the necessity of laser remelting.

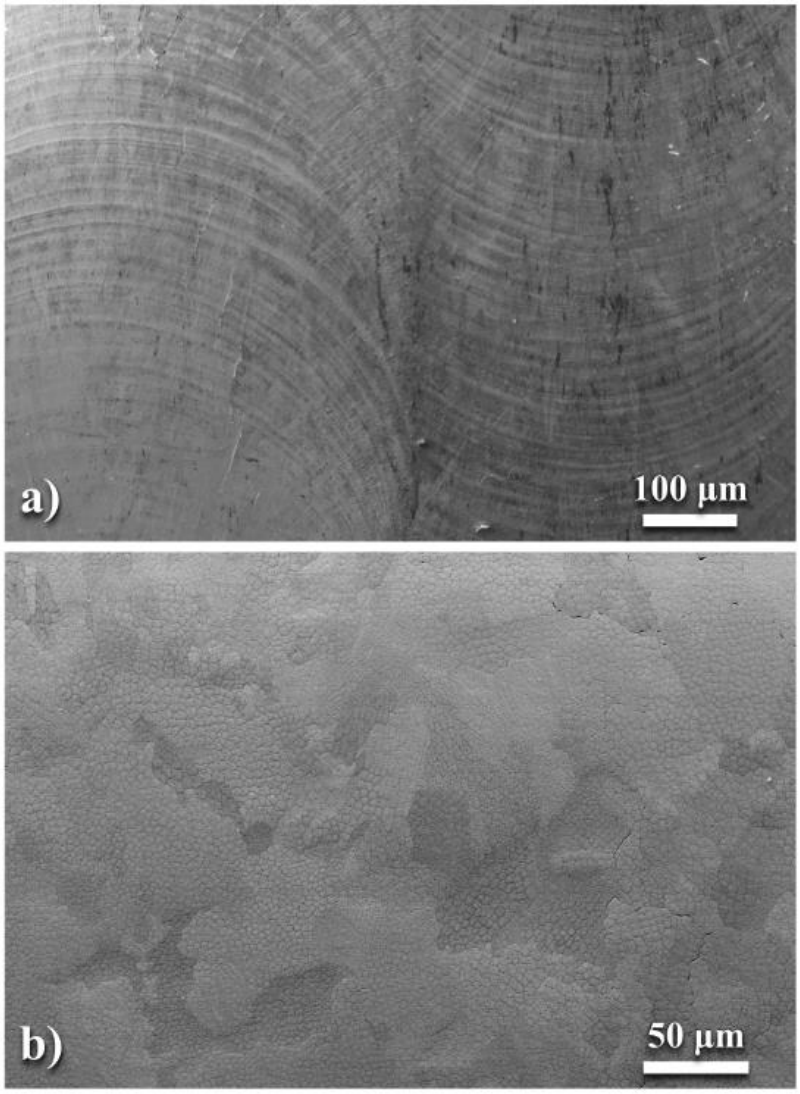

Figure 18*: SEM image of a) as-fabricated top surface and b) polished top surface of additively manufactured nearly equimolar MoNbTaW sample. Sample BR3 in Table 7.1 in the Appendix.*

In addition to performing broad EDS line scans to determine the average composition of each sample, EDS chemical mapping was performed at higher magnification to assess the micro-segregation of alloying elements. Figure 19 shows the elemental distribution of both the additively manufactured and arc-melted equimolar MoNbTaW produced for comparison.

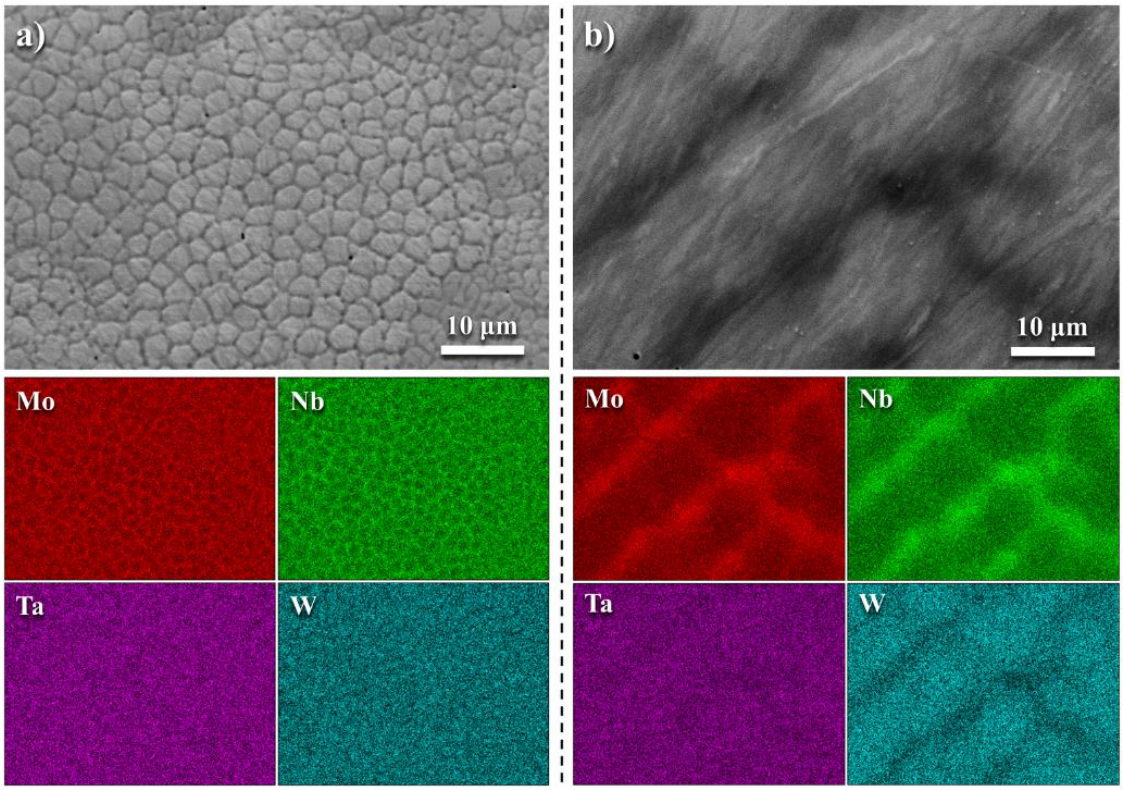

***Figure 19**: SEM image and EDS chemical mapping of equimolar MoNbTaW produced through a) additive manufacturing (sample BR3 in Table 7.1 in the Appendix) and b) arc melting. Note: the images are taken at the same magnification to illustrate the extent of chemical segregation.*

Generally speaking, from thermodynamics of solidification, segregation of solute elements will occur as a result of a difference in solubility of these elements in the liquid and solid phases. While thermodynamically driven, the length scale over which this occurs is dictated by solidification kinetics and specifically the degree of undercooling which can be related to the cooling rate of the system [136]. As may be expected, the length scale of the cellular structure in the additively manufactured material is much finer than the dendritic structure in the arc-melted material which is indicative of a faster cooling rate in the case of the additively manufactured material. Both the additively manufactured and arc-melted equimolar MoNbTaW HEA exhibited similar differences in chemical composition between the inter- and intra-cellular/dendritic regions of the as-solidified microstructure. These local compositions, measured by EDS,

are given in Table 2.1 and are in good agreement with measurements on arc-melted MoNbTaW from literature [137].

***Table 2.1**: Comparison of local chemical composition measured by EDS of equimolar MoNbTaW synthesized by additive manufacturing and arc melting.*

	Additively Manufactured		Arc Melted	
Region	Intracellular	Intercellular	Intradendritic	Interdendritic
Mo (at%)	23 ± 2	26 ± 2	22 ± 2	25 ± 2
Nb (at%)	23 ± 2	31 ± 2	23 ± 2	32 ± 2
Ta (at%)	25 ± 2	21 ± 2	26 ± 3	24 ± 3
W (at%)	29 ± 3	23 ± 3	29 ± 3	19 ± 3

The length scale of the chemical segregation is particularly relevant when seeking to homogenize the material through heat treatment. Using $x \approx 2\sqrt{D \cdot t}$ as an estimate for the diffusion length and assuming the interdiffusion coefficients of the two alloys are comparable, the difference in time required to homogenize each alloy can be estimated. From inspection of Figure 19, the interdendritic spacing of the arc-melted material is estimated to be ~4-5 times greater than the intercellular spacing in the additively manufactured material. This would suggest that the arc-melted material would take ~16-25 times *longer* to homogenize than the additively manufactured material.

2.3.3 Phase Characterization

X-ray diffraction (XRD) was performed on each sample stub from the arrays, the resulting patterns of which are shown in Figure 20 with intensities normalized to the first major peak. Each pattern consists of purely BCC peaks without additional signals from otherwise forbidden reflections which would be indicative of ordered phases; as a result, each composition was determined to be a disordered BCC solid solution. Of note is the variation in relative intensity of the diffraction peaks within a given diffraction pattern which may be caused by texturing or the relatively large grains seen in Figure 18, leading to only a small number of grains being interrogated. Indeed, it is not uncommon for additive manufacturing techniques to produce a textured structure or large grains when depositing using high energy densities [138].

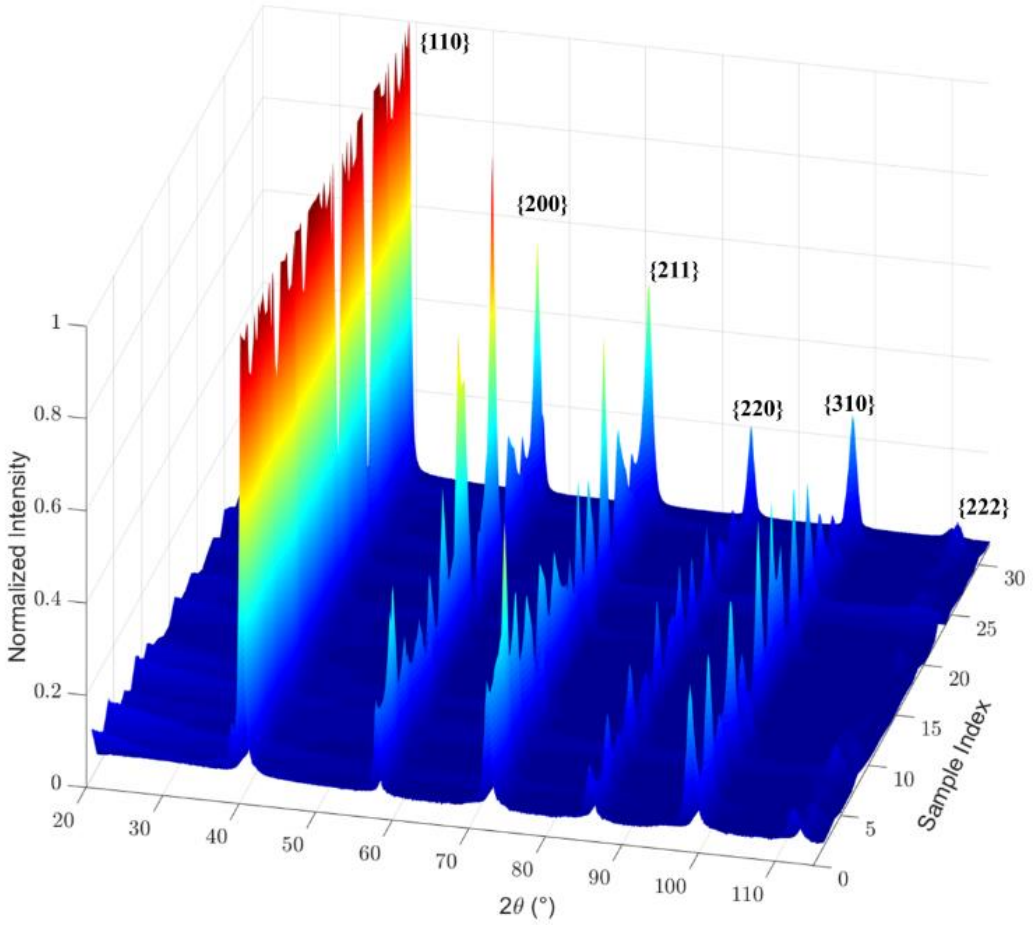

***Figure 20**: Composite image of XRD patterns from the 31 sample stubs analyzed. All samples appear to exhibit only a single-phase, disordered BCC crystal structure.*

From the XRD patterns, lattice parameters of each alloy were calculated by performing a Nelson-Riley regression on the lattice parameters calculated from each reflection within a pattern [131]. Additionally, since each composition forms a solid solution, the expected lattice parameter can be calculated from a weighted average of the constituent elements (Vegard's law) which has been performed and listed for each sample alongside the measured lattice parameter in Table 7.1. As may be expected, ~95% of the measured lattice parameters were within 0.5% of the lattice parameters predicted using Vegard's law - the measured lattice parameter of only one sample was found to deviate more than 1% from Vegard's law.

While every printed sample was experimentally found to consist of a single disordered BCC structure, as expected from high-temperature CALPHAD calculations, it is not known whether this is the

thermodynamically stable phase for each composition at lower temperatures, as only the equimolar MoNbTaW HEA has been studied extensively in literature [125-128]. To elucidate this, high-throughput CALPHAD calculations were performed over the Mo-Nb-Ta-W composition space using PanDat^{TM}, spanning all composition bound by 5 at% to 50 at% for each element, with a step size of 5 at%, to determine the stable phases at 300 °C. The resultant stable-phase predictions for each composition were used to produce a quaternary phase diagram, shown in Figure 21 with the compositions of the additively manufactured samples superimposed. Here, it can be seen that Nb acts to stabilize the single disordered BCC phase while Ta acts to destabilize the single disordered BCC phase, leading to phase separation and formation of an ordered BCC secondary phase. The vast majority of the alloys produced as part of this study are predicted to remain thermodynamically stable as a single disordered BCC at 300 °C, however, some Ta-rich and Nb-poor compositions are predicted to form second phases. Under normal conditions, the formation of these second phases would not be expected due to the slow diffusivity of refractory metals at lower temperatures, however, in a kinetically driven system (such as under irradiation) it may be possible for such phases to form which could potentially lead to changes in material properties such as hardening and embrittlement. It is noted that results from CALPHAD calculations of refractory HEA compositions at low temperatures must be used conscientiously, as many of the chemical potentials used for these calculations are the result of extrapolations from higher temperatures and more dilute concentrations [139], which can lead to greater uncertainties – thus necessitating experimental validation through long-term aging experiments.

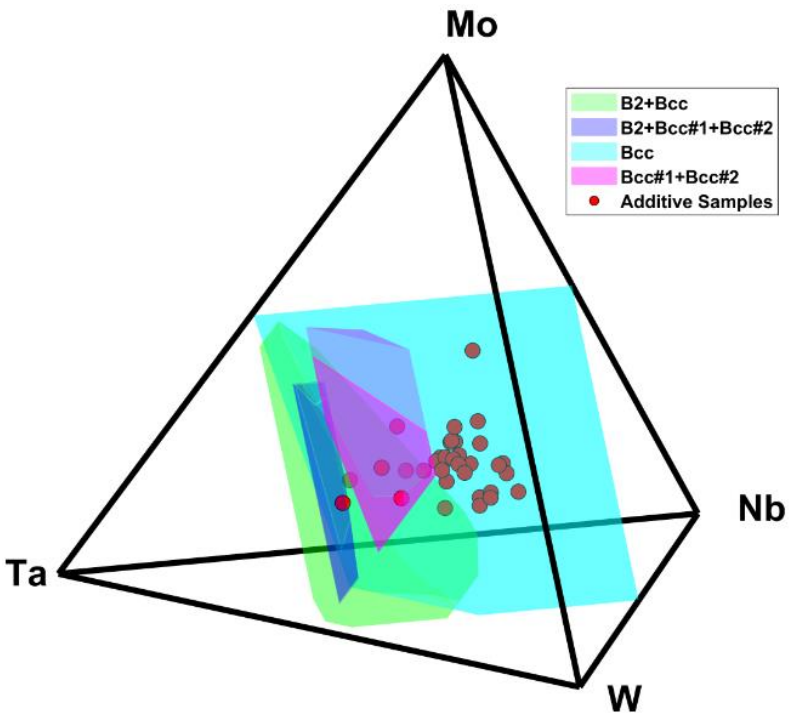

***Figure 21**: Quaternary phase diagram of Mo-Nb-Ta-W system at 300 °C as calculated using high-throughput CALPHAD calculations.*

2.4 Discussion

2.4.1 Printing Considerations

Although visual inspection of the as-built materials revealed cracking along the build-plate/sample interface visible in Figure 16, the samples remained well adhered to the build plate. Such cracking is to be expected given the thermal stresses produced during additive manufacturing especially with the difference in coefficient of thermal expansion (CTE) between the stainless-steel build plate and the refractory samples; the CTE of 316 stainless steel is 2-3x greater than that of Mo, Nb, Ta, and W at room temperature [140]. Future printing campaigns will attempt to match the thermo-mechanical properties of printed material with build-plate material selection to minimize thermal stresses where possible, for example, by using pure Mo, Nb, Ta, or W build plates when printing with these elements.

A common challenge encountered when printing with elemental powders is the incorporation of unmelted powder, and overall lack of chemical homogeneity in the final product [135, 141-143]. This

problem can become more pronounced when working with high-melting-point materials as was observed in preliminary experiments in the Mo-Nb-Ta-W system as part of this study. Previous studies have combatted this problem by using either pre-alloyed or pre-mixed powder [144-146] or by introducing remelting passes during printing [135, 147, 148]. Unfortunately, the use of pre-alloyed or pre-mixed powder immediately limits the ability to rapidly explore different alloy compositions, thus in this work laser remelting was used to preserve this capability.

Unmelted powder retention was first minimized in this work by adjusting printing parameters such as lowering powder flow rates, increasing laser power, lowering scan speed, and decreasing hatch spacing, specifically to increase the amount of energy deposited per unit mass of powder and the time each location remains molten during printing. Nevertheless, unmelted powder was still observed to the extent that laser remelting was still deemed necessary. In the interest of synthesis time, only a single laser remelting pass at the end of the build was used to produce a homogeneous layer. This was motivated by future materials testing, such as ion irradiation, corrosion, and micromechanical testing, performed in the near-surface regions of the material. On the other hand, this remelting technique could be applied throughout the build process to ensure a larger extent of chemical homogeneity in the build depth. Sample stubs of the selected alloys were still required to be built several layers high to avoid artifacts from the interaction region with the substrate such as interdiffusion of substrate material into the final part.

When performing in situ alloying of elemental powders through additive manufacturing, it is also important to bear in mind that the composition of the powder being flown through the system may not necessarily be the composition of the final additively manufactured alloy. For example, to achieve the near-equimolar MoNbTaW composition in sample R8.1 (actual composition $Mo_{23}Nb_{24}Ta_{25}W_{28}$), the composition of the powder used was approximately 47 at% Mo, 9 at% Nb, 30 at% Ta, and 14 at% W. Previous work with this system has related this discrepancy to the melting point and vapor pressure of the different elements [135]. However, since numerous other factors including powder oxide thickness [149], powder size distribution [150], powder morphology [151], etc. can also affect the melting and spatial

distribution of elements in the final part, optimization through iterative trial prints appears much more tractable to achieve desired compositions in lieu of exhaustive bottom-up modeling efforts.

2.4.2 High-Throughput Implications

In addition to greatly expanding the variety of geometries that can be fabricated as compared to conventional metallurgy methods, additive manufacturing is similarly paving the way for alloy exploration. Since the number of possible alloy compositions increases dramatically with each additional constituent, and even more so by varying the concentration of each element in a system, most alloy development has occurred near to a singular base element, with few alloying additions. Thus, a vast space of potential alloys exists relatively unexplored, with high-entropy alloys residing at the heart of this new frontier.

The experiments presented herein have demonstrated how in situ alloying through additive manufacturing can be used to explore the HEA alloy space in a high-throughput manner. Using arc melting as a representative for conventional alloy synthesis techniques, the time savings of using in situ alloying through additive manufacturing for materials synthesis can be estimated semi-quantitatively with this study to be approximately one order of magnitude. Moreover, when considering the time necessary to homogenize arc-melted and additively manufactured materials through heat treatment, as shown in section 2.3.2, the total time savings increase to over two orders of magnitude when using in situ alloying. For the application of ion irradiation, corrosion, and micromechanical testing specifically, there is an additional time savings gained since all samples can be tested simultaneously without having to load and unload each sample one at a time. Similarly, the time required to polish each sample to a surface roughness acceptable per ASTM standard [152], is likely far greater than would be necessary to polish a sample array on a single build plate.

High-throughput alloy development, however, requires additional aspects beyond materials synthesis, including characterization and modeling, and in order to achieve a comprehensive understanding of the material in question, all three are needed. It is thus critical to match high-throughput alloy processing

rates for both fabrication and property characterization methods, as well as incorporate a high-throughput computational effort. Alongside the production of combinatorial thin films [115-118], additive manufacturing is one of the few synthesis methods versatile and fast enough to enable all three aspects to function synergistically in a high-throughput manner. Moreover, additive manufacturing affords many of the same flexibilities of combinatorial thin film synthesis while being able to produce bulk quantities of material (i.e., millimeters vs. micrometers of usable material) and can be readily scaled to produce larger volumes of material and different sample geometries as needed – a capability not available when using other high-throughput synthesis techniques.

The high-throughput synthesis and characterization methods employed in the work have also been used synergistically with CALPHAD modeling, via the software PanDat^{TM}, to assess the phase stability for the compositions printed from the Mo-Nb-Ta-W system. While modeling for this work was performed post facto, this need not be the case. Indeed, with the use of additive manufacturing, coarse modeling over large composition spaces could first be performed to determine regions of interest which could then be rapidly printed and characterized in a near-automatic fashion. In addition to microstructural characterization such as SEM, EDS, and XRD, other testing can be performed in a similar fashion such as resistivity measurements, micromechanical testing, and profilometry [153].

2.5 Conclusions and Future Work

In this work, high-throughput materials synthesis was combined with characterization and modeling techniques to form the framework for an accelerated approach toward alloy development using arrays of high-entropy alloys in the Mo-Nb-Ta-W system produced by in situ alloying of elemental powders through additive manufacturing. Use of separate elemental feedstock powders enabled the selection of any linear combination of the four elements, thus forming the basis for high-throughput alloy exploration and synthesis. Three printing iterations were performed to improve the predictive capabilities of the final sample compositions produced. By the third iteration, targeted compositions could be printed within ±5 at% for Mo and W and within ±10 at% for Nb and Ta. Sample stubs produced were subsequently characterized

using SEM, EDS, and XRD; all samples were found to be chemically homogeneous with minimal inclusions of unmelted powder and exhibit a single disordered BCC crystal structure. All characterization was performed non-destructively with samples remaining on the build plate, enabling future high-throughput testing to be performed using the same build plate. Additionally, the coupling of high-throughput synthesis and characterization techniques with high-throughput modeling was demonstrated using CALPHAD calculations via PanDat^{TM} to predict the equilibrium phases of each printed alloy composition at 300 °C. While nearly every composition printed was predicted to remain a single disordered BCC crystal structure at 300 °C, certain Ta-rich and Nb-poor compositions were predicted to form second phases – however, the slow diffusivity of refractory metals at this temperature would likely inhibit their formation in practice.

3 High-Throughput Phase Stability Assessment

This chapter features direct content from the following journal article(s) first-authored by the PhD candidate:

M. Moorehead, P. Nelaturu, C. Parkin, C. Zhang, A. Savan, J. Hattrick-Simpers, M. Elbakhshwan, K. Sridharan, A. Ludwig, D. Thoma, A. Couet, **Accelerated Phase-Stability Assessment of Cr-Fe-Mn-Ni High-Entropy Alloys via High-Throughput Aging**, Materials Today (2022), *submission pending*.

3.1 Introduction and Motivation

With in situ alloying via additive manufacturing (AM) having been demonstrated as a feasible means of producing "bulk" quantities of samples in the Mo-Nb-Ta-W system in a high-throughput manner, the next logical step is to apply the technique to an alloy system more relevant for nuclear applications and compare the results with other high-throughput synthesis techniques and simulation. In this pursuit, the Cr-Fe-Mn-Ni system is chosen as it covers all of the alloys which have been approved for use in high-temperature nuclear applications, as outline in the ASME Boiler and Pressure Vessel Code (BPVC), Section III, Division 5.

One particular area of interest in the study of HEAs and CCAs which is relevant to nuclear applications is phase stability. Many of these multicomponent alloys have gained attention for their unanticipated phase stability given the number of possible phases, including intermetallic compounds, which can form as dictated by the Gibbs phase rule [154]. Unfortunately, the vast majority of experimental work studying these alloys has been focused on materials in the as-cast condition which often exhibit non-equilibrium solidification structures such as dendrites and chemical segregation which are not necessarily representative of the thermodynamically stable phases over a given temperature range [42, 155]. Indeed, many of these seemingly single-phase compositions begin to phase separate and form precipitates when heat treated at intermediate temperatures (i.e., between 400-1000 °C) [156-159]. Such uncertainty in the equilibrium

phases of HEAs and CCAs serves as an impediment in their application to nuclear environments, since under irradiation, metastable alloys can be driven towards their phase fractions at thermodynamic equilibrium or, alternatively, chemical segregation and new phases can form at different temperatures depending on the competition between thermodynamic driving forces and the diffusion kinetics which are enhanced under irradiation. Indeed, to entertain the idea of using HEAs or CCAs in a reactor environment, it is necessary to know what the equilibrium phases are at multiple reactor-relevant temperatures, which for new alloys would typically require a battery of aging experiments which may be prohibitive for large numbers of alloys, due to both material and time requirements.

Since large-scale alloy synthesis and aging experiments can be costly and time consuming, many studies have been dedicated to using first-principles modeling and simulations to determine the stable phases of complex alloy systems at thermodynamic equilibrium [160]. However, most atomistic modeling techniques (DFT, Monte Carlo, MD, ab-initio, etc.) are not well suited to cover a broad array of different compositions in a computationally efficient manner. The disordered nature of CCAs further exacerbates the computational cost by often necessitating the simulation of multiple different supercell configurations [161] and larger-than-normal simulation volumes [128] to accurately describe the properties of the randomized systems [162]. By comparison, CALPHAD modeling is computationally fast enough for the task, however, it is reliant on databases of chemical potentials and must extrapolate to model composition and temperature combinations for which experimental data is unavailable [163], which can lead to greater uncertainties over atomistic modeling. Nevertheless, while these modeling techniques alone are able to shed light on the mechanisms which govern the thermodynamic properties of compositionally complex systems, to validate these models and advance alloy development, performing traditionally time-consuming experiments remains inescapable.

As research interest in CCAs and HEAs continues to grow, it is evident that whether performing standalone experiments or validating simulations, efficient exploration of the complex composition space requires the development and implementation of high-throughput synthesis and characterization

techniques. Of the high-throughput synthesis techniques previously applied to CCAs (including multi-material diffusion couples [164], friction stir welding [165], etc.) two techniques have been demonstrated to be particularly well suited for phase-stability assessments: combinatorial thin-film synthesis [166] and in situ alloying via AM, detailed in the previous section [167]. Combinatorial thin films (CTFs) offer the ability to densely map continuous ranges of compositions from multicomponent systems onto a single substrate [168]. However, since geometrically the compositions covering the CTF are a 2D projection of a surface in the multicomponent composition space, accessing specific independent multi-component compositions typically would require synthesizing multiple thin films. Additionally, while the CTFs can contain a vast number of compositions on a single film, a given composition is only available at over a small region and the films themselves are subject to degradation if annealed at elevated temperatures for prolonged periods of time (e.g. peeling, evaporation of volatile species). In situ alloying via additive manufacturing AM is comparatively slower at producing different compositions than CTF synthesis, however, specific compositions can be printed on-demand and the material printed can be produced in arbitrarily large sizes which enables high-temperature and long-duration annealing without substantial material degradation. Additionally, in the event that oxidation or loss of volatile species occurs during heat treatment, samples produced via AM are large enough to be mechanically polished to remove any reaction layer or scale.

In an effort to populate the Cr-Fe-Mn-Ni composition space with a rich collection of experimental thermodynamic data, this work employs both CTF synthesis and in situ alloying via AM to produce hundreds of unique Cr-Fe-Mn-Ni compositions which were then subjected to different isothermal aging heat treatments. As part of this high-throughput aging study, a CTF was used to span the center of the Cr-Fe-Mn-Ni composition space with excellent composition resolution while multiple AM sample arrays were used to produce discrete compositions across the entire composition space. Playing to the strengths of each of these synthesis techniques, the Cr-Fe-Mn-Ni CTF was used for low-temperature, short-duration aging experiments while the AM sample arrays were used for high-temperature, long-duration aging experiments.

To compliment the rapidity of these high-throughput synthesis techniques, similarly accelerated techniques were used to characterize the materials before and after aging, including synchrotron X-ray diffraction (XRD) of the aged combinatorial thin film and automated SEM, EDS, and lab-scale XRD of the aged additively manufactured compositional arrays. Experimental thermodynamic data from both the CTF and the additively manufactured arrays including phase composition, phase fraction, and lattice parameters were added to the thermodynamic databases which are used to refine the chemical potentials used in CALPHAD simulation. CALPHAD simulation can then be used to map the remaining areas of the Cr-Fe-Mn-Ni compositional phase space.

3.2 Methods and Materials

Combinatorial thin-film (CTF) synthesis was performed at Ruhr-Universität, Bochum using via co-deposition, whereby sputter guns are positioned at non-perpendicular incident angles to a substrate which allows the relative deposition rate from a given sputter gun to be graded across the surface of the substrate. By adjusting the incident angle and the power of each sputter gun, a combinatorial thin film of relatively uniform thickness centered on a specific composition is achievable. In this work, a CTF was deposited onto a 100-mm-wide Si wafer, passivated with an oxide thickness of ~1.5 μm to prevent interdiffusion, using elemental Cr, Fe, Mn, Ni sputter gun cathodes with purities >99.99%, a film ~1.25 μm in thickness was produced, shown in Figure 22. The composition at 342 points, in a grid pattern spanning the surface of the CTF, was measured using energy-dispersive spectroscopy (EDS). The CTF was aged for 4 hours at 500 °C in atmospheric pressure of UHP Ar while the surface of the film was covered by a blank passivated Si wafer to minimize the volatilization of Mn in the film. The CTF was allowed to cool in the furnace down (~10^{-1}-10^{0} K/s) to room temperature to avoid peeling of the film. After aging, each point on the CTF was examined using synchrotron X-ray diffraction (XRD) at the Stanford Linear Accelerator Center (SLAC), using a 16-keV X-ray beam, with a 0.15 μm^2 spot size, to produce a 2D diffraction pattern captured using a wide-angle X-ray scattering (WAXS) detector.

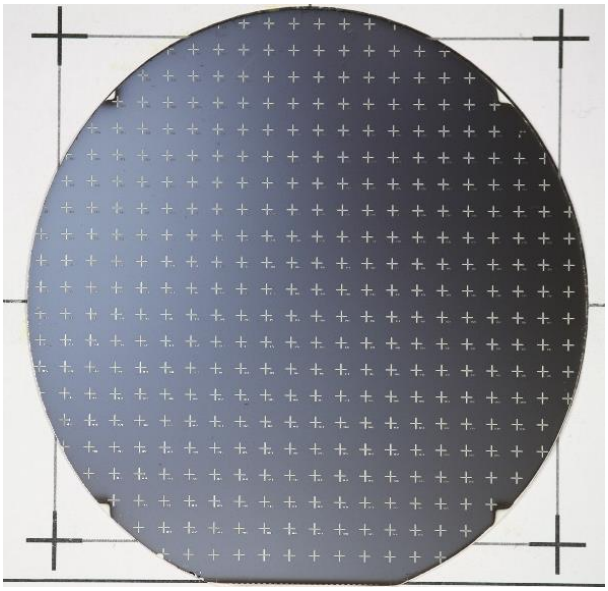

***Figure 22**: Patterned combinatorial thin film (CTF).*

Compositional arrays produced by in situ alloying via additive manufacturing (AM) containing >100 discrete alloy compositions were produced using an Optomec LENS MR-7, a directed energy deposition (DED) metal 3D printer equipped with four independently controlled powder hoppers. Each hopper was filled with either Cr, Fe, Mn, or Ni elemental powder. All powders were gas atomized and purchased from American Elements; Cr, Fe, and Ni powders had purities >99.9% while the Mn powder was >99 pure. Each hopper on the LENS MR-7 is outfitted with an auger, whose speed can be controlled remotely, which introduces the metal powder into a common Ar gas stream where powders from each hopper are mixed in flight to the printhead. The mixed powder is sprayed out a set of nozzles directed at a single point where they are intercepted by a continuous-wave IR laser, up to 1 kW in power, which melts the powders together and deposits material onto the build plate. By maneuvering the build plate with respect to the printhead, arbitrary geometries can be printed. Each AM array comprised 25 square stubs, 10 x 10 mm in area, built five print layers tall resulting in stub heights varying between ~3-5 mm tall, printed onto a single 316-stainless-steel build plate (100 x 100 x 6.35 mm), an example of which is shown in Figure 23. All laser and stage motion parameters were kept constant between prints. Each print layer consists of delivering the desired powder composition at a rate of ~0.2 mols/min (as calculated from mass flow rate

calibrations) to the printhead and consolidating the powders using a laser power of 350 W while rastering the stage at 10.58 mm/s, with a hatch spacing of 0.38 mm. After each print layer, two remelting passes were performed with a laser power of 500 W, at a speed of 21.17 mm/s, and a hatch spacing of 0.19 mm to ensure chemical homogeneity. The laser focus was set to be 0.38 mm below the build surface and the scan direction was rotated 90° between each layer – this pattern was repeated five times, moving in the build direction 1 mm and rotating the scan direction 90° between each set. Since the composition of parts produced by AM with elemental powders often deviates from the average composition of the powder delivered, due to ranges in elemental melting points, vapor pressures, and powder size distributions and geometries, a calibration compositional array consisting of 25 stubs of different compositions was printed, and the composition of each stub was measured via EDS using a JEOL JSM-6610 scanning electron microscope (SEM) at the Wisconsin Nanoscale Imaging and Analysis Center. From the calibration compositional array, the relationship between auger RPM and printed composition was determined by adding a retention rate term and fitting the coefficients relating mass flow rate to auger RPM; a more detailed description of composition calibration and the in situ alloying via AM process can be found in reference [167]. After printing, the compositional arrays were aged in a water-cooled ultra-high-vacuum (UHV) furnace at 1000 °C then 700 °C for 24 hours each, with rapid cooling (~10^0-10^1 K/s) and removal from furnace between treatments. After each heat treatment, the aged compositional arrays were mechanically polished, to remove any reaction layer of material which may have lost Mn to volatilization, and characterized using SEM, EDS, and lab-scale XRD using a Bruker D8 Discover.

XRD patterns acquired from both the CTF and the AM arrays were first matched to simulated XRD pattern standards using a series of Matlab scripts, to ease the indexing burden, after which each spectrum was manually verified to ensure proper peak identification. To minimize the time-consuming process of manual verification of each spectrum for future datasets, two aggregate data sets separately containing the synchrotron and lab-scale XRD data were input into an unsupervised hierarchical clustering machine learning algorithm to categorize the spectra.

***Figure 23**: Compositional array produced by in situ alloying via additive manufacturing (AM).* For reference, each square stub is 1 cm^2 while the build plate is 10 cm on a side.

Thermodynamic modeling using the CALPHAD method was performed using the PanDat software and the PanHEA database in collaboration with Computherm LLC. Specifically, the High-Throughput Calculation (HTC) function was used to simulate an array of composition spanning the entirety of the Cr-Fe-Mn-Ni composition space, with a step size of 5 at%. The specific details of CALPHAD modeling and use of the PanDat software and its application to the study of HEAs have been discussed extensively elsewhere [163]. The predicted phases at thermodynamic equilibrium were calculated for each composition at three different temperatures, 1000 °C, 700 °C, and 500 °C, corresponding to the AM homogenization temperature, the AM aging temperature, and the CTF aging temperature, respectively.

3.3 Results

3.3.1 Combinatorial Thin Film

Prior to deposition of combinatorial thin film, the composition at the center of the wafer was targeted to be $Cr_{18.2}Fe_{27.3}Mn_{27.3}Ni_{27.3}$, a Cr-Fe-Mn-Ni HEA composition often studied in literature [69, 169,

170], while the minimum concentration of each element anywhere on the film was targeted to be 10 at%. Following deposition of the Cr-Fe-Mn-Ni combinatorial thin film, automated chemical mapping via EDS was performed across the entire wafer to determine the composition at each position. Figure 24 shows the EDS results of the CTF in the as-deposited composition. Here, smooth chemical gradients can be seen for each of the four constituent elements spanning much of the HEA composition space, while the composition at the center of the wafer was measured to be $Cr_{19.6}Fe_{27.4}Mn_{26.8}Ni_{26.2}$.

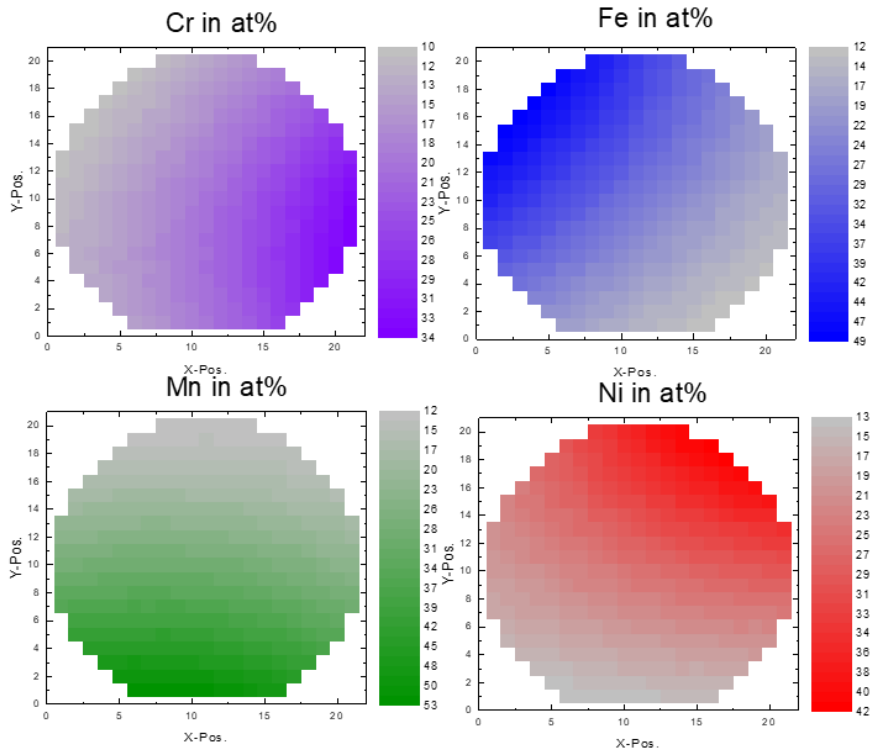

***Figure 24**: EDS chemical mapping of Cr-Fe-Mn-Ni CTF in the as-deposited condition.*

Thermally aging metallic CTFs poses several unique challenges over traditional “bulk” materials due to the geometric constraints of the material. Firstly, the act of heating the CTF can relieve residual stresses in the film retained from the deposition process which may lead to geometric changes. Secondly, differences in the coefficient of thermal expansion (CTE) between the varying compositions across the thin film, as well as from any mismatch between the CTE of the film and the SiO2/Si substrate, can cause

additional stresses during heating and cooling. Both of these effects can lead to delamination of the film from the substrate which can compromise the ability to perform experiments on the film. Additionally, due to the limited amount of material the film is comprised of, oxidation and volatilization of species from the CTF pose as serious threats – especially since no mechanical sample preparation can performed on the film to remove any reaction layer as can be done with bulk materials.

To minimize the loss of CTF components (namely Mn) to volatilization and to limit oxidation, the CTF was thermally aged at atmospheric pressure in ultra-high purity argon at 500 °C for 4 hours, followed by furnace cooling to minimize the risk of delamination. SEM imaging and EDS mapping was performed at 256 locations on the CTF after thermal aging to assess any chemical changes (i.e., oxidation, volatilization) or morphological changes. Figure 25 shows representative SEM imaging and EDS chemical mapping of the thermally aged CTF, taken from the center of the wafer near the $Cr_{19.6}Fe_{27.4}Mn_{26.8}Ni_{26.2}$ composition. From the SEM imaging, an extensive network of microcracks is observed which was found to span the entirety of the CTF surface, with no discernable dependance on the local composition. The composition at the center of the CTF after aging was measured to be $Cr_{18.6}Fe_{26.8}Mn_{28.5}Ni_{25.1}$ with an oxygen content of 0.36 at%, indicating no substantial volatilization of Mn and minimal oxidation during the thermal aging treatment. Indeed, across the entire wafer, compositions after thermal aging were typically within ±3 at% of their measured composition before aging. While oxygen is generally difficult to quantify with confidence using EDS, across the wafer the oxygen concentration was measured to be between 0-6 at%, except for compositions above ~40 at% Mn in which oxygen measurements ranged between 4-12 at% suggesting preferential, albeit minimal, oxidation with increasing Mn content.

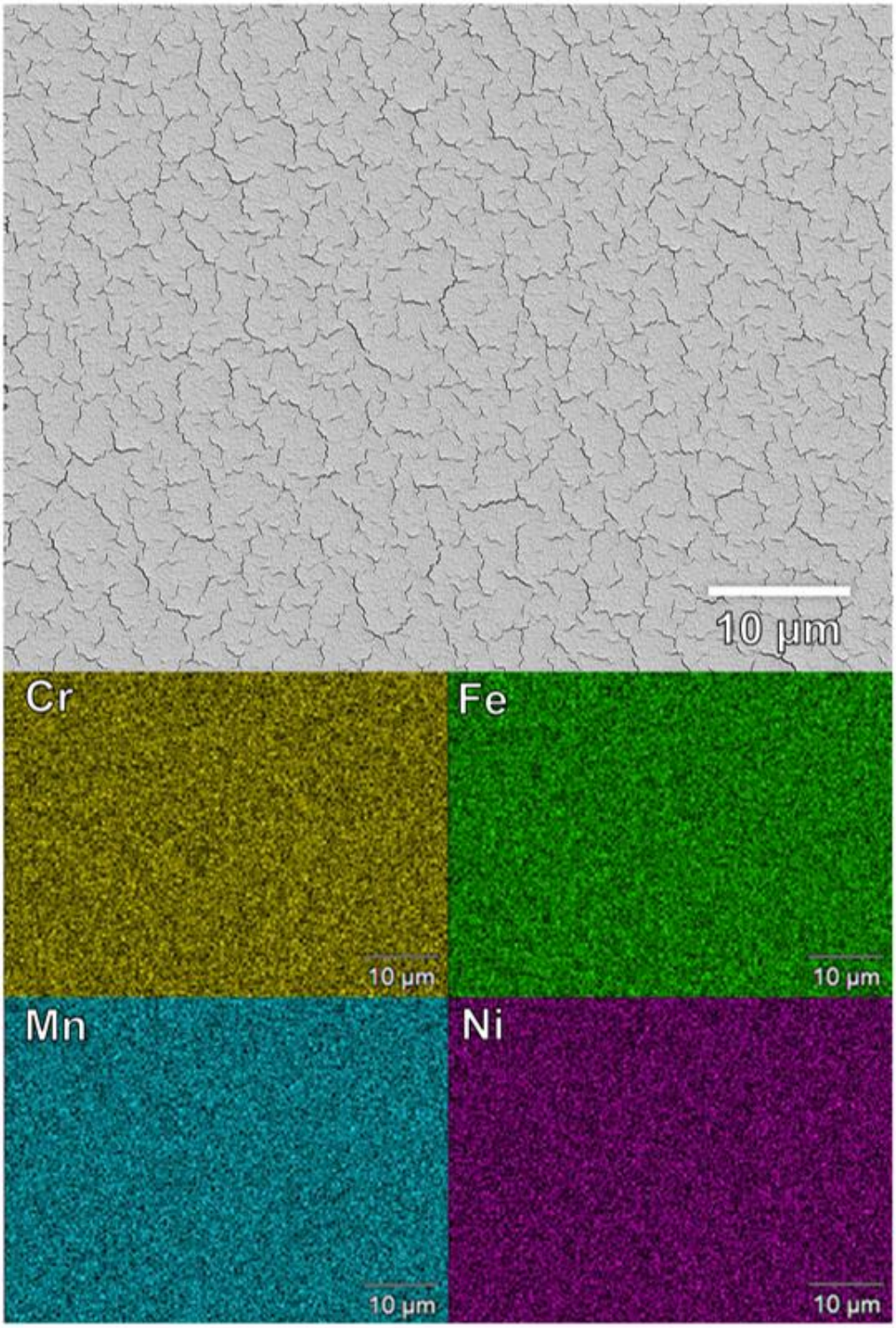

Figure 25*: SEM secondary-electron image and EDS chemical mapping of the thermally aged CTF taken from the center of the wafer near the* $Cr_{18.2}Fe_{27.3}Mn_{27.3}Ni_{27.3}$ *composition.*

342 unique compositions spanning the entire Cr-Fe-Mn-Ni CTF wafer were characterized after thermal aging using synchrotron XRD in transmission. To aid in the indexing of this extensive dataset, a suite of Matlab programs was developed to compare the experimental XRD spectra with simulated XRD spectra for each of the anticipated phases near the center of the Cr-Fe-Mn-Ni composition space (e.g., FCC, BCC, sigma, etc.). After the automated indexing, each of the experimental XRD spectra was manually compared to the automated indexing outputs for quality control. The entire synchrotron XRD dataset from the aged Cr-Fe-Mn-Ni CTF is presented in Figure 26a and Figure 26b, while an example of an indexed diffraction pattern is shown in Figure 26c, which was taken from scan 196 near the center of the wafer near the composition $Cr_{18.2}Fe_{27.3}Mn_{27.3}Ni_{27.3}$. Due to the low crystallographic symmetry of the sigma (σ) phase, which leads to a wide array of reflections in the diffraction pattern, the presence of σ phase can complicate the indexing process as many of the intensity peaks produced by the σ phase overlap with those produced by the FCC and BCC phases. To manually confirm the presence of each phase from the diffraction patterns, signature peaks with minimal peak overlap were identified for each phase, namely the [220]-type reflection near 4.9 $Å^{-1}$ for the FCC phase and the [200]-type reflection near 4.4 $Å^{-1}$ for the BCC phase, while a series of small peaks clustered near 3 $Å^{-1}$ and 5 $Å^{-1}$ were indicative of σ phase – which can be observed in Figure 26b for scans 1 through ~200.

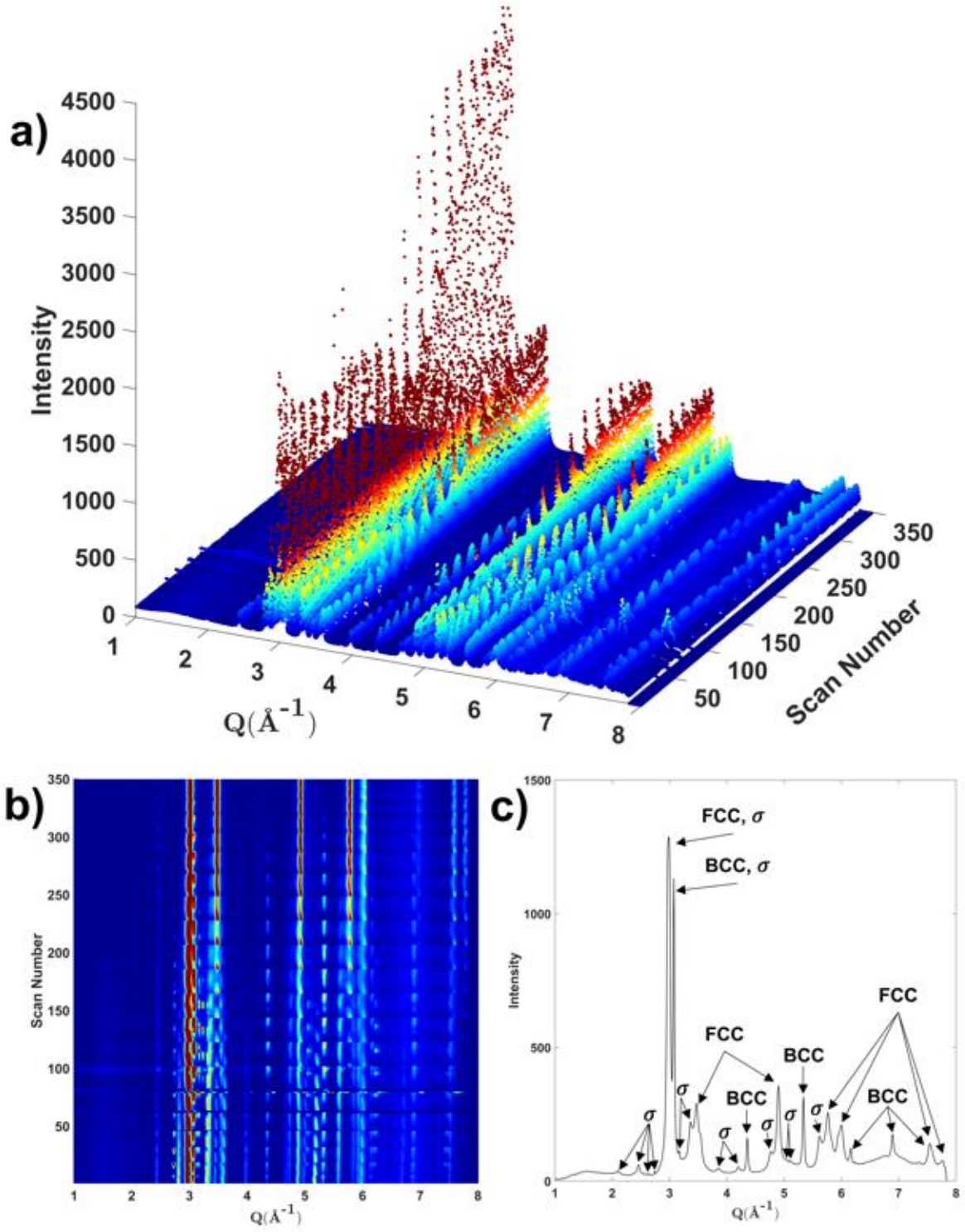

***Figure 26**: a) 3D visualization and b) intensity colormap of synchrotron XRD data from the aged CTF. c) example of indexed XRD diffraction pattern showing the FCC, BCC, and sigma phases collected from scan 196 near the center of the wafer with the composition* $Cr_{18.6}Fe_{26.8}Mn_{28.5}Ni_{25.1}$.

From the synchrotron XRD, the phase makeup of each composition on the CTF was determined and is presented in Figure 27. Here, the smoothly graded compositions of the combinatorial thin film are shown to form a curved 2D surface through the four-element composition space. Compositions in the Ni-rich region of the CTF remained as a single FCC phase after aging at 500 °C, while increases in Fe or Cr promote the formation of a BCC phase. Increases in Mn and Cr (at the cost of Ni and Fe) promote the formation of a CrFe-type σ phase in addition to the FCC and BCC phases which together form a three-phase region covers most of the wafer. Other notable regions include an FCC+σ region near the Fe+Mn side of the wafer, as well as a BCC+σ region near the edge of the wafer with the greatest Cr content. In addition to these regions, several XRD spectra near the Cr-rich edge of the wafer were unable to be indexed due to visible delamination and degradation of the metallic film locally, however, these points are an exception as the vast majority of the CTF remained visually pristine following aging. Collectively, the indexing of XRD spectra from the smoothly varying compositions of the CTF enables precise mapping of the phase boundaries within the Cr-Fe-Mn-Ni system, with a resolution that few experimental techniques rival.

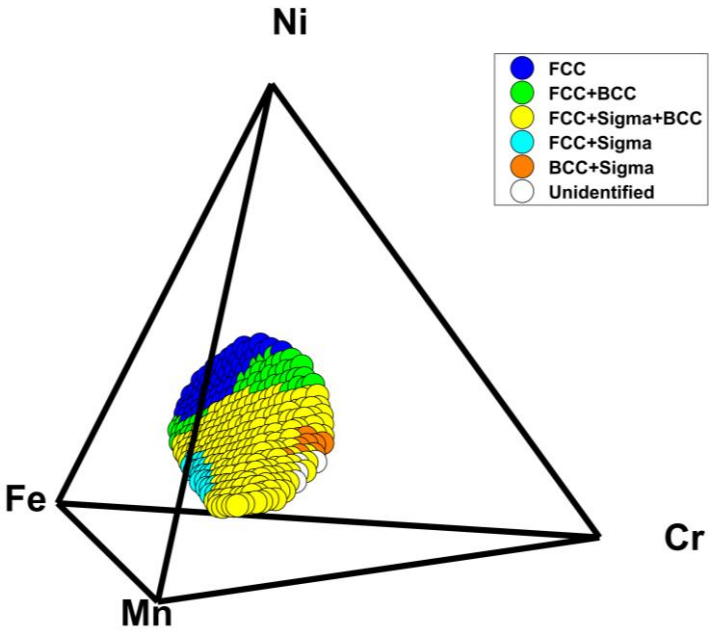

***Figure 27**: Phases measured using an automated Matlab code to process the SLAC data of the CTF after aging at 500 °C for 4 hours. Outliers have been spot checked by human to ensure quality.*

3.3.2 Additively Manufactured Arrays

As compared to the combinatorial-thin-film synthesis, in situ alloying using additive manufacturing can produce samples which are many orders of magnitude larger in size (millimeters versus microns) enabling more aggressive thermal treatments and mechanical sample preparation. For this study, 120 Cr-Fe-Mn-Ni alloys across five additively manufactured arrays were subjected to a two-part thermal treatment consisting of a 24-hour homogenization at 1000 °C followed by a 24-hour age at 700 °C, with SEM, EDS, and benchtop XRD performed once after each step. Following the printing process, macroscopic chemical compositions of each additively manufactured sample were determined by performing XRF measurements, which can measure the composition of a single sample in approximately 30 seconds. However, to assess the microscopic chemical homogeneity and presence of entrapped elemental powders from the printing process, SEM and EDS was performed on each sample in the as-printed condition. For comparison, the microstructures and chemical mapping of the $Cr_{35}Fe_{15}Mn_{15}Ni_{35}$ in the as-printed condition and after the two-step heat treatment are shown in Figure 28a and Figure 28b, respectively. In the as-printed condition, the $Cr_{35}Fe_{15}Mn_{15}Ni_{35}$ sample appears composed of a single chemically homogeneous phase without any notable amount of unmelted powder entrapped. The microstructure consists of grains, ~50-100 micrometers in size, that are irregularly shaped, which is indicative of the high cooling rates involved during DED synthesis, estimated to be on the order of 10^4 -10^5 K/s [171]. After the 24 hours at 1000 °C followed by 24 hours at 700 °C, the microstructure has decomposed into a Ni-rich phase and a Cr-rich phase, which are expected to be FCC and BCC, respectively.

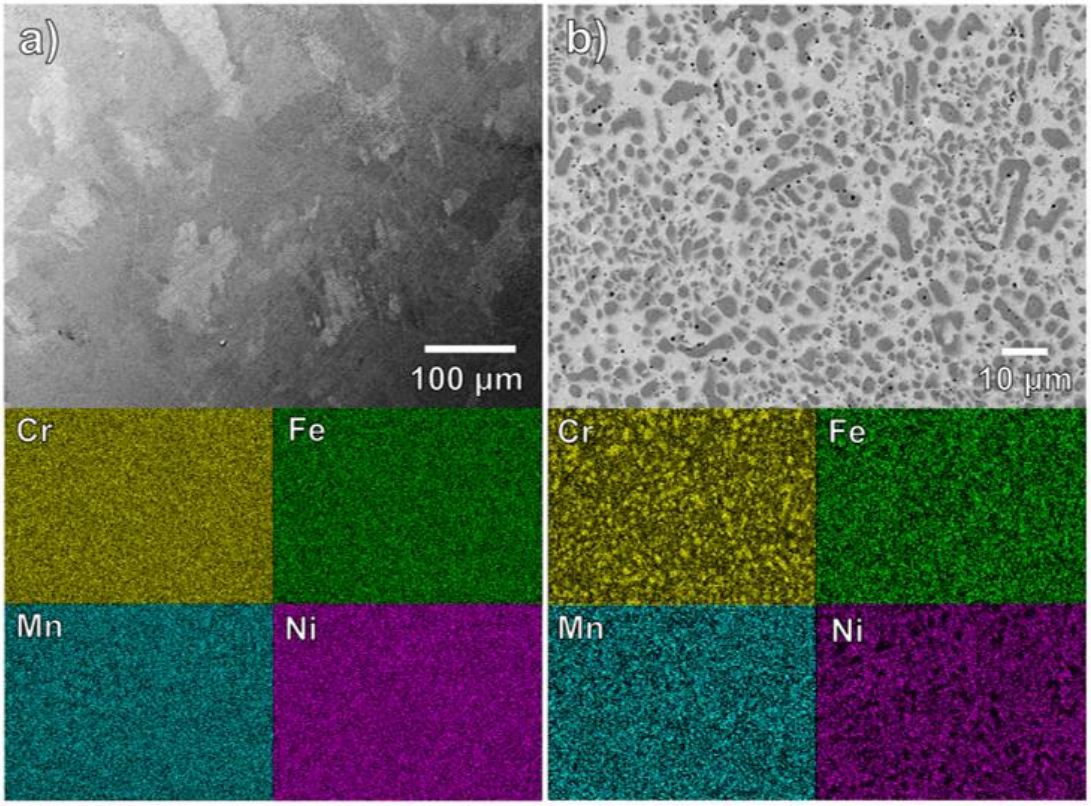

***Figure 28**: Example of the a) as-printed versus b) homogenized+aged microstructure of $Cr_{35}Fe_{15}Mn_{15}Ni_{35}$ from an additively manufactured sample array. Note: the magnification is 5x greater in the homogenized+aged image to highlight the Cr-rich precipitates.*

Due to the size of the XRD dataset, totaling 240 spectra between the two heat treatment temperatures, the same automated indexing regime with manual quality controlled was employed as was used for the combinatorial thin film in section 3.3.1. The experimentally measured phases after the 1000 °C homogenization treatment and subsequent 700 °C aging treatment are shown in Figure 29 and Figure 30, respectively.

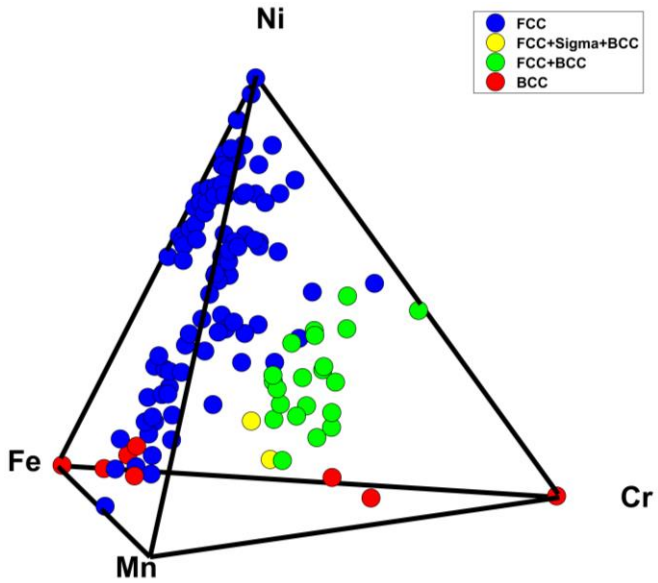

***Figure 29**: Phases of 120 additively manufactured Cr-Fe-Mn-Ni alloys after a 24-hour homogenization heat treatment at 1000 °C, measured experimentally via XRD.*

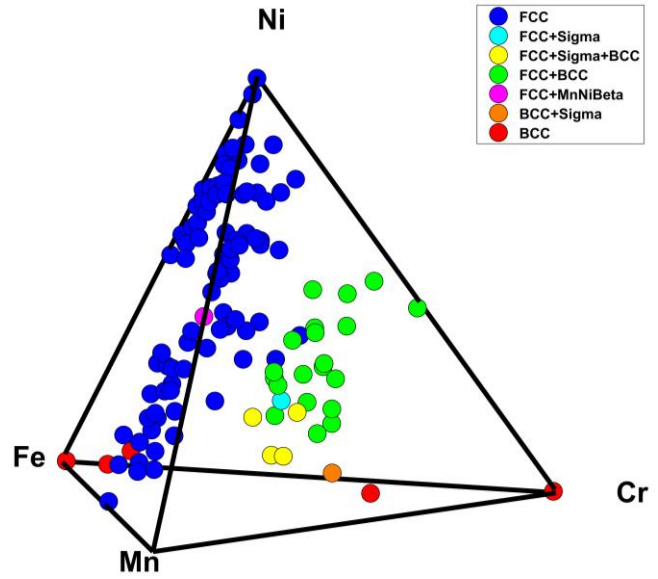

***Figure 30**: Phases of 120 additively manufactured Cr-Fe-Mn-Ni alloys after a 24-hour homogenization heat treatment at 1000 °C plus a 24-hour aging heat treatment at 700 °C, measured experimentally via XRD.*

After the 1000-°C heat treatment, the additive samples can be grouped into three major categories: a large single-phase FCC region spanning the Fe- and Ni-rich areas of the composition space, a two-phase FCC+BCC region with increasing Cr content, and narrow range of single-phase BCC compositions lacking in substantial Ni content. Two of the AM samples were identified to contain some fraction of σ phase. The

compositions of both σ-containing alloys had Cr:Fe ratios near 1:1, which is the near the prototypical Cr:Fe characteristic of the σ phase from the Cr-Fe binary phase diagram [172]. While in the binary Cr-Fe system, σ phase does not form above ~830 °C, experimental work with HEAs in the Co-Cr-Fe-Mn-Ni system has demonstrated σ formation at temperatures in excess of 1000 °C from heat treatment durations as short as 3 minutes [173]. Such results increase the plausibility that the σ phase observed in the Cr-Fe-Mn-Ni alloys in the current study is indeed stable at 1000 °C, rather than resulting from the non-instantaneous cooling rate ending the 1000-°C heat treatment. However, evidence of the finite cooling rate following heat treatments in this study, on the order of ~10^0-10^1 K/s, is visible in the case of pure Fe, which would require cooling rates on the order of ~10^3-10^4 K/s to retain a measurable fraction of the FCC austenite phase below the 911-°C transition to BCC ferrite [174].

Following the 1000-°C homogenization heat treatment, the same 120 AM samples were aged for 24 hours at 700 °C and recharacterized. The phase distributions of the AM alloys after the aging heat treatment, shown in Figure 30, closely resemble the results after the homogenization treatment at 1000 °C, shown in Figure 29, with a few notable exceptions. Firstly, after aging, several alloys with reduced Ni content show formation of σ phase, expanding the FCC+BCC+σ three-phase region. Additionally, two of the previously single-phase FCC alloys with some of the highest Cr contents, $Cr_{42.1}Fe_{2.7}Mn_{4.0}Ni_{51.2}$ and $Cr_{40.4}Fe_{25.7}Mn_{4.9}Ni_{29.1}$, become FCC+BCC after aging indicating a decrease in the solubility of Cr in the FCC phase at 700 °C versus 1000 °C. While there is clear movement in the phase boundaries surrounding the FCC+BCC+σ three-phase region and between the FCC and FCC+BCC regions, the coarseness of the compositional mapping the AM arrays provide limits the precision with which these boundaries can be located relative to the CTF.

3.3.3 Comparison with CALPHAD Modeling

While advances in experimental synthesis and characterization techniques have improved the rate at which thermodynamic data can be collected, the speed of such experimental work is incapable of surpassing the speed of CALPHAD modeling – in part due to the times required to allow systems to

approach thermodynamic equilibrium. However, the accuracy of CALPHAD modeling is reliant on the availability and the accuracy of extensive experimental datasets. To assess the accuracy of using CALPHAD modeling to predict the stable phases of Cr-Fe-Mn-Ni HEAs and concentrated alloys, the experimentally determined phases of the 342 CTF compositions from section 3.3.1 and 120 AM alloy compositions from section 3.3.2 were compared to phases predicted by CALPHAD using the PanHEA thermodynamic database. Figure 31 shows the experimentally determined phases of the CTF compositions after aging at 500 °C and of the AM compositions after the homogenization heat treatment at 1000 °C and subsequent aging heat treatment at 700 °C, plotted against the equilibrium phase fields predicted by CALPHAD.

At 1000 °C, the equilibrium phase field predicted by CALPHAD is dominated by three major regions, namely FCC, BCC, and FCC+BCC. In addition to these major regions, alloy compositions with minimal Ni content begin forming σ phases and alloys which are Mn-based consist of combinations the A13 β-Mn phase and the other phases in the composition space. The experimentally measured phases closely follow the CALPHAD predictions, exemplified by the population of data straddling the FCC/FCC+BCC phase boundary. Overall, the CALPHAD predictions at 1000 °C are in good agreement with the experimental data, with CALPHAD predicting the phases measured experimentally correctly 88.3% of the time. Moreover, the majority of compositions which are in disagreement are Fe-rich alloys which were predicted to be FCC at 1000 °C but measured to be BCC. As described in section 3.3.2, this is likely the result of experimental limitations due to the cooling rate of samples during heat treatment meaning the accuracy of CALPHAD predictions at 1000 °C is likely well over 90%.

At 700 °C, the equilibrium phase field increases in complexity, with the additions of the A12 α-Mn, B2 ordered BCC, MnNi tetragonal, and Cr_3Mn_5 phases. Additionally, the portion of the composition space occupied by alloys containing σ phase greatly increases. While the FCC+σ and FCC+BCC+σ regions of the equilibrium phase field cover a large range of compositions, these regions

occupy compositions with elevated Mn contents which were not sampled as often by the AM arrays. Comparable to 1000 °C, the experimentally observed phases closely follow the CALPHAD predictions, with CALPHAD predicting the phases measured experimentally correctly 87.5% of the time. The CALPHAD modeling also accurately captures the movement of the FCC/FCC+BCC phase boundary between 1000 °C and 700 °C and indicates the new location of the boundary exists near a gap in the experimental data, illustrating the utility of using CALPHAD over experimental techniques alone.

At 500 °C, while no new phases are predicted, the equilibrium phase field is subdivided into additional combinations of the phases predicted and observed at higher temperatures. In Figure 31, the compositions of the CTF, with greater Mn contents than the AM arrays, can be seen crossing into the FCC+σ and FCC+BCC+σ regions of the equilibrium phase field, in addition to the FCC and FCC+BCC regions thoroughly sampled by the AM arrays. However, in contrast to the AM arrays, the CALPHAD predictions for the aged CTF are far less accurate, with CALPHAD predicting the phases measured experimentally correctly only 27.2% of the time. While many of the compositions on the CTF were indeed experimentally measured to have FCC+σ and FCC+BCC+σ phase makeups, many more of the compositions on the CTF were found to have all three FCC+BCC+σ phases than predicted by CALPHAD. The two most likely reasons for this are the duration of the CTF aging heat treatment, and the reliability of CALPHAD predictions at low temperatures. For the sake of the chemical and structural integrity of the CTF, the dwell time at 500 °C was limited to 4 hours which limits the amount of long-range diffusion that can occur which may be necessary for some compositions on the film to reach thermodynamic equilibrium. Additionally, the thermodynamic databases which are used in CALPHAD modeling are often based upon limited experimental data from elevated temperatures, which leads to greater uncertainty in the predictions when extrapolating to lower temperatures [175].

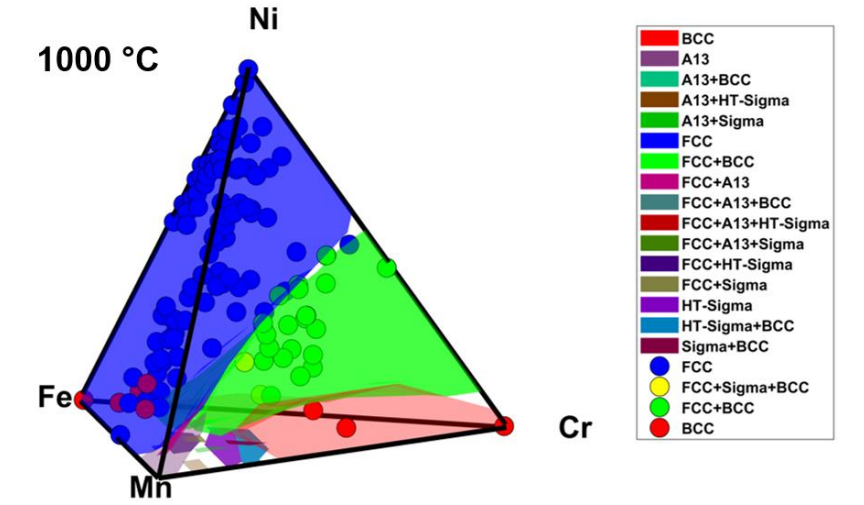
Ni
1000 °C
Fe
Mn
Cr
BCC
A13
A13+BCC
A13+HT-Sigma
A13+Sigma
FCC
FCC+BCC
FCC+A13
FCC+A13+BCC
FCC+A13+HT-Sigma
FCC+A13+Sigma
FCC+HT-Sigma
FCC+Sigma
HT-Sigma
HT-Sigma+BCC
Sigma+BCC
FCC
FCC+Sigma+BCC
FCC+BCC
BCC

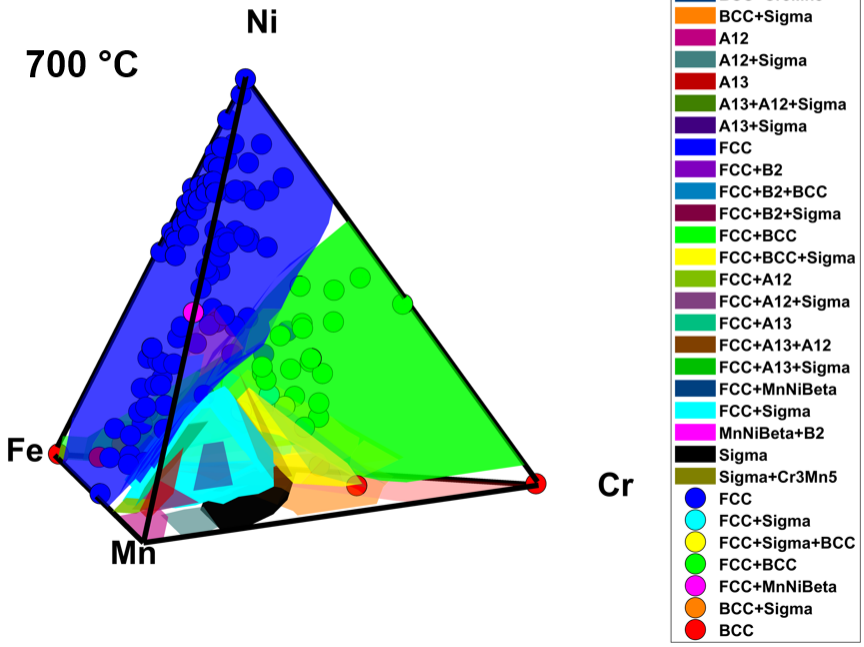
Ni
700 °C
Fe
Mn
Cr
B2
B2+BCC
B2+BCC+Sigma
B2+Sigma
BCC
BCC+Cr3Mn5
BCC+Sigma
A12
A12+Sigma
A13
A13+A12+Sigma
A13+Sigma
FCC
FCC+B2
FCC+B2+BCC
FCC+B2+Sigma
FCC+BCC
FCC+BCC+Sigma
FCC+A12
FCC+A12+Sigma
FCC+A13
FCC+A13+A12
FCC+A13+Sigma
FCC+MnNiBeta
FCC+Sigma
MnNiBeta+B2
Sigma
Sigma+Cr3Mn5
FCC
FCC+Sigma
FCC+Sigma+BCC
FCC+BCC
FCC+MnNiBeta
BCC+Sigma
BCC

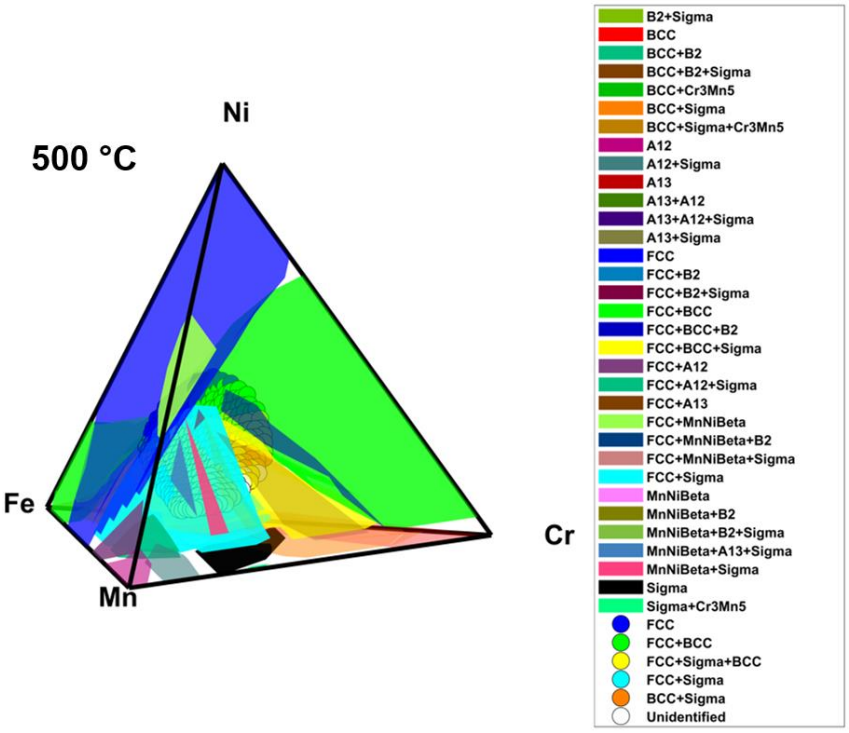

***Figure 31**: Phase diagram of Cr-Fe-Mn-Ni at 1000 °C, 700 °C, 500 °C as predicted by CALPHAD with overlays of experimental XRD.*

3.4 Discussion

When comparing the agreement of CALPHAD predictions with the AM compositional arrays heat treated at 1000 °C and 700 °C (88.3% and 87.5%, respectively) versus the agreement with the CTF aged at 500 °C (27.2%), at first glance it may appear as though the discrepancy is due solely to the relatively short dwell time of 4 hours and relatively slow cooling rate (~10^{-1}-10^{0} K/s) of the CTF. However, upon closer inspection of the phases measured across the CTF, it is clear that these discrepancies are not exclusively due to the thermal treatment. To illustrate this, Figure 32 shows the equilibrium phases of the CTF at 500 °C as predicted by CALPHAD. In comparison to the experimentally measured phases in Figure 27, CALPHAD modeling predicts a substantially smaller single-phase FCC region and three-phase FCC+BCC+σ region. As compared to CALPHAD predictions, a substantially larger portion of the CTF was measured to be single-phase FCC which may be expected if the duration and temperature of the aging heat treatment did not provide sufficient time kinetically for secondary phases, which require long-range

diffusion, to form. However, at the same time, σ phase was measured experimentally at many compositions on the CTF, namely Cr-rich compositions, which CALPHAD does not predict to exhibit σ phase at 500 °C or any temperature above there. Assuming the CALPHAD predictions are correct, this would imply that σ phase forms in these alloys at temperatures below 500 °C during the cooling from the aging treatment. Barring drastic differences in diffusion coefficients between alloy compositions on the CTF, the existence of a larger single-phase FCC region and larger three-phase FCC+BCC+σ region measured experimentally from the CTF conflict with each other from a kinetics standpoint. While under certain circumstance, thin films may contain phases which are stabilized by the strain and associated pressure exerted locally. However, this phenomenon requires a coherent or semi-coherent interface between the thin film and the substrate, and even then, would only be expected in the first tens of monolayers of the film [176-178]. Since the CTF in this study has a thickness greater than 1 micrometer and shows signs of substantial stress relief during aging, evidenced by the microcracking seen in Figure 25, it is improbable that strain-stabilization is contributing to phases measured experimentally. Thus, the discrepancies in experimentally measured phases and phases predicted by CALPHAD likely have contributions from the short aging duration, as well as increased uncertainty in CALPHAD predictions for concentrated alloy compositions at lower temperatures.

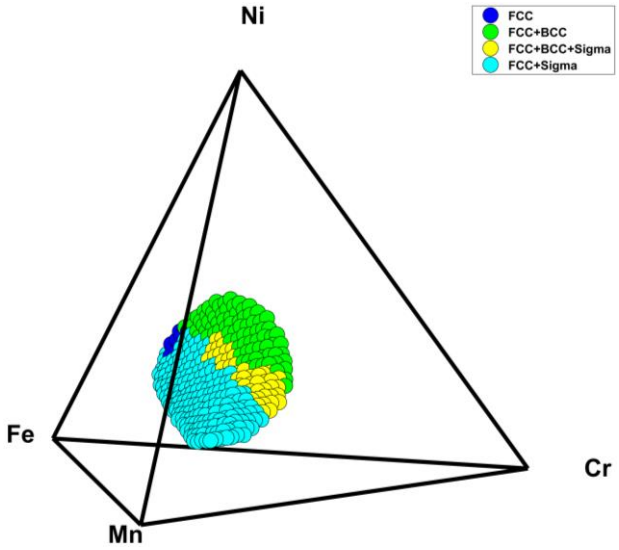

***Figure 32**: Equilibrium phases of CTF composition at 500 °C as predicted by CALPHAD.*

While combinatorial thin films have previously been used to assess the phase stability of hundreds of alloy compositions and validate CALPHAD modeling in a high-throughput manner, to the best of the authors' knowledge, the present study represents the first time in situ alloying via additive manufacturing has been deployed on a comparable scale. In total, 120 unique alloy compositions were examined at both 1000 °C and 700 °C using the same arrays of samples, which could presumably be used for future studies at different temperatures as well, thanks to "bulk" nature of the samples which allows them to be mechanically polished to remove any reaction layer resulting from either oxidation or volatilization during previous heat treatments. Moreover, the phases measured from the aged AM compositional arrays proved to be excellent agreement with CALPHAD predictions at both 1000 °C and 700 °C 88.3% and 87.5%, respectively). In addition to longer heat treatment durations for the AM arrays, the agreement between the experimentally measured phases and the CALPHAD predictions also benefit from the vast amount of data that has been generated surrounding the Cr-Fe-Mn-Ni from more than a century of steelmaking, which has been used to refine the thermodynamic databases used for CALPHAD modeling. Comparison of the experimental phase data generated from the AM compositional arrays to the data-rich Cr-Fe-Mn-Ni CALPHAD predictions then serves two purposes: 1) populate less-explored regions of the Cr-Fe-Mn-Ni composition space with experimental data (e.g., examining the equimolar and other HEA compositions), and 2) validate the use of AM compositional arrays in a high-throughput aging methodology using a well-studied system – both of which have been achieved.

While validation of thermodynamic databases using familiar combinations of elements is valuable in and of itself, the use of CTFs and AM compositional arrays provides an opportunity to explore and generate data for more exotic alloy compositions that would otherwise be too costly or time consuming to pursue. For example, in this study and after the required equipment is calibrated, the time to synthesize the CTF with 342 unique compositions and the time to additively manufacture discrete coupons of 120 unique alloy compositions were each less than one day – many times faster than conventional metallurgy techniques. Moreover, both the CTF and the AM compositional arrays are naturally suited for further high-throughput

processing and characterization owing to their form factors consisting of many alloy compositions on a single substrate, which typically can be analyzed more quickly and easily than the same number of individual samples. Using SEM/EDS as an example, a single CTF (342 alloys) or single AM compositional array (25 alloys) can be examined by only breaking vacuum to load the substrate once. If 10 minutes is taken as an estimate for the time to evacuate the SEM after loading a sample, examining the equivalent number of samples individually for a CTF would require nearly two and a half days of pumping and the equivalent number of samples individually for an AM array would require over four hours of pumping. Similar thought experiments can be performed for sample preparation and other characterization techniques, thus illustrating the potential of implementing high-throughput techniques.

In exploring new compositional spaces, CTFs, AM compositional arrays, and CALPHAD modeling each provide unique capabilities while serving complimentary roles. However, the utility of each technique varies depending on the compositions and temperatures being examined as well as the properties being measured. For example, in the present study, Cr-Fe-Mn-Ni alloys produced by additive manufacturing were able to be heat treated for long durations reliably and CALPHAD predictions were in good agreement with the phases measured experimentally. However, the CTF showed signs of deterioration after a shorter heat treatment, thereby decreasing the likelihood that all of the compositions were able to reach thermodynamic equilibrium at the aging temperature (500 °C). At the same, in situ alloying via additive manufacturing can have difficulties producing samples with disparate melting points and thermal properties, and if such a combination of elements does not already have a rich thermodynamic database to base CALPHAD modeling on, the use of CTFs may be the only viable high-throughput technique for effectively exploring said composition space.

Beyond CTFs and AM compositional arrays, several other high-throughput synthesis techniques have been used in different areas of the materials community. Similar to the CTF used in this study, many of these techniques achieve large ranges of alloy composition by employing compositional gradients, including diffusion multiples [102], grading via additive manufacturing [179], and grading via friction stir

welding [165]. However, each of these techniques involving compositional grading suffers from only containing a given composition a single point, 1D path, or at most a 2D cross section, but never in an arbitrary 3D volume, which typically limits the characterization techniques compatible with such graded materials to the micro- or nano-scale. By contrast, techniques similar to the synthesis of compositional arrays by additive manufacturing, including rapid alloy prototyping (RAP) [108] and advanced spark-plasma sintering (SPS) techniques [180], are capable of producing 3D volumes of discrete compositions, however, are often not as fast as gradient techniques when tasked with producing large arrays of compositions. In the aim to accelerate materials research and alloy development, it is thus desirable to holistically consider many high-throughput techniques, including combinatorial thin-film synthesis, in situ alloying via additive manufacturing, and CALPHAD modeling, when approaching a new experiment, rather than relying on one technique in a vacuum. Moreover, to take full advantage of efficiency gains from implementing high-throughput capabilities, it is often necessary to parallelize or increase the throughput of downstream experimentation and characterization techniques – else the implementation of the high-throughput techniques only pushes the workflow bottleneck forward rather than eliminate it entirely. By invoking high-throughput synthesis techniques (CTFs, AM compositional arrays), parallel processing (mechanical polishing of entire AM compositional arrays and heat treatment of the CTF and AM arrays), rapid characterization techniques (XRF, automated SEM/EDS, synchrotron XRD), and computationally efficient modeling and simulation (CALPHAD), the current study illustrates the time-savings and effectiveness of integrating multiple high-throughput techniques into an experimental design, and may serve as a framework for future high-throughput methodologies.

3.5 Conclusions and Future Work

In this work, the exploration and determination of equilibrium phases of the Cr-Fe-Mn-Ni composition space, with an emphasis on concentrated compositions including many high-entropy alloys, has been demonstrated and greatly accelerated by applying a series of high-throughput techniques in concert. Specifically, by using both combinatorial thin-film (CTF) synthesis and in situ alloying via additive

manufacturing (AM), a total of 442 unique alloy compositions were produced. Both the CTF and AM compositional arrays were successfully thermally aged, and the stable phases were subsequently examined using synchrotron X-ray diffraction (XRD) and lab-scale XRD for the CTF and AM compositional arrays, respectively. The XRD results from the CTF aged at 500 °C comprise a 2D surface with high compositional resolution through the center of the Cr-Fe-Mn-Ni composition space, while the series of AM compositional arrays homogenized at 1000 °C and subsequently aged at 700 °C provide data points which span a broader range of the composition space with a coarser compositional resolution. Results from both the CTF and the AM compositional arrays have been used to validate CALPHAD modeling over a broad range of both composition and temperature. At 1000 °C and 700 °C, CALPHAD predictions of equilibrium phases were in agreement with experimental data from the AM compositional arrays for 88.3% and 87.5% of the alloy compositions, respectively. At 500 °C, CALPHAD predictions were in agreement with experimental data from the CTF for only 27.2% of alloy compositions, with the greatest discrepancies originating from the size of the single-phase FCC region and three-phase FCC+BCC+σ region, likely resulting from a combination of insufficient aging time of the CTF and greater uncertainty of CALPHAD predictions for concentrated alloys at lower temperatures.

Most importantly, this work has demonstrated the viability of using AM compositional arrays for thermodynamic studies and more broadly provides a framework for integrating cross-disciplinary high-throughput techniques to accelerate materials research. Future work will include investigating less-studied alloy systems as well as expand the properties explored using high-throughput techniques beyond equilibrium phase stability to include oxidation resistance, irradiation tolerance, and susceptibility to molten salt corrosion.

4 Room-Temperature Ion Irradiation and Stage Development

This chapter features direct content from the following journal article(s) first-authored by the PhD candidate:

M. Moorehead, B. Queylat, H. Zhang, K. Kriewaldt, A. Couet, **Development of a versatile, high-temperature, high-throughput ion irradiation system**, Nuclear Inst. and Methods in Physics Research, A (2021), *in press*.

M. Moorehead, P. Nelaturu, M. Elbakhshwan, C. Parkin, C. Zhang, K. Sridharan, D.J. Thoma, A. Couet, **High-throughput ion irradiation of additively manufactured compositionally complex alloys**, Journal of Nuclear Materials, 547 (2021) 152782.

4.1 Introduction and Motivation

Understanding the thermodynamic stability of various HEAs and CCAs is an important step in exploring the concentrated composition space for viable alloys for advanced nuclear applications, however, the most crucial step is determining the performance of a material under irradiation. In a reactor environment, core structural materials are subjected to a flux of neutrons ranging in energy from their birth during fission (~2 MeV) down to thermal energy levels (~0.025 eV) over the span of years and even decades (e.g., in the case of the reactor vessel). To simulate end-of-life damage levels in a material while maintaining the highest fidelity, test reactors such as the Advanced Test Reactor can be used, however, damage rates here are still low (~10 dpa/year) compared to the damage levels which could be observed in many advanced reactor designs (~100-600 dpa) [181]. Given the duration of neutron irradiation experiments, notwithstanding other complicating factors, juxtaposed with the typical (desired) residence period of a PhD student, it is not uncommon to use ion irradiation to further accelerate irradiation studies.

Ion irradiation has long been used as a surrogate for neutron irradiation experiments which are comparatively slower, more expensive, and often can leave materials activated and difficult to handle post-

irradiation. Owing to the higher dpa rates associated with ion irradiation, researchers can subject materials to radiation damage levels equivalent to that of an end-of-life nuclear reactor after only a few hours of irradiation using heavy ions [182]. Similarly, using protons or helium ions, radiation-induced phenomena such as precipitate formation/dissolution [183, 184], irradiation-assisted stress corrosion cracking (IASCC) [185], and gas bubble formation [186, 187] can be induced comparable to their neutron-induced counterparts while still maintaining damage rates orders of magnitude greater than neutron irradiation.

Historically, in the process of evaluating new alloys for nuclear applications, ion irradiation has taken considerably less time than the alloy synthesis and post-irradiation examination. However, recent advances in combinatorial synthesis techniques, such as in situ alloying via AM [167] and combinatorial thin film synthesis [166], have helped accelerate the alloy synthesis process as well as enable more efficient characterization by allowing many samples and compositions to be examined in parallel on a single substrate. Concurrently, automated, high-throughput, characterization techniques, and associated data analysis, are being developed with recent significant advances in automation and/or autonomous characterization [188]. Unfortunately, most ion irradiation facilities are primarily equipped to accommodate small samples ($\lessapprox$1 cm^2), thus making them incompatible with the comparatively larger substrates (~100 cm^2) utilized for these high-throughput synthesis techniques. Even if large sample arrays were to be separated into individual samples to be irradiated one at a time, considerable time would be spent loading the sample, achieving adequate vacuum, heating the sample to the desired temperature, and finally allowing the sample to cool down after irradiation before it could be safely exchanged for the next sample. These practical challenges contribute to the already lengthy process of nuclear materials discovery and qualification, which historically has taken 20-30 years for new materials, and identification of this critical chokepoint has prompted the creation of both domestic and global initiatives to address it [189], including the aptly named Nuclear Materials Discovery and Qualification Initiative (NMDQi) [190] in the United States.

With the growing use of combinatorial synthesis methods and high-throughput, automated characterization techniques, ion irradiation facilities will need to upgrade their capabilities to be able to accommodate these new material platforms, lest ion irradiation become the new chokepoint in the alloy development process for nuclear applications. To address this need, the work herein first describes the design and development of a versatile, high-throughput ion irradiation stage at the University of Wisconsin-Madison Ion Beam Laboratory capable of irradiating large sample arrays (>175 cm^2 work area) of arbitrary geometries with remote-controlled operation. Then, to demonstrate the viability and utility of applying an AM-based HTP methodology to radiation-tolerant alloy development, an assortment of CCAs in the Cr-Fe-Mn-Ni alloy system is examined, including several HEAs which have previously shown promising ion and neutron irradiation tolerance [169, 170]. From the Cr-Fe-Mn-Ni system, targeted compositions of each pure element, every $X_{50}Y_{50}$ binary alloy, every $X_{33}Y_{33}Z_{33}$ ternary alloy, every $W_{18}X_{27}Y_{27}Z_{27}$ and $W_{15}X_{35}Y_{15}Z_{35}$ quaternary alloy, and the equimolar alloy, $Cr_{25}Fe_{25}Mn_{25}Ni_{25}$, have been examined.

4.2 Stage Design

The nuclear materials community is not the first to encounter the challenge of performing ion irradiations on large substrates. Other industries, such as the microelectronics industry in the case of ion implantation, have addressed this challenge by either rotating a carousel of substrates beneath an ion beam or by raster an ion beam across a single substrate [191]. To irradiate different regions of a substrate, it is common to electrostatically or magnetically deflect the incoming ion beam to direct it to the desired position. However, given the relatively high energies of ions used to simulate radiation damage in nuclear reactors (typically 1-5 MeV), deflecting the ion beam sharply would require the addition of powerful electrostatic deflectors or bending magnets while deflecting the beam more gradually would require lengthening and/or broadening a beamline – both of which would be financially and logistically burdensome. Instead, a sample stage system capable of maneuvering samples into the path of the beam appears more tractable. However, manipulating a stage requires the use of motors which can pose risks to maintain ultra-high vacuum conditions necessary for ion irradiation, due to the off-gassing of polymeric

components. The problem of off-gassing can be further exacerbated if components are heated while under vacuum as is typical of many irradiation experiments. Additionally, low melting materials such as zinc (in galvanized steel) and aluminum can be easily sputtered if they are impinged upon by the ion beam, which may lead to contamination of samples. Thus, it is desirable to keep all motors outside of the vacuum chamber and construct the stage out of materials capable of operating reliably at elevated temperatures and without fear of off-gassing or sputtering.

The University of Wisconsin-Madison Ion Beam Laboratory (IBL) facility was used to development and test various components of the high-throughput irradiation system described herein. The facility uses a 1.7-MV tandem accelerator and features two sources: a TORVIS source used to produce helium and hydrogen ions, to more closely simulate neutron damage in nuclear reactors (using damage rates of ~1E-6 dpa/s), and a SNICS source capable of producing a wide range of heavy ions (e.g., C, Si, V, Fe, Ni, Nd) used for producing much higher damage rates to simulate end-of-life damage levels in a nuclear reactor (using damage rates of ~1E-2 dpa/s). The UW-Madison IBL facility features three post-accelerator beamlines featuring different detectors and equipment to accommodate different ion irradiation experiments; the middle beamline in particular features a large cylindrical chamber (ID: 50 cm, height: 28 cm) which was used to house the high-throughput irradiation stage and equipment.

To ensure proper tolerances between moving parts, stage components were modeled using SolidWorks 2019 and machined using a CNC mill. To ensure safe and reliable operation at elevated temperatures, all major stage components inside the vacuum chamber were machined from 304 stainless steel. Figure 33 shows a 3D model of the stage system and its components, both in a blown-up and an assembled view, while Figure 34 shows an image of the stage loaded into the vacuum chamber. To achieve a broad range of motion in two dimensions, the stage slides onto a hanger and is retained using a dovetail mechanism, which prevents relative motion between the stage and the hanger in all directions except ±X (see Figure 33b for coordinate system). The hanger is suspended in the center of the vacuum chamber by the joining rod, which connects the hanger to a linear manipulator that allows for motion in ±Y. To move the stage along the X

axis, a hook is used to connect the stage to a second linear motion feedthrough perpendicular to the first. To maintain free motion of the stage along the Y axis, the hook connects to the stage using a T-slot, allowing the stage to move in the ±Y directions without applying a torque to the hook or the X-direction linear manipulator.

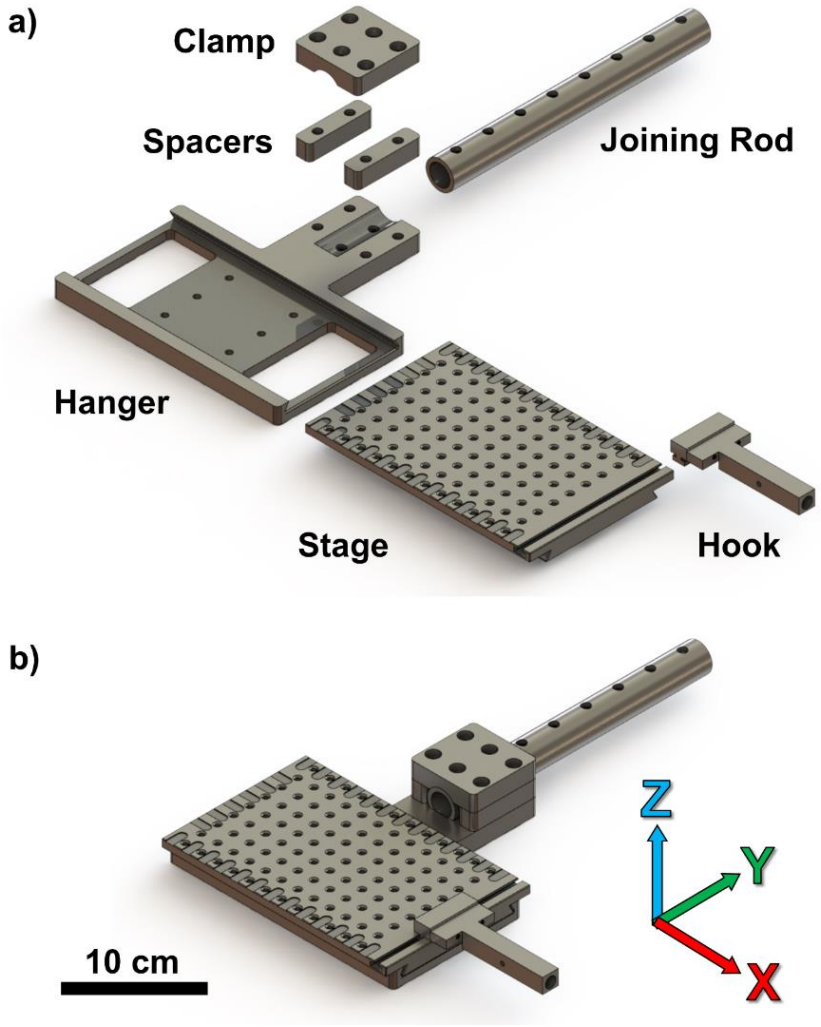

Figure 33*: 3D model of stage system in a) a blown-up view and b) an assembled view. Precision shoulder bolts have been omitted for clarity.*

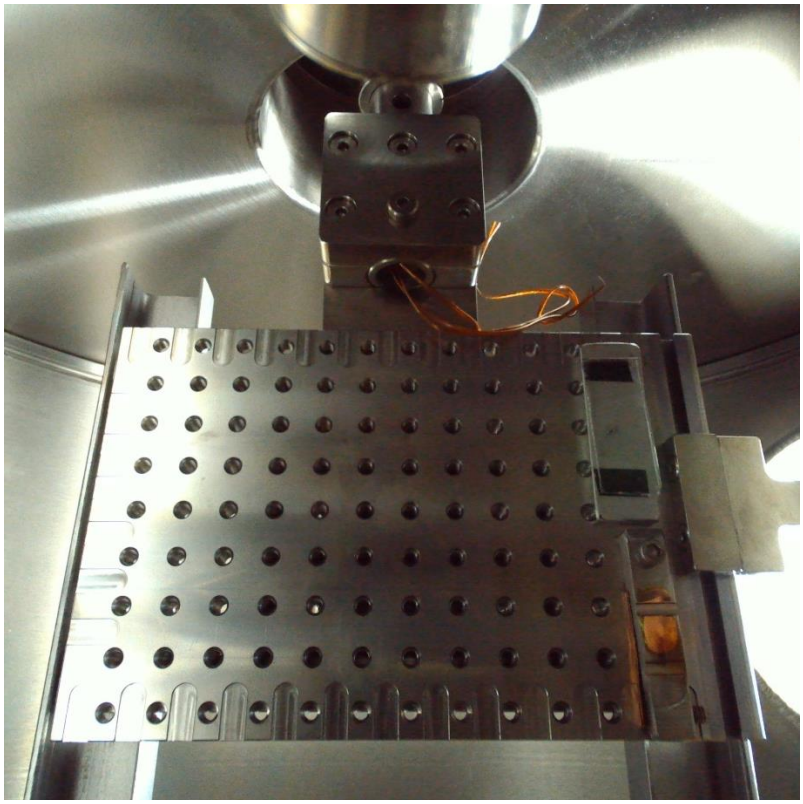

Figure 34*: Photograph of stage loaded into vacuum chamber. Thermocouple wires can be seen passing through the joining rod at the top of the hanger while a piece of quartz used for ion beam shaping.*

To drive the stage, one Nanotec AS4118 stepper motor is attached to each manipulator on the exterior of the vacuum chamber. Since the weight of the entire stage/hanger system is borne by the Y manipulator, a geared 50:1 torque multiplier is used to ensure the stepper motor along the Y axis can reliably move the stage/hanger without stalling. The X manipulator motor features a resolution of ~80,000 steps per millimeter while the Y manipulator (with the 50:1 gearing) has a resolution of ~400,000 steps per millimeter resulting in superb spatial positioning accuracy limited only by slight backlash from deflections of the manipulator arms during operation.

The stage itself features a 9x12 array of 8-32 tapped holes with a spacing of 12.7 mm (0.5”) which can be used to attach samples or sample arrays of arbitrary shapes and sizes in addition to other devices such as thermocouples and tools for ion beam diagnostics (e.g., quartz slides which scintillate under the ion beam to aid in beam shaping and positioning). The stage also features a pattern of shallow slots around the exterior

of the work area which, along with the array of tapped holes, can serve as fiduciary marks to aid in stage and beam positioning by an operator or autonomously by a computer when coupled with digital image correlation (DIC) – a potential use for future experiments.

4.3 Methods and Materials

Cr-Fe-Mn-Ni compositional arrays produced in this work were synthesized via direct energy deposition (DED) carried out using an Optomec LENS MR-7 equipped with a 1-kW Nd:YAG laser (spot size 600 μm) and four independently controlled powder hoppers. Each hopper was filled with a single elemental powder. Elemental powders used were in the size range of 45-150 μm in diameter and were produced via gas atomization, which produces nominally spherical powders. All samples were printed in an argon atmosphere, with O_2 content monitored and maintained below 10 ppm, on unheated 316-stainless-steel build plates, 6.35 mm in thickness, while the laser focus was set to be ~380 μm below the surface of the build layer. Since using elemental powders to perform in situ alloying via DED often leads to the incorporation of unmelted elemental powders in the printed alloy matrix [148, 192], multiple intermittent laser remelting passes were employed to ensure chemical homogeneity. The printing regime for a single sample (illustrated in Figure 35) was as follows:

(1) While flowing powder (mixed in flight), deposit a layer of material with a single rastering pass with the laser over the cross section of the part.
(2) Without powder flowing, perform one or more rastering passes with the laser over the cross section of the part – entirely remelting the previously deposited layer with each pass.
(3) Move to next layer height and prepare for next deposition layer.

For each sample in a compositional array, this cycle was repeated for a total of five deposition layers, with a square cross section 10 mm on a side. The printhead was moved vertically 1 mm after each complete deposition + remelt cycle, loosely resulting in a layer thickness of ~1 mm and a total height of ~5 mm for

each sample, with some variation as a function of composition. Each sample was printed using two remelting passes (rotated 90°) for each deposited layer and using a hatch spacing of 190 μm and a speed of 21.16 mm/s during remelting passes and a hatch spacing of 380 μm and speed of 10.58 mm/s during deposition passes. The laser power during remelting and deposition passes was 500 W and 350 W, respectively, when printing each four-element alloy, while laser powers for unary, binary, and ternary alloys were empirically adjusted, based upon the melting point of the composition, to improve the likelihood of successful printing. The laser powers used are summarized in Table 7.2 in the Appendix section of this paper.

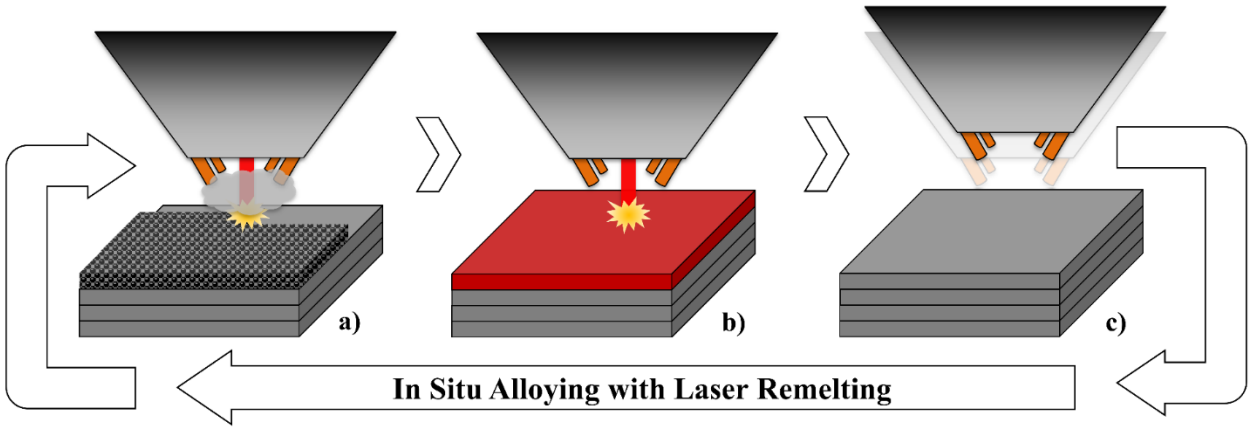

Figure 35*: Schematic illustration of in situ alloying via DED with the incorporation of intermittent laser remelting passes (not drawn to scale). a) Powder, illustrated by the gray plume, is flown through copper nozzles (shown in orange) where it is melted and consolidated by the laser as it passes over the surface of the part. b) Without powder flowing, the recently deposited layer is remelted by the laser to incorporate any unmelted powders and improve homogeneity. c) After remelting, the printhead is advanced vertically in preparation for printing the next layer.*

To produce the correct sample compositions, mass flow rate versus hopper auger rotations-per-minute (RPM) calibration curves were first collected. Indeed, when calculated using only a mass balance of the incoming powders, deviations in the printed composition from the target composition are often observed because of the differences in the chemical, morphological, and flow properties of elemental powders. To correct for these deviations, multiple iterations of compositional arrays were printed with the composition of each sample being measured and the mass flow rates calibration curves empirically adjusted by introducing a “retention rate” fitting parameter. Then the relationships between mass flow rate and printed composition are recalculated using a least-squares minimization after each printing iteration. If the

terminating surfaces of the as-built samples are flat and nearly coplanar, the composition can be measured quickly and accurately (within ± 1 at%) via X-ray fluorescence (XRF). However, if there are significant height variations in the different printed samples, composition measurements via energy-dispersive spectroscopy (EDS) were found to be more reliable, albeit slower. A more detailed description of the composition calibration optimization process is given in reference [167]. In this work, all as-built compositions were measured by EDS using a JEOL JSM-6610 scanning electron microscope (SEM). Once satisfactory composition calibration was achieved, whereby deviations between measured composition and target composition were typically less than ~5 at% for each element in each sample (see in the Appendix), a compositional array featuring targeted compositions of each pure element, every $X_{50}Y_{50}$ binary, every $X_{33}Y_{33}Z_{33}$ ternary, every $W_{18}X_{27}Y_{27}Z_{27}$ and $W_{15}X_{35}Y_{15}Z_{35}$ quaternary, and the equimolar $Cr_{25}Fe_{25}Mn_{25}Ni_{25}$ was printed, shown in Figure 36 (note that in this picture the plate was media blasted to remove powders adhered to the surface). All samples were printed using an estimate molar flow rate of 0.3 mols/min, however, due to differences in laser parameters and material behaviors, the final heights of the samples were varied. Consequently, to aid in further processing, the samples were leveled using wire electrical discharge machining (EDM) to produce coplanar sample heights.

***Figure 36**: Photograph of the as-built Cr-Fe-Mn-Ni array printed on a 316-stainless-steel build plate after media blasting to remove adhered powders. Prior to any machining, sample heights and surface finish as printed vary as a function of composition.*

As-fabricated alloys produced by DED, and more generally by additive manufacturing, often exhibit chemical segregation, dislocation structures, and residual stresses resulting from the initial solidification process during the deposition of a given layer. These effects are further influenced by the solid-state heat treatment that will inevitably occur by the thermal cycling caused by the melting of the subsequently deposited layers [171]. To alleviate variations in these effects in the different printed alloys, the entire compositional array was homogenized in a water-cooled Materials Research Furnaces (MRF) vacuum furnace (base pressure ~10^{-6} torr) at 1000 °C for 24 hours followed by furnace cooling to room temperature at an average cooling rate of approximately 1 °C/s. The temperature of 1000 °C was selected as the highest temperature attainable without inducing insipient melting in any of the printed alloys, which is dictated by the relatively low melting point of the MnNi binary alloy (~1020 °C) [193]. After the homogenization treatment, the composition of each sample was measured using a handheld SciAps X-200 series XRF detector. The XRF (separately calibrated against EDS) was employed as a high throughput method for compositional analysis on multiple alloy samples. The equilibrium phases of each measured sample composition at 1000 °C were calculated using the CALPHAD method, via the Pandat software and

the PanHEA thermodynamic database. The entire compositional array was mechanically polished progressively from 120 through 1200 SiC grit papers, followed by polishing with 3-μm and 1-μm diamond suspensions and finally with 0.04-μm colloidal silica to produce surface finish required for ion irradiation in accordance with ASTM E521-96 [194]. Surface roughness measurements were performed using a Zygo New View white-light interferometer.

Heavy-ion irradiation was performed at the University of Wisconsin Ion Beam Laboratory (UW-IBL) using a defocused beam of 4-MeV Ni^{2+} ions at room temperature. Prior to irradiation, the compositional array was affixed to a custom XY stage, large enough to accommodate the size of the plate. Half of each sample was masked by a steel-foil mask to preserve half of each sample in the unirradiated condition, as illustrated in Figure 37. To calculate the fluence necessary to produce a target damage level of 50 dpa at the damage peak, the quick Kinchin-Pease (KP) calculation mode was used in SRIM and displacement energies of each element were set to be 40 eV while the lattice binding energy and surface binding energy were each set to 0 eV, as discussed in reference [195]. Since the average masses of Cr, Fe, Mn, and Ni are similar (with pure nickel and chromium representing the largest deviations of ± 6% from the average), displacement and binding energies of each element were treated as identical, and the densities of each alloy are comparable (as most alloys examined were predicted to be either mostly or entirely face-centered cubic (FCC) by CALPHAD). To simplify the irradiation experimental setup, each alloy was irradiated to the same fluence of 4-MeV Ni^{2+} calculated to produce a peak damage of 50 dpa in equimolar CrFeMnNi, which was found to be 5.33×10^{16} ions/cm^2. Figure 38 shows the damage profiles in four equimolar alloys in the Cr-Fe-Mn-Ni composition space after a fluence of 5.33×10^{16} ions/cm^2 using 4-MeV Ni^{2+} ions in which the damage profiles appear more similar with increasing compositional complexity.

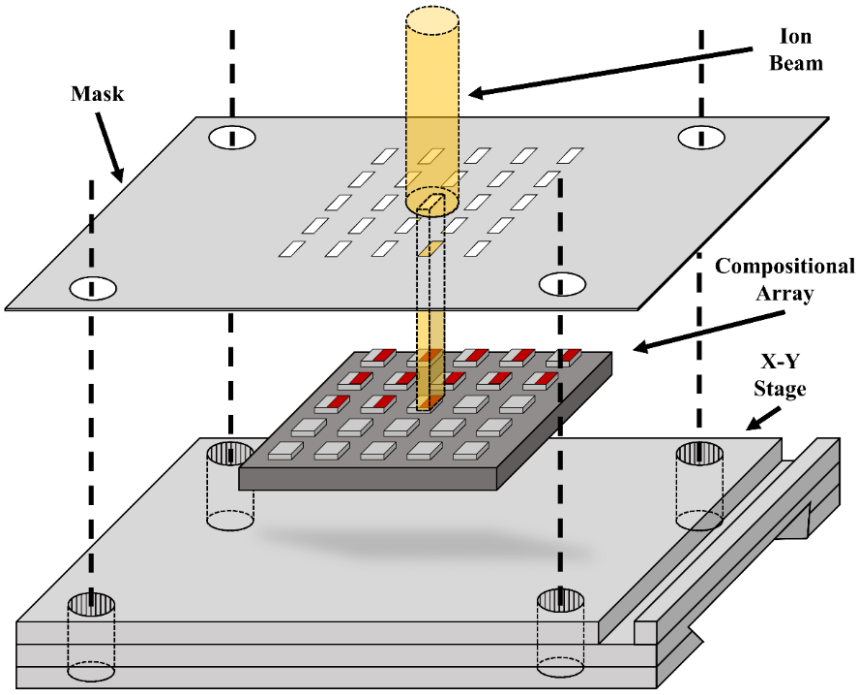

***Figure 37**: Exploded schematic of the Cr-Fe-Mn-Ni compositional array mounted to custom XY sample stage. Half of each sample in the compositional array is masked by steel foil.*

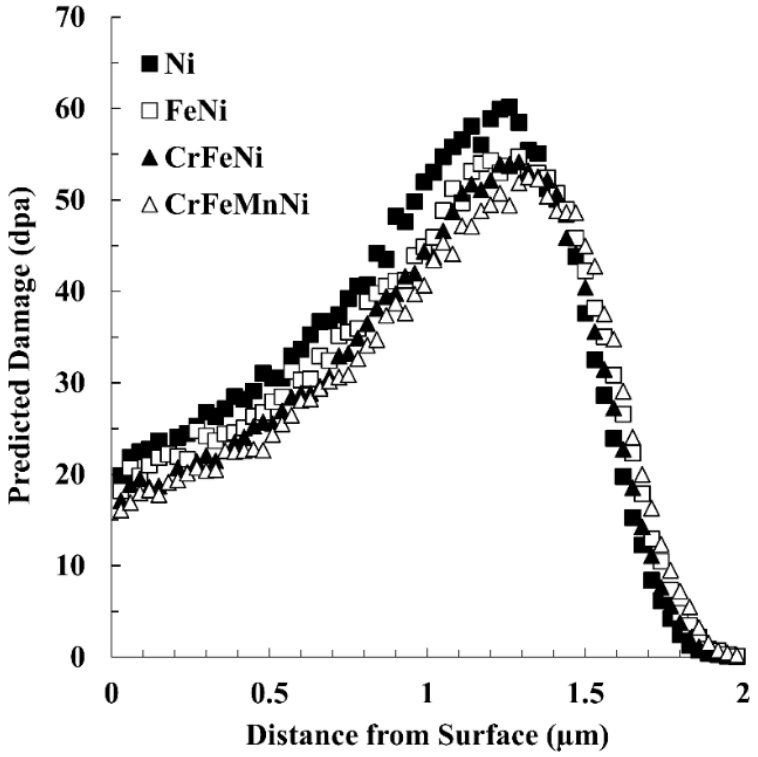

***Figure 38**: Damage profiles calculated from SRIM data of various equimolar alloys irradiated with 4-MeV Ni^{2+} ions to a fluence of $5.33x10^{16}$ ions/cm^2.*

Following ion irradiation, X-ray diffraction (XRD) studies were performed, using a Bruker D8 Discovery X-ray diffractometer equipped with a Cu K-alpha X-Ray source, with a spot size of 0.1 mm, and an automated sample stage. The small X-ray spot size and the thickness of each printed sample (several millimeters) ensure that individual samples can be illuminated by X-rays without generating additional signal from the stainless-steel substrate or other nearby samples. XRD was performed on both the irradiated and unirradiated regions the samples to identify any radiation induced phase changes, including potential precipitate dissolution from ballistic mixing, as well as to compare the phases in the unirradiated regions with CALPHAD predictions. The latter point is particularly critical for alloy design purposes [163, 196]. Nanoindentation measurements were performed along a 6-mm-long line in the center of each sample crossing the interface between the unirradiated/irradiated regions to evaluate radiation-induced hardness changes. Nanoindentation measurements were performed using a Bruker Hysitron TI-950 Triboindenter, equipped with a Berkovich tip. All measurements were performed using load control mode in which the maximum applied load was fixed at 6000 μN. The experiment was performed into two steps; the loading step, where the load is applied to push the indenter into the material at a loading rate of 1 mN/s until it reaches the maximum specified load, followed by the unloading step, where the indenter is drawn back to its original position. Uncertainty in the nanoindentation measurements primarily originates from estimation of the contact area between the indenter and the material, and it is generally accepted to be ~5% or less [197]. For each sample, a line scan of indents was performed across the irradiation interface with 200 μm lateral step size. Samples were characterized in the as-built state and after homogenization + irradiation using JEOL JSM-6610 scanning electron microscope (SEM) equipped with EDS. ImageJ® was used to threshold SEM images and identify individual pores in the samples to determine pore size distributions and total porosity by calculating the area fraction.

4.4 Results

In order to perform accurate characterization of samples using XRD and XRF, a minimum area of sample uniformity is needed based on the spot size of the X-ray source from each technique. In this study,

the spot size of the XRF gun, a circular area approximately 6 mm in diameter, dictated the minimum geometry necessary for measurements. As a result, three samples, shown in Figure 36, have not been included for analysis namely the sample in Row 1 / Column 3, Row 2 / Column 1, and Row 3 / Column 1, corresponding to target compositions of pure Mn, CrMn, and CrFeMn, respectively. In general, high-Mn compositions presented a challenge to printing due to volatilization and this problem is often exacerbated when paired with higher melting point elements (e.g., Cr), which themselves necessitate higher laser powers to melt sufficiently. For ease of discussion, samples will be referred to hereinafter by their compositions, in at%, as measured by XRF after homogenization.

4.4.1 Alloy Compositions

The compositions of the alloys from the Cr-Fe-Mn-Ni compositional array are plotted against their as-built targeted compositions in Figure 39 in both the as-built and homogenized conditions. While XRF is the preferred method for measuring chemical composition for these samples due to its speed, the variations of height and surface finish of the samples in the as-built condition preclude the use of XRF since the snout of the XRF gun must be placed flat against the measurement surface. To remedy this, chemical composition in the as-built condition was measured using EDS while after homogenization and leveling via wire EDM, XRF was used. For materials with extensive standard libraries (e.g., steels), XRF and EDS have been found to be in close agreement (±1 at%), thus, the chemical compositions measured using these two techniques is used interchangeably for the Cr-Fe-Mn-Ni alloys produced in this study. The measured compositions were originally within ~5 at% of their targeted compositions, with only one outlier deviating by more than 10 at%. After homogenization at 1000 °C for 24 hours under vacuum, a large decrease in the Mn content was observed which scaled with the initial Mn content of the alloy. The suspected cause for the loss of Mn during homogenization is the relatively high vapor pressure of Mn at 1000 °C, approximately 10^{-2} torr [198], which is several orders of magnitude larger than the base pressure of the MRF vacuum furnace used for heat treatment, which was approximately 10^{-6} torr.

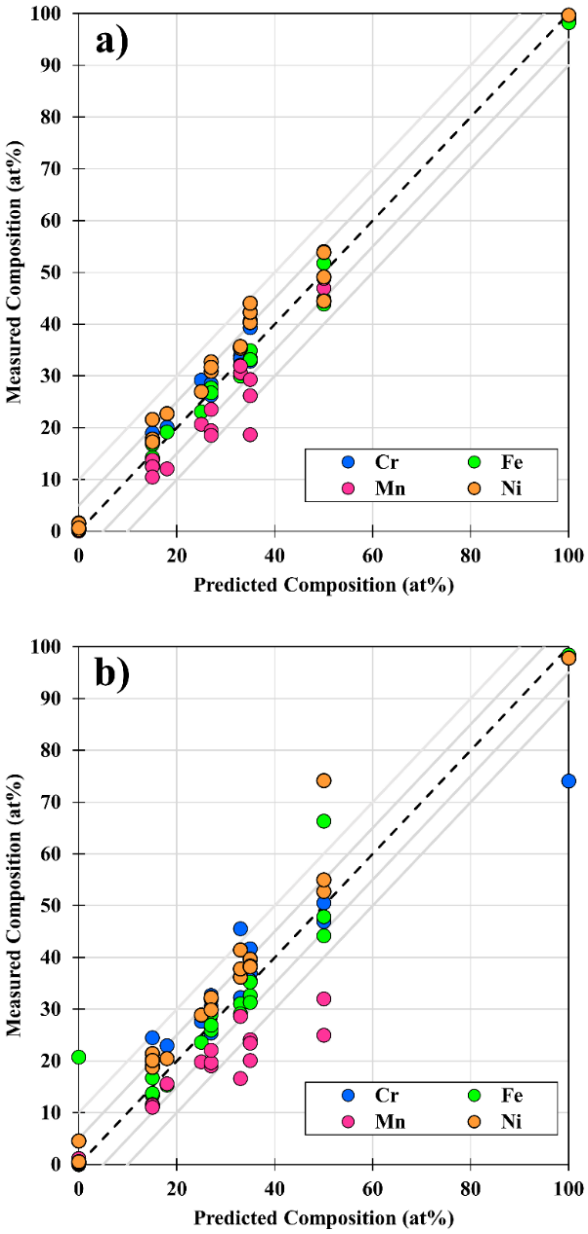

***Figure 39**: Measured composition versus predicted composition for each element in each sample of the Cr-Fe-Mn-Ni compositional array measured by a) EDS in the as-built state and by b) XRF in the homogenized state.*

In addition to Mn loss during the homogenization treatment, effects of additive manufacturing geometry on the composition were observed in the printing of pure Cr, where rather than measuring close to 100 at% Cr, the composition measured by XRF was found to be $Cr_{74}Fe_{21}Mn_1Ni_4$. The presence of Fe, Mn, and Ni in the measured ratios inside the Cr sample are likely due to substantial intermixing of the printed Cr and the SS-316 build plate caused by the comparatively short build height of the Cr sample, seen

in the top left corner of the build plate in Figure 36. Since the penetration depth of the electrons used to measure the composition via EDS in the as-built condition is substantially shorter than that of the X-rays used in XRF, it is unclear whether the intermixing of the Cr with the SS-316 build was caused primarily during printing or as a result of the homogenization heat treatment. In any case, the Cr sample serves to motivate the need to build up samples far beyond the surface of the substrate to avoid effects from the substrate and the interface region. Of course, one could use the substrate material as an alloying element, which has been successfully demonstrated as a high-throughput in situ alloying technique in [199].

4.4.2 Phases

XRD was used to examine the phase distribution of each sample from the Cr-Fe-Mn-Ni compositional array in both the irradiated and unirradiated regions. As may be expected from a room-temperature irradiation, the XRD patterns in the irradiated regions of each sample appear very similar to their unirradiated counterparts indicating no substantial new phases. Each alloy was found to consist of either a single-phase body-centered cubic (BCC) structure, a single-phase face-centered cubic (FCC) structure, or a combination of FCC and BCC phases. To compare with the expected phases of the Cr-Fe-Mn-Ni system from CALPHAD, compositions spanning the entire Cr-Fe-Mn-Ni composition space were simulated using the Pandat high-throughput calculation (HTC) function, with a step size of 5 at%, at 1000 °C – the temperature used for homogenization of the compositional array. The results from the CALPHAD HTC are shown in Figure 40 with the experimental XRD results overlaid. The phases identified experimentally via XRD are in remarkable agreement with the equilibrium phases predicted by CALPHAD simulation. In each of the multiphase (FCC+BCC) HEAs, the FCC phase is slightly enriched in Ni while the BCC phase is significantly enriched in Cr. The boundary between the FCC and FCC+BCC regions predicted by CALPHAD, where the most experimental data is present, matches the experimental data within a few at%. These variations are close to the uncertainty of the XRF measurements of approximately ± 1 at%. However, two notable outliers were observed: pure Fe and $Fe_{67}Mn_{33}$. At 1000 °C, both pure Fe and $Fe_{67}Mn_{33}$ were expected to be a single FCC phase but were instead observed experimentally to be BCC,

and FCC + BCC, respectively. Evidently, these two alloys underwent solid-state phase transformation as a result of the non-instantaneous cooling rate of the compositional array following the homogenization heat treatment since pure Fe is expected to transition from FCC to BCC at approximately 912 °C and $Fe_{67}Mn_{33}$ is similarly predicted to become FCC + BCC at lower temperatures.

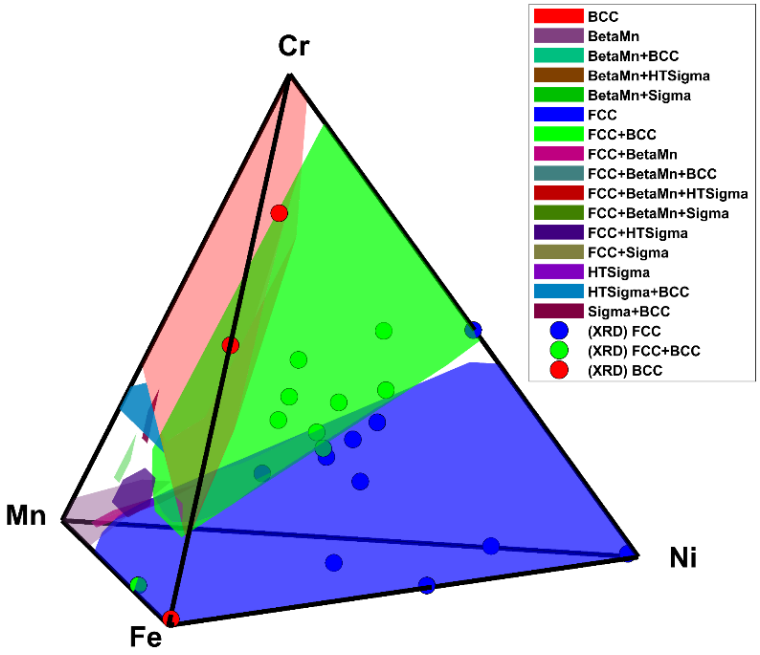

***Figure 40**: HTC CALPHAD equilibrium phases of the Cr-Fe-Mn-Ni composition space at 1000 °C with experimental XRD results overlaid.*

4.4.3 Microstructural Characterization

After irradiation, samples from the compositional array were examined using SEM and EDS. The irradiated region of each sample was distinguishable from the unirradiated region by its darker contrast when imaged using an in-lens secondary-electron detector, which may be caused by changes in surface morphology or deposition of neutral carbon atoms during irradiation [200]. However, besides this slight change in contrast, no microstructural differences were observed between the unirradiated and irradiated regions of the samples. To highlight the different microstructures observed in the Cr-Fe-Mn-Ni system, Figure 41 shows the SEM images and EDS chemical maps taken from the unirradiated region of three CCAs, $Cr_{19}Fe_{31}Mn_{11}Ni_{39}$, $Cr_{28}Fe_{23}Mn_{20}Ni_{29}$, and $Cr_{42}Fe_{17}Mn_{20}Ni_{21}$ with approximate Cr:Ni ratios of 1:2,

1:1, and 2:1, respectively. For $Cr_{19}Fe_{31}Mn_{11}Ni_{39}$, a single chemically homogeneous phase is observed with fine uniformly distributed pores with an average area of 0.15 ± 0.10 μm^2 and a total porosity of 0.55%. With increasing Cr content and decreasing Ni content, $Cr_{28}Fe_{23}Mn_{20}Ni_{29}$ shows the formation of BCC Cr-rich precipitates uniformly distributed throughout the FCC matrix and an increase in both the average pore size and total porosity which was measured to be 0.20 ± 0.16 μm^2 and 1.35%, respectively. Further increase in the Cr:Ni ratio, in the case of $Cr_{42}Fe_{17}Mn_{20}Ni_{21}$, leads to an increase in the Cr-rich BCC phase fraction, which rather than forming discrete precipitates in an FCC matrix instead forms a globular interconnected network intertwined with the FCC phase. Relative to the previous two alloys, the average pore size and total porosity was also measured to increase in $Cr_{42}Fe_{17}Mn_{20}Ni_{21}$ to 0.34 ± 0.34 μm^2 and 1.95%, respectively. Overall, from the EDS chemical mapping, Cr and Ni are observed to segregate more strongly than Fe and Mn during this phase separation, and both the pore size and total porosity area fraction was observed to increase with increasing Cr-rich BCC phase fraction.

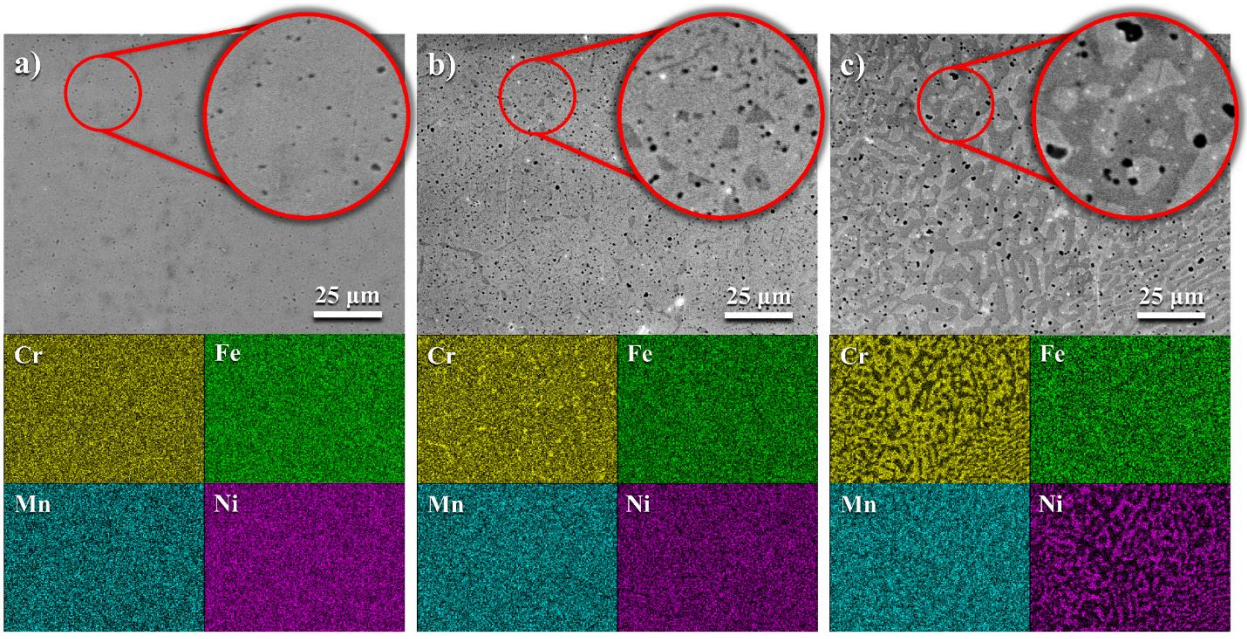

Figure 41: SEM images and EDS chemical maps from the unirradiated regions of a) $Cr_{19}Fe_{31}Mn_{11}Ni_{39}$ b) $Cr_{28}Fe_{23}Mn_{20}Ni_{29}$, and c) $Cr_{42}Fe_{17}Mn_{20}Ni_{21}$. Each alloy consists of a primary FCC phase with an increasing amount of the BCC Cr-rich phase (dark contrast) from a) to c). Insets are provided in red circles at a magnification 3x greater than the base images to highlight the porosity distributions.

4.4.4 Hardness

While phenomena such as void swelling, RIS, and radiation-induced precipitation would not be expected in Cr-Fe-Mn-Ni alloys irradiated at room temperature, due in part to the lack of vacancy mobility, radiation hardening from point defects and from the formation of self-interstitial atom (SIA) clusters would be expected [201]. Figure 42 shows the nanoindentation line profiles of two *less compositionally complex* single-phase BCC solid-solution alloys. Here, a sharp step increase in hardness is observed for $Cr_{51}Fe_{49}$ from ~3.5 GPa to ~5 GPa between the unirradiated and irradiated region while the comparatively softer Fe shows a more gradual increase from ~1.75 GPa to ~3.25 GPa. The gradual increase is likely caused by the Al-foil mask interface not being quite perpendicular to the nano-indentation line scan.

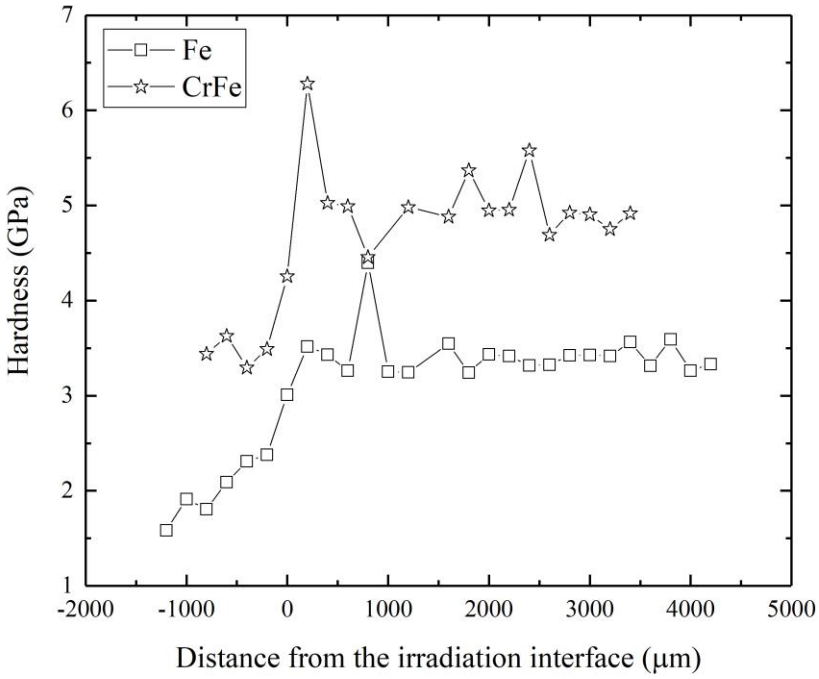

***Figure 42**: Hardness profiles across the unirradiated/irradiated interface of select single-phase BCC alloys measured via nanoindentation. Since the unirradiated region for these two alloys was only sampled by the first ~5 point of each scan, hardness values have been plotted as a function of distance from the sample edge for clarity.*

Alongside the single-phase BCC alloys, many single-phase FCC alloys were examined, including several single-phase FCC CCAs, where evidence of irradiation hardening was clearly visible. Figure 43 shows a pair of typical load-versus-displacement curves, generated from nanoindentation of the unirradiated and irradiated regions of $Cr_{20}Fe_{35}Mn_{24}Ni_{20}$. To achieve the target load of 6000 μN, a displacement of ~300

nm is necessary in the unirradiated condition while the same load is reached after a displacement of ~250 nm in the irradiated condition, corresponding to an increase in hardness from ~2.5 GPa to ~3.5 GPa after irradiation. A comparison of the hardening behavior of various FCC CCAs is shown in Figure 44, which includes the nanoindentation line profiles centered on the unirradiated/irradiated interface of $Cr_{20}Fe_{35}Mn_{24}Ni_{20}$, $Cr_{19}Fe_{31}Mn_{11}Ni_{38}$, and $Cr_{23}Fe_{26}Mn_{19}Ni_{32}$. In the unirradiated region, the hardness values of the FCC CCAs range from ~2.5-3.25 GPa, while after irradiation the hardness values range from ~3.5-4.75 GPa, thus exhibiting a slight improvement over the BCC Fe and CrFe alloys.

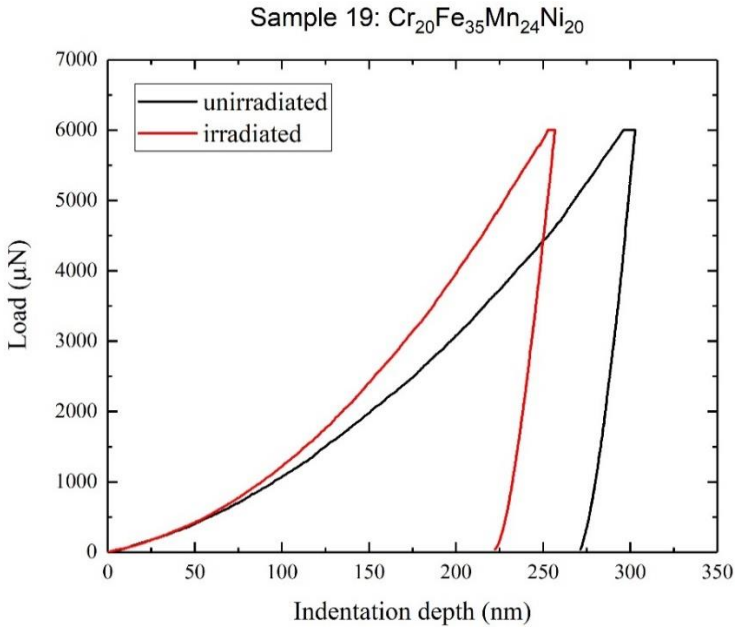

***Figure 43**: Representative load vs. displacement curves from the unirradiated and irradiated regions of the FCC CCA $Cr_{20}Fe_{35}Mn_{24}Ni_{20}$*

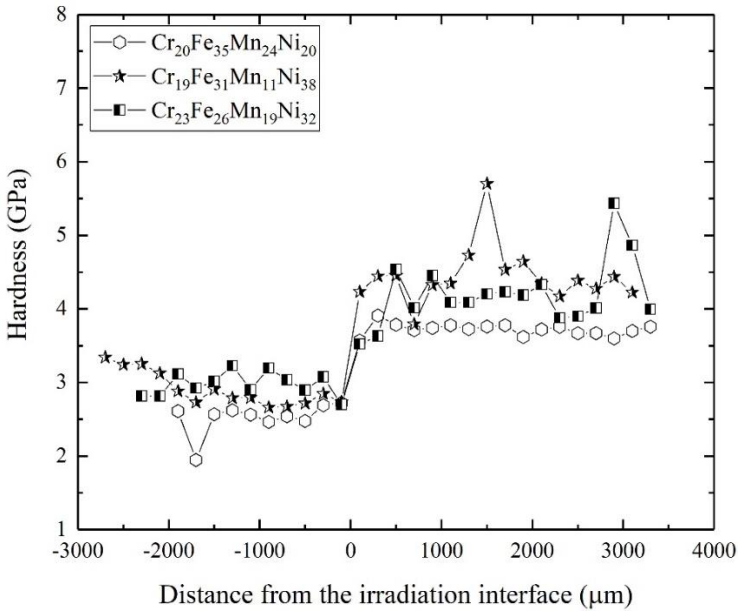

Figure 44*: Hardness profiles across the unirradiated/irradiated interface for several single-phase FCC CCAs measured via nanoindentation.*

In each of the single-phase alloys, the hardness before and after irradiation can be readily determined from the individual nanoindentation line scans. However, for the two-phase (FCC+BCC) CCAs, even if a step increase in hardness across the unirradiated/irradiated interface is observed, the scatter in hardness values within a region is often substantial. This makes it difficult to discern the absolute hardness of the individual phases. Since nanoindentation measurements probe a finite interaction volume several micrometers in all directions [197], the size and spatial distribution of second phases affect the hardness measured from a single point and can produce a distribution of hardness values for a two-phase system rather than two discrete hardness values, one for each phase. To try and visualize the data from the multiphase alloys in a meaningful way, Figure 45 shows histograms of the unirradiated and irradiated areas, respectively, pooled from every alloy examined where the interface between the unirradiated/irradiated interface is discernable in the hardness data. A kernel smoothing function was applied to the raw hardness data to produce a probability density function (PDF) for both conditions; the bin size for both the histograms and the kernel smoothing functions was set to 0.25 GPa. In the unirradiated histogram (Figure 45a), two primary groups of hardness values were observed centered at 3 GPa and 4.5 GPa, which can generally be attributed to the Ni-rich FCC phase and the Cr-rich BCC phases measured in many of these alloys by XRD

(compositions inferred from CALPHAD), with the exception of a few of the unary and binary alloys (e.g. Fe, $Fe_{67}Mn_{33}$). After irradiation (Figure 45b), the two original groups of hardness data merged into a single group of hardness values, centered at approximately 4.25 GPa. Had the FCC and BCC phases both hardened to the same extent, the same bimodal hardness distribution seen in the unirradiated condition would be expected in the irradiated condition (only offset to higher hardness values). However, this was not observed suggesting that the Cr-rich BCC phase in the two-phase Cr-Fe-Mn-Ni CCAs is more resistant to irradiation hardening than the Ni-rich FCC phase.

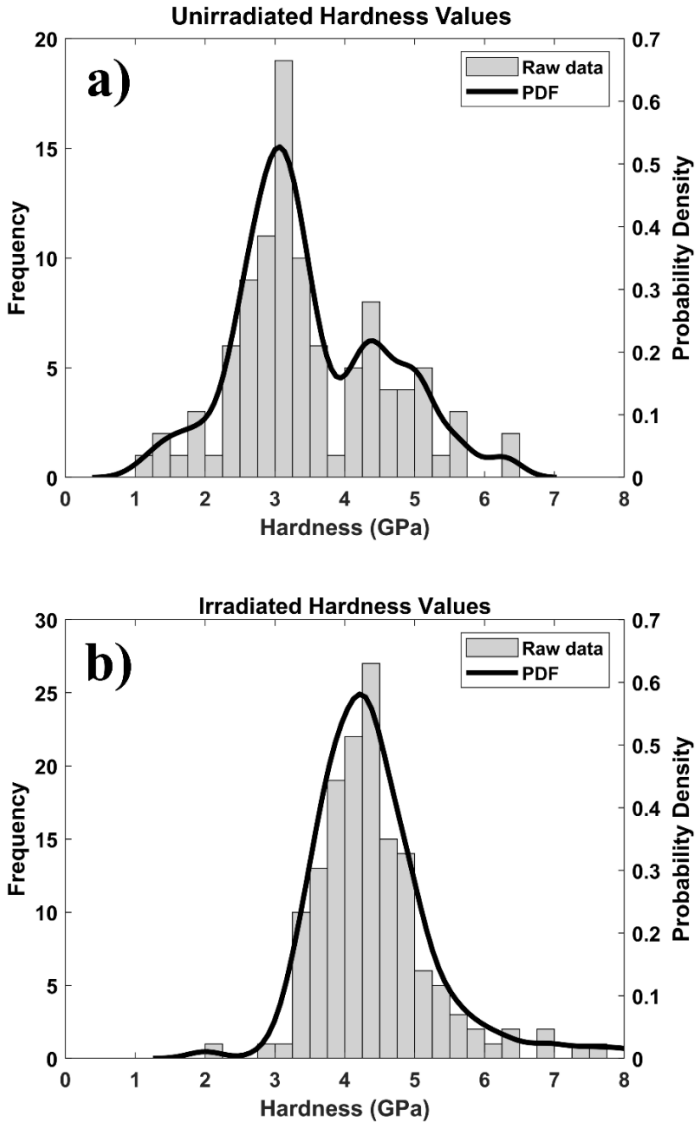

Figure 45*: Histograms of the hardness values measured from a) the unirradiated region and b) the irradiated region of each alloy via nanoindentation. Alloys in which the unirradiated/irradiated interface was undiscernible have been omitted.*

4.5 Discussion

To the best of the authors' knowledge, this study represents the first time an additively manufactured compositional array has been irradiated in a high-throughput manner. Producing compositional arrays using in situ alloying via additive manufacturing is, however, not without its challenges. Specifically, minimizing porosity and maintaining compositional accuracy after heat treatment are two area whose improvement would have a substantial impact on the robustness and utility of additive manufacturing as a high-throughput irradiation tolerance screening technique.

Prior to homogenization, some loss of Mn from the compositional array was anticipated and the depth of the Mn-depleted layer was estimated using isotope tracer diffusion data from the well-studied austenitic 316 stainless steel (SS-316) system, as a surrogate for the Cr-Fe-Mn-Ni CCAs of which little diffusion data is available for in the literature. From reference [202], the lattice diffusion coefficient of Mn in SS-316 at 1000 °C was calculated to be 8.84×10^{-16} m^2/s. Using the characteristic diffusion length as an estimate suggests a Mn-depleted depth of approximately 17.5 μm in thickness under the homogenization treatment used in this study. This thickness was considered negligible when compared to the amount of material removed during mechanical grinding and polishing after heat treatment. However, while this assumption remains valid for the low-Mn alloys, it may not be true for higher Mn contents. The cause of the increased Mn depletion for alloys with higher Mn content is likely due the depressed melting point of high-Mn alloys, which causes the homogenization temperature to translate to a substantially higher homologous temperature for these alloys. This would of course lead to a lower vacancy activation energy for the high-Mn alloys, resulting in higher diffusion coefficients. For example, using the Pandat software with the PanHEA database, the melting point (T_{mp}) of equimolar CrFeMnNi was calculated to be 1268 °C while the melting point of $Mn_{50}Ni_{50}$ was calculated to be 1045 °C corresponding to homologous temperatures of $0.83T_{mp}$ and $0.97T_{mp}$, respectively. As such, the measured compositions of equimolar CrFeMnNi and $Mn_{50}Ni_{50}$ after homogenization were found to be $Cr_{27}Fe_{24}Mn_{20}Ni_{29}$ and $Mn_{25}Ni_{75}$, respectively. From this finding, unless

homogenization heat treatments can be performed at elevated pressures without substantial oxidation, it is recommended that Mn content is kept below ~25 at% to prevent substantial volatilization.

Each sample in the compositional array has some degree of porosity, as measured by SEM. It is necessary to understand both the distribution and the causes for this porosity so that it can be minimized as this HTP process is further developed. Few materials synthesis techniques are able to produce materials at 100% of their theoretical density, however, laser-based additive manufacturing is particularly prone to introducing pores into printed material when laser parameters are not optimized [203]. While there are many sources of porosity in additively manufactured materials, two of the most common sources in DED are keyhole (metal-vaporization) porosity and entrapped-gas porosity, both of which become more common with increasing laser power. Both types of pores stem from fluid instabilities in the melt pool near the metal-vapor depression directly under the laser, which can trap metal vapor from the deposited material and/or inert gas from the build environment upon solidification. Pores containing metal vapor quickly become evacuated as the vapor condenses on cooling, however, pores with entrapped inert gases maintain an internal gas pressure on cooling. In addition to porosity introduced during synthesis, heat treatment can also produce porosity by the Kirkendall effect due to differences in diffusion coefficients between the dendritic/interdendritic regions in the solidification structure or during the formation and evolution of secondary phases. To remove these pores, hot isostatic pressing (HIP) is often used, which is effective at closing evacuated pores including metal-vapor pores and Kirkendall voids. However, HIPping is less effective at removing entrapped gas pores due to the internal gas pressure and low solubility of inert gases, such as argon, in solid metals [204]. To assess the role of the Kirkendall effect on porosity of the samples in the Cr-Fe-Mn-Ni compositional array, the porosity in the FCC CCAs (Figure 41) can be compared to the porosity of the pure Fe sample (Sample #2). The pure Fe sample was measured to have a total porosity of 0.48% with an average pore size of 0.12 ± 0.06 μm^2. Since this sample consists of a single element, there should be no additional porosity caused by Kirkendall voiding during heat treatment. Therefore, this level of porosity can be considered a baseline for samples in the compositional array. By comparison, the total

porosity in the single-phase FCC CCA $Cr_{19}Fe_{31}Mn_{11}Ni_{39}$ was measured to be 0.55% with an average pore size of 0.15 ± 0.10 μm^2, which is quite close to the baseline level. This suggests minimal Kirkendall voiding occurs as a result of the elimination of chemical segregation from the solidification structure upon homogenization. In contrast, as the Cr content is increased, leading to the formation of a BCC phase in $Cr_{28}Fe_{23}Mn_{20}Ni_{29}$ and $Cr_{42}Fe_{17}Mn_{20}Ni_{21}$, the total porosity increases to 1.35% and 1.95%, respectively. Moreover, in addition to the population of submicron pores distributed uniformly throughout every printed sample, $Cr_{42}Fe_{17}Mn_{20}Ni_{21}$ (shown in Figure 41c) features an additional population of larger pores positioned at the interface between the FCC and BCC phases. This would indicate substantial Kirkendall voiding increasing with the BCC phase fraction. Since a large source of pores in the two-phase CCAs appears to be Kirkendall voiding from the FCC+BCC phase separation, the total porosity of these samples, and future compositional arrays, should be able to be reduced substantially with a HIP treatment.

The assortment of Cr-Fe-Mn-Ni alloys irradiated in this campaign offer several insights into both the hardening response of this class of CCAs and the implications of using high-throughput techniques in the development of radiation-tolerant materials. Firstly, radiation-induced hardening was observed in both FCC and BCC CCAs as well as several multiphase (FCC+BCC) CCAs. However, the degree of hardening is dependent on both the crystal structure and the composition of the phase. For example, while the irradiated pure Fe and CrFe binary alloy show an average increase in hardness of ~1.5-2 GPa (Figure 42), the hardness of the Cr-rich BCC phase present in the two-phase CCAs showed negligible change in hardness (Figure 45). In contrast, the magnitude of the change in hardness and the average hardness of the single-phase FCC CCAs (Figure 44) seem to be relatively insensitive to modest changes in concentrations of Fe, Mn, and Ni in the alloys, whose hardening due to irradiation all ranged around ~1-1.5 GPa. Overall, the hardness values of the single-phase FCC CCAs before and after irradiation in this work are in good qualitative agreement with hardness measurements from low-temperature neutron irradiations of a comparable Cr-Fe-Mn-Ni FCC HEA [169], which also was measured to have an initial hardness ~3 GPa and a change in hardness of ~1.5 GPa after neutron irradiation to 1 dpa – a damage level above which radiation-induced hardening would be

expected to saturate [205]. This builds confidence in the validity of using additively manufactured compositional arrays to predict the response of CCAs under reactor conditions.

To understand the exact atomistic mechanisms underpinning the irradiation response of a material typically requires the use of TEM or equally in-depth and time-consuming techniques. However, this is expressly not the purpose of employing HTP screening techniques. Instead, HTP techniques, including the ones employed in this study, enable researchers to expand their search ranges and explore alloy compositions that would otherwise be time and cost prohibitive. Incidentally, the HTP synthesis, irradiation, and characterization methodology presented in this study is an embodiment of the Pareto principle, wherein 80% of the challenge can be overcome with 20% of the effort. While HTP techniques will always need to be coupled to more precise *low-throughput* techniques, their implementation serves as an enabling approach to accelerate the development of CCAs and novel materials for advanced nuclear technologies in general.

The time savings resulting from HTP techniques cannot be overstated. To quantify this assessment, one needs to consider the time needed to synthesize, irradiate, and characterize 25 alloys using traditional approaches. To arc melt a chemically homogeneous button, careful weighing of the precursor elements must be performed followed by several melting iterations with intermediate flipping of the melted button, which often requires the arc melter to be brought back to atmospheric pressure to flip the button and/or clean the chamber depending on the type of system and materials being melted. Optimistically, this entire process may take ~1-2 hours per alloy. By comparison, each alloy in the Cr-Fe-Mn-Ni compositional array featured in this study took approximately 10 minutes to print with less than 30 seconds between switching compositions, meaning the array of 25 compositions was able to be synthesized, conservatively, in less than 5 hours – representing a time savings between fivefold and tenfold. Similar time savings are achieved for sample preparation (because an entire compositional array can be polished simultaneously), during irradiation, where only one vacuum cycle between atmospheric pressure and ultra-high vacuum is necessary to load the compositional array, and for characterization techniques where the regular spacing of samples

in the compositional array allows a user to take full advantage of automated data collection (e.g. in the case of XRD and nanoindentation), as has been demonstrated in this study.

4.6 Conclusions and Future Work

Using DED to produce an array of CCAs, which were subsequently irradiated and characterized, additive manufacturing has been demonstrated to be an enabling technology for the high-throughput (HTP) assessment of the irradiation properties of alloys, specifically for the Cr-Fe-Mn-Ni family of CCAs, which show promise as radiation-tolerant materials. CALPHAD simulations of the Cr-Fe-Mn-Ni composition space have been demonstrated to accurately predict the phase distributions of concentrated alloys after homogenization at 1000 °C, as confirmed by XRD. In total, 25 alloy compositions were rapidly synthesized and irradiated, 23 of which were of sufficient quality to be characterized using XRF, XRD, and nanoindentation. Radiation-induced hardening of several CCAs was measured, with hardness increases ranging from ~1-1.5 GPa, which is comparable to hardening observed in neutron-irradiated Cr-Fe-Mn-Ni HEAs in the literature. In general, the combination of HTP techniques in this study including additive manufacturing, CALPHAD modeling, and automated characterization techniques, has demonstrated immense time savings over conventional exploratory alloy development processes. Assessment of compositional accuracy and porosity distributions in the additively manufactured compositional array has provided guidance for future printing campaigns, including reducing Mn content below ~25 at% and adding a HIP treatment to eliminate metal-vapor pores from manufacturing and Kirkendall voids from heat treatment. Future work will focus on performing ion irradiation at higher temperatures to promote other radiation-induced phenomena such as void swelling, RIS, and phase changes also to be characterized using HTP methods, as well as covering a larger compositional space in this alloy system and others less explored.

5 High-Temperature Ion Irradiation and Localized Heating System

This chapter features direct content from the following journal article(s) first-authored by the PhD candidate:

M. Moorehead, B. Queylat, H. Zhang, K. Kriewaldt, A. Couet, **Development of a versatile, high-temperature, high-throughput ion irradiation system**, Nuclear Inst. and Methods in Physics Research, A (2021), *in press*.

5.1 Introduction and Motivation

While the stage developed and tested in the previous section is adequate for performing room-temperature ion irradiations, the final piece of the high-throughput irradiation puzzle is to be able to perform high-temperature irradiations. At room temperature, ion irradiation can induce phenomena such as radiation hardening, however, to observe void swelling, materials must be irradiated between temperatures near ~0.3-0.6T_m, which corresponds to ~250-750 °C for stainless steel and many other Cr-Fe-Mn-Ni alloys.

Heated ion irradiation of large-area materials is routinely performed within the semiconductor industry, where it is often desirable to anneal out radiation-induced defects and recrystallize material which can be amorphized under irradiation, as is the case for ion implantation in silicon wafers [206]. Under irradiation, substrate temperatures are dictated by the ion beam current applied and any water cooling or resistive heating applied uniformly to the back of the substrate [207]. However, for irradiation damage experiments, relying on the ion beam current to set the substrate temperature is often undesirable or infeasible, since the goal of many experiments is to decouple the microstructural response of a material under irradiation as a function of temperature *or* damage rate while all other parameters are held constant. Moreover, metallic samples or samples bombarded using heavy ions may not be capable of being heated to reactor-relevant temperatures with ion beam heating alone, given the maximum beam currents available at many accelerator facilities. Traditional resistive heating can also pose challenges for combinatorial sample arrays specifically

– if samples are being irradiated in series, heating would likely be applied to all samples simultaneously using a traditional resistive heater. This introduces the risk of annealing out the radiation-induced defects previously produced in a given sample. Thus, to maintain the greatest degree of both experimental flexibility and fidelity, it is desirable to be able to heat samples individually, while other samples remain cool to limit diffusion and annealing of defects.

In addition to heating samples individually, the ultimate objective is to automate all of the control systems necessary to irradiate samples in a high-throughput manner, to reduce the time needed to irradiate an entire array of samples and minimize user error. Ion beam current integration, sample temperature management, and stage control should be performed automatically and require minimal user input (if any) to switch between samples within a sample array. Such a control system would also need to include safety interlocks to prevent damage to the beamline or samples either by user action or during automated operation.

The following sections detail the design, development, and operation of the systems identified as necessary to perform high-throughput ion irradiations at elevated temperatures. Additionally, the newly developed high-temperature, high-throughput irradiation system has been used to perform first-of-a-kind ion irradiation experiments which enable the high-throughput assessment of void swelling in Cr-Fe-Mn-Ni-based HEAs and CCAs.

5.2 Localized Heating System

The methodology for locally heating individual samples is dependent on the sample material. For example, ceramics can be readily heated by controlling the ion beam current alone (or even cooling the sample stage with water or liquid/gaseous N2) since most ceramics have sufficiently low thermal conductivities to produce a large temperature difference (ΔT) between the sample surface and stage with only modest heat fluxes imparted by the ion beam [208]. For metallic samples however, a substantially

larger heat flux is necessary to bring the sample surface to temperatures representative of fission-based, or even fusion-based, nuclear reactors.

To produce sufficiently large heat fluxes to heat metallic samples, a 2-kW infrared (IR) Nd:YAG laser from AdNaNo-Tek is used. The IR laser is housed on the exterior of the vacuum chamber and can deliver nominally up to 2-kW of laser heating at a wavelength of 1064 nm as a columnated beam with a circular spot size approximately 15 mm in diameter through an IR-transparent ZnSe window. A laser in the near-IR spectrum was chosen specifically to minimize any hazard to operators (as compared to a powerful laser operating in the visible light spectrum) while still maintaining high absorption rates across most metals and alloys, with the exception of a few highly reflective metals in the near-IR spectrum (e.g., pure Au, Ag, and Cu) [209]. For large arrays of samples, it is infeasible to attach thermocouples to each sample to provide temperature measurements and complete the temperature feedback loop with the IR laser. Instead, a Japan Sensor FTKX-type optical pyrometer is used to remotely measure the temperature on the surface which is heated by the IR laser. To perform accurate temperature measurements, the emissivity, ϵ, of the heated material must be known. For common materials, tabulated emissivity values have been compiled [210], otherwise, the emissivity of a material can be determined by calibrating the optical pyrometer against a thermocouple attached to the sample when heated either in situ by the laser, or while using conventional methods (e.g., hot plate).

To minimize reflection of the IR laser off of the sample surface, the IR laser was positioned as close to the normal axis of the sample as feasible, given that this position is occupied by the ion beamline. Additionally, since the wavelength of the IR laser is within the measurement range of the optical pyrometer, it is necessary that the optical pyrometer and IR laser are positioned such that the primary reflected laser beam is not within the acceptance angle of the optical pyrometer, else erroneous measurements and damage to the optical pyrometer are possible. Figure 46 illustrates the positioning of the IR laser and optical pyrometer relative to the ion beam and sample stage. The vacuum ports used by the optical pyrometer and IR laser are symmetrical about the ion beam, ±15° in the azimuthal direction -on opposite sides- and 20° in

the polar direction -on the same side- from the ion beam, which prevents the primary reflected laser beam from impinging directly onto the optical pyrometer.

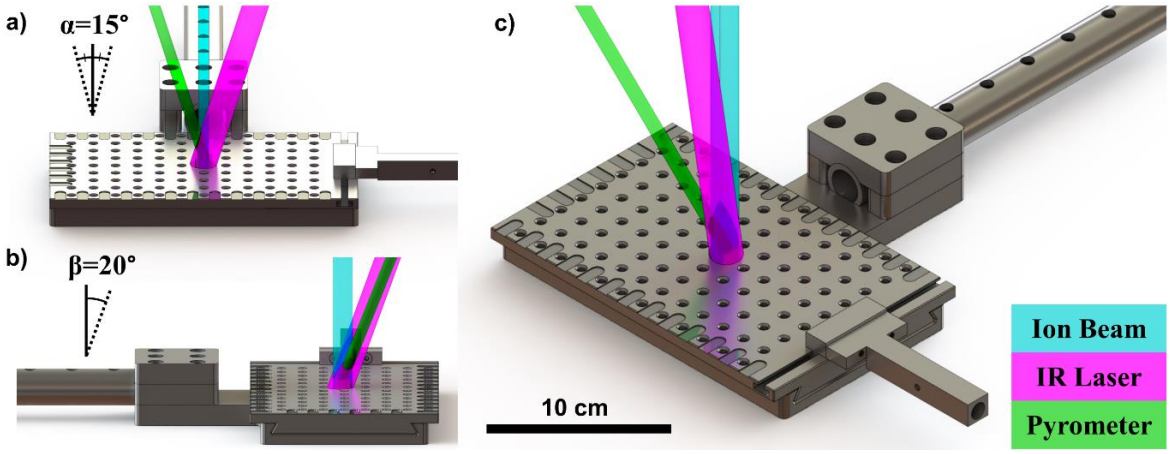

***Figure 46**: Illustration of the ion beam and IR laser impinging on a sample while the temperature is measured by the pyrometer. a), b), and c) offer different views of the triple-beam (ion beam, IR laser, pyrometer) condition, to show the orientation relationship between the beams. Note that the scale bar is only valid for view c).*

To test the localized heating capabilities of the IR laser system, a test sample array consisting of six cubes, 1 cm on a side and spaced 1 cm apart in a 3x2 pattern on a 2.5-mm-thick substrate, was machined from a single 12.7-mm-thick plate of 316 stainless steel by milling and polished using SiC paper to a mirror finish. In the first experiment, a single cube was heated using the IR laser to 500 °C, followed by a five-minute dwell, and cooled quickly by turning the IR laser off. The temperature measured by the optical pyrometer is read by a Eurotherm 2408 temperature controller which, using proportional-integral-derivative (PID) control, smoothly adjusts the IR laser power to maintain the desired temperature. Figure 47 shows the heating and cooling profile of the 316 stainless steel cube, as well as the IR laser power profile; note that 177 °C is the lowest temperature detectable by the optical pyrometer. Initially, there is a large spike in IR laser power to drive the sample temperature above the detectable threshold of the optical pyrometer, after which the power drops off and then steadily rises to ~60% over approximately 5 minutes to maintain a heating rate of 1 °C/s. Once within 5 °C of the target temperature, there is a sharp drop in IR laser power to prevent overshoot of the target temperature which is followed by a steady decline in IR laser power to

~40% over the five-minute dwell as the temperature gradient through the height of the cube equilibrates. After the dwell, the IR laser is turned off which causes an exponential decay in surface temperature back below the measurable temperature threshold over approximately 5 minutes.

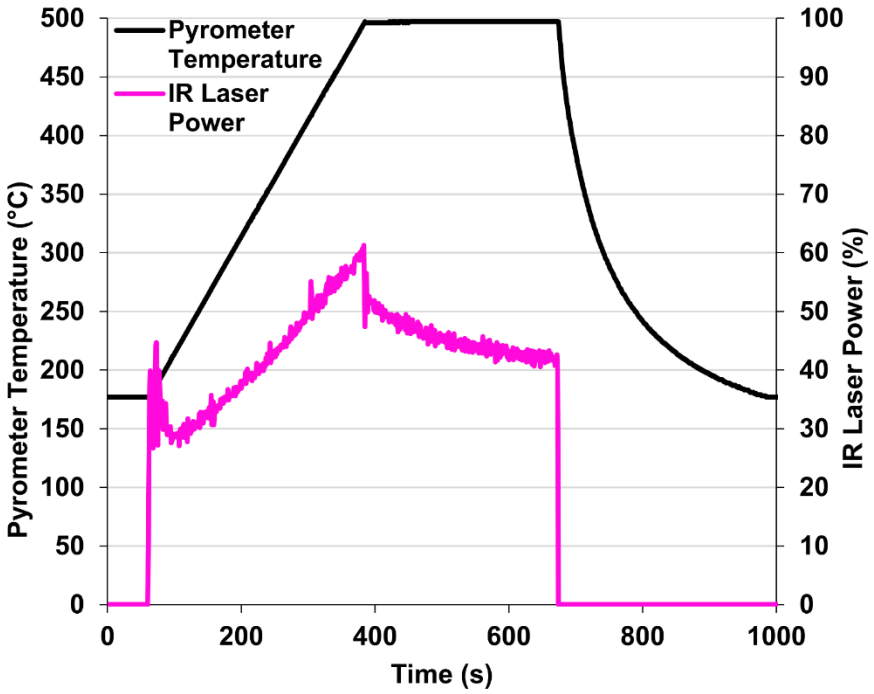

***Figure 47**: Temperature and IR laser power profiles of 1-cm^3 316-stainless-steel cube heated to 500 °C at 1 °C/s, followed by a five-minute dwell and then rapid cooling.*

Ensuring that ion-induced irradiation damage in previously irradiated samples is not annealed out during the irradiation of subsequent samples is paramount to the viability of high-temperature, high-throughput ion irradiation experiments. For most materials, diffusion of self-interstitial atoms (SIAs) can occur at or below room temperature, and in many materials individual vacancies can become mobile at temperatures <200 °C [24]. Given the relatively low temperatures necessary to activate these processes and the relatively high concentration of point defects generated by irradiation, it is infeasible to suppress SIA and vacancy diffusion in adjacent samples while one sample is heated to sufficiently high temperature as heat can be transferred between samples through the substate they share. Fortunately, dislocation-loop mobility in most materials <200 °C is sufficiently slow that, over the timescale of an ion irradiation

experiment (typically ≲1 minute/dpa for heavy ions), it is unlikely that measurable differences in microstructure or mechanical properties would be found as compared to a sample irradiated independently at elevated temperatures and allowed to cool gradually to room temperature. To illustrate these points, diffusion coefficients, migration energies, and diffusion lengths for SIAs, vacancies, and SIA loops are given in Table 5.1 using α-Fe (BCC) at 200 °C as an example. After 6000 seconds (the estimated time to irradiate a sample to 100 dpa using heavy ions), the 1D diffusion length of SIAs is nearly 1 mm while the diffusion length of vacancies is ~13 μm and the diffusion length of ½<111>-type SIA loops, approximately 8 nm in diameter, is only ~56 nm. However, at higher temperatures, other processes including vacancy cluster dissolution by vacancy emission, unfaulting of Frank loops, and the growth of dislocation loops and networks can be activated as part of the so-called stage IV recovery of irradiated materials, which can affect both the microstructure and mechanical properties [211, 212]. For reactor-relevant materials such as steels and Cr-Fe-Mn-Ni-based complex concentrated alloys (CCAs), onset of stage IV recovery has been estimated to occur between 400-500 °C [169, 170, 213]. Thus, for arrays of Cr-Fe-Mn-Ni-type alloys, 400-500 °C serves as an upper bound for the temperature that irradiated samples in a sample array can safely remain at after they have been irradiated, without appreciably altering the microstructure and properties by thermal annealing.

Table 5.1*: Irradiation defect diffusion lengths in α-Fe (BCC) over 6000 seconds (the estimated time to irradiate a sample to 100 dpa using heavy ions), calculated at 200 °C using diffusion coefficients and activation energies from literature. X=2*sqrt(D*t) was used to estimate the 1D diffusion length. An SIA loop consisting of 1000 atoms, corresponding to a loop diameter of ~8 nm, was used for reference.*

Defect	**Diffusion Coefficient Pre-Exponent D_0 [m^2/s]**	**Migration Energy [eV]**	**Diffusion Length [m]**	**Reference**
SIA	6.02E-8	0.3	9.59E-04	[214]
Vacancy	6.02E-8	0.65	1.31E-05	[214]
½ <111>-type SIA Loop	9.16E-6	1.3	5.56E-08	[215]

To approximate the maximum viable irradiation temperature of Cr-Fe-Mn-Ni-type alloys, which constitute the majority of structural components within a nuclear reactor, a cube in the middle of the six-cube 316-stainless-steel array was heated to 800 °C by operating the IR laser near the maximum of its continuous safe operation power of 85% (1700 W). After a five-minute dwell at 800 °C, the IR laser was turned off and the stage was quickly repositioned to measure the temperature of an adjacent cube which was found to be ~425 °C (and decreasing). Figure 48 shows a photograph of the entire stage with the heated sample while Figure 49 shows photographs taken at each step of the 800-°C heating experiment from inside the vacuum chamber. In Figure 49b, the spot size of the IR laser is shown by operating the IR laser below <1% power which appears purple when viewed using a webcam with a CMOS sensor capable of capturing both visible and near-IR light. Here, the IR laser spot can be seen covering one sample cube in its entirety without touching the surrounding cubes. Note that while the cross section of the IR laser beam is circular, the projected spot more closely resembles an ellipse due to the angle of the incident beam relative to the normal axis of the sample (illustrated in Figure 46). At higher laser powers, the camera inside the vacuum chamber becomes saturated (Figure 49c). Immediately after the IR laser is turned off, the incandescence of the sample cube heated to 800 °C is visible while the adjacent sample cubes appear the same as before heating – corroborating the pyrometer temperature measurements of both the heated and unheated samples.

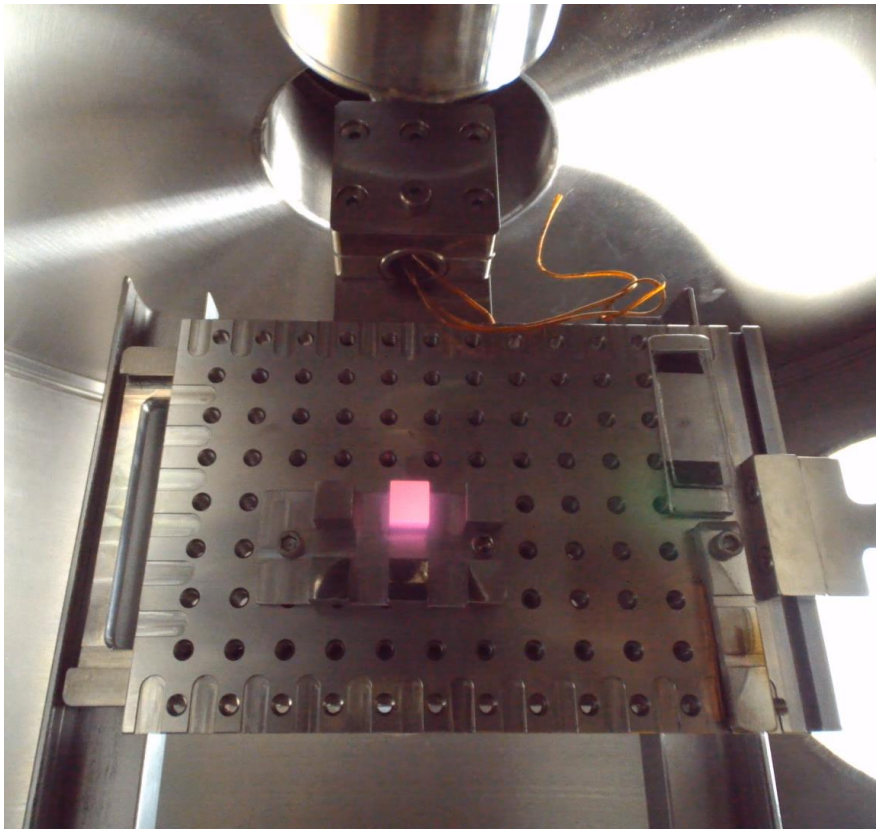

***Figure 48**: Photograph of sample cube in 1-cm^3 316-stainless stee-cube array heated to 800 °C without directly heating surrounding samples.*

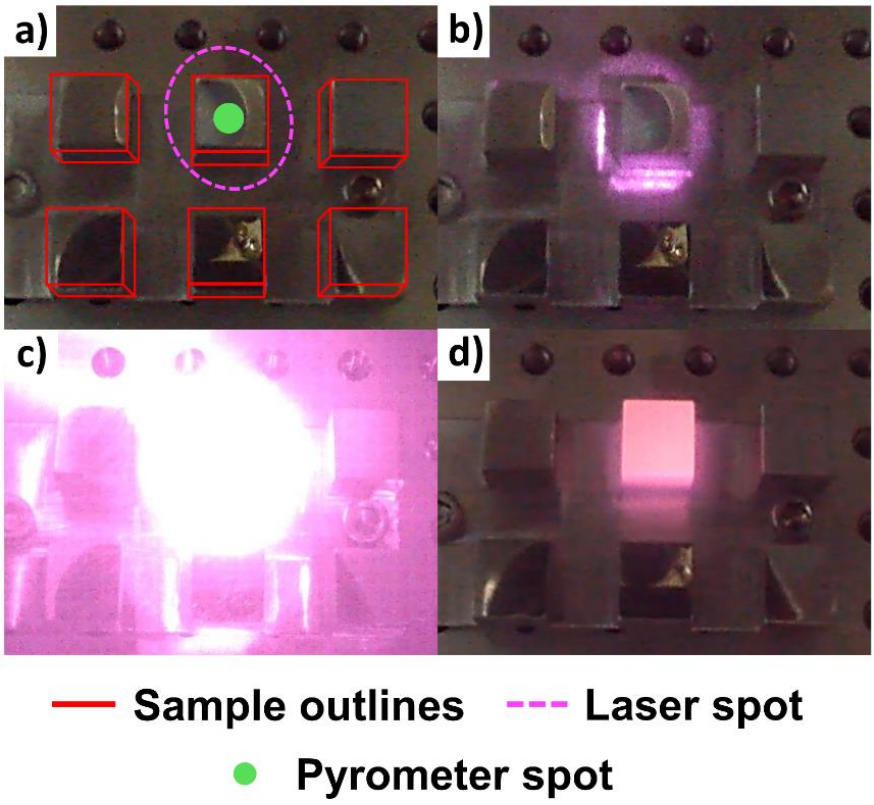

***Figure 49**: 800-°C heating experiment of 1-cm^3 316-stainless stee-cube array as shown a) before heating with annotations clarifying cube, IR laser, and pyrometer positions; b) while operating at <1% power to show IR laser spot size (purple) and optical pyrometer pilot light (faint green); c) while operating at 85% IR laser power; d) immediately after IR laser was turned off, highlighting the incandescent heated cube surrounded by (relatively) cooler cubes.*

The results from the 800-°C heating experiment demonstrate that in the case of 316 stainless steel and the sample geometry used above, ion irradiations should be able to be performed up to ~750 °C without major concern of annealing adjacent samples during subsequent irradiations. For reference, 750 °C is above the maximum operating temperature of nearly all advanced reactor designs, except for the most ambitious high-temperature gas reactor and fusion concepts [35]. Changes to the sample array geometry, including wider sample spacing and taller sample heights, could be invoked to perform high-throughput ion irradiations at higher irradiation temperatures and higher temperature differences between samples more suitable to specific irradiation requirements.

5.3 Automated Control Program

While performing ion irradiations on arrays of samples already saves a substantial amount of time lost to sample transfers, chamber evacuations, and sample heating/cooling, there are still time savings to be gained by automating the control of the irradiation setup and execution. Specifically, stage positioning, IR laser control, temperature monitoring, current measurement, fluence integration, and data logging are all mechanical/repetitive tasks that need not have human involvement. To realize this, the program dubbed "Chronos", the personification of time in Greek mythology, was developed using LabVIEW 2020 – a screenshot of which is shown in Figure 50. The program communicates with beamline devices using ethernet, RS-232, and RS-485 serial communication lines to communicate using different protocols (e.g., Modbus, SCPI 1996.0) and uses a National Instruments cDAQ-9189 to send and receive analog signals as well as take thermocouple readings. To setup an irradiation, users need only provide a list of sample positions, irradiation temperatures, and desired fluences, after which Chronos can perform the desired irradiation experiment without further user interaction. Irradiation execution is preceded by a full system self-test, whereby the program sends test signals to all connected devices to ensure communications are behaving properly. For the next part of the self-test, the program actuates the Faraday cup (which serves to block the ion beam and measure the beam current) in and out, moves the stage back and forth ±10 mm in both the X and Y directions to ensure stepper motors are operational and stage is able to move freely, and (if temperature control is enabled) powers the IR laser and heats the target area to 200 °C to ensure proper operation of both the IR laser and the pyrometer. If the self-test is passed without any devices sending alarm signals, any interlocks tripped, or any limit switches reached, the irradiation proceeds. With the Faraday cup blocking the ion beam, Chronos begins the irradiation by positioning stage such that the first sample is aligned at the triple beam condition, where the ion beam, IR laser, and optical pyrometer coincide. The sample is then driven to the target temperature using the IR laser and once the sample temperature is within 15 °C of the target temperature, the Faraday cup is actuated out and the sample is exposed to the ion beam. Using the ion beam current measured during the initial sample heating, Chronos will calculate the expected

irradiation time and reinsert the Faraday cup at regular intervals to monitor the beam current which is used to calculate the fluence delivered and the time remaining. After a single irradiation is completed, the Faraday cup is inserted to block the beam, the IR laser is turned off, and (depending on initial program configuration) the program will either wait for a user signal to proceed or automatically proceed to the next sample. Following each irradiation, the temperature history, IR laser power history, and beam current history are automatically output to a .csv file along with the minimum/maximum/average temperature, beam current, beam flux, and final fluence. Additionally, if SRIM was used to calculate the dpa profile beforehand and a phonon.txt was provided [216], Chronos will output minimum/maximum/average peak dpa, plateau dpa, peak dpa rate, and plateau dpa rate. Example output tables from a previous 4-MeV Ni^{2+} irradiation of pure Fe, to a peak damage of 200 dpa at 500 °C and performed using Chronos, are provided in the Appendix (Table 7.3 and Table 7.4); for brevity, the >5600 pyrometer temperature and IR laser power measurements are omitted.

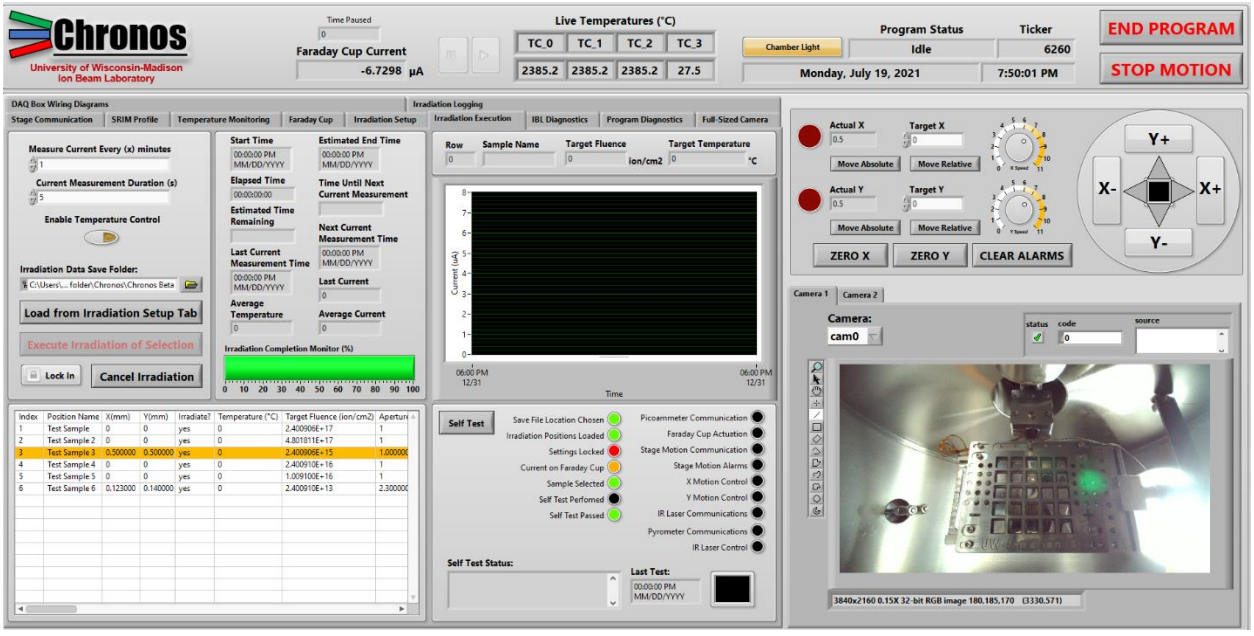

***Figure 50**: "Chronos", an automated high-throughput ion irradiation program developed using LabVIEW 2020 and implemented at the University of Wisconsin-Madison Ion Beam Laboratory (IBL).*

To ensure both the integrity of the irradiation experiments and the safety of the beamline, several interlocks and safety mechanisms have been incorporated in addition to the initial self-test performed before

an irradiation. Firstly, at any point during the irradiation, the user has the ability to pause or cancel the irradiation as well as end the program as part of an emergency stop mechanism. When paused, the Faraday cup is inserted to block the ion beam and the pause timestamp and duration is recorded automatically such that average fluxes, currents, etc. can properly calculated after the irradiation, regardless of the number or duration of interruptions. In the case of canceling an irradiation, the Faraday cup is inserted for a final current measurement, the IR laser is turned off, and the .csv irradiation log is output. In the case of ending the program, the Faraday cup is inserted and without waiting for a current measurement, all controlled devices are shut down immediately. During automated irradiation, several engineering safety mechanisms are being verified constantly. For example, if at any point during the irradiation the sample temperature deviates from the target temperature by more than ±15 °C for 30 seconds or longer, Chronos will automatically pause the irradiation and wait until the temperature returns to the valid range before restarting; this serves to preserve the integrity of the irradiated sample in the case that the IR laser shuts down prematurely, for example, by tripping a cooling water temperature interlock or if a circuit breaker is tripped within the lab space. Similarly, if the program encounters a communication error with the stepper motor drives during irradiation, it will attempt to refresh and reestablish the connection and if unsuccessful, the program will not proceed in attempting to irradiate additional samples.

5.4 High-Temperature, High-Throughput Ion Irradiation Experiment

With installation of the localized heating system and integration with the automated control program, Chronos, completed, the final validation step is to perform a high-temperature, high-throughput ion irradiation experiment. The goal would be to characterize the samples afterwards to verify that irradiation phenomena only producible at elevated temperatures, namely void swelling, have been produced and that the results are in agreement with data from literature; ideally, such characterization would also be performed in a high-throughput fashion as well. At the time of writing, many different high-temperature ion irradiations under different experimental conditions have been performed at the University of Wisconsin-Madison Ion Beam Laboratory (IBL) using the high-throughput irradiation systems described in the

previous sections, which have produced well over 100 different irradiated samples over the span of eight months. During this time, improvements have been made to the stage motion system (e.g., adding guiderail, reinforcing the hook mechanism), the localized heating system (e.g., installing a larger window for the pyrometer, improving pyrometer alignment fixture), and Chronos (e.g., scheduled memory deallocation, more accurate beam current integration, quality-of-life improvements), all of which have improved the speed, precision, fidelity, and reliability of the high-throughput irradiation system. For the sake of concision, the following section details the most recent high-temperature, high-throughput irradiation experiment as it is the most representative of the current state of the high-throughput irradiation system installed at the IBL.

5.4.1 Methods and Materials

To fully validate the high-temperature capabilities of the high-throughput ion irradiation system, whose development has been detailed over the last two chapters, a compositional array of 25 Cr-Fe-Mn-Ni alloys was produced by in situ alloying via additive manufacturing using an Optomec LENS MR-7 following the same procedure described in section 4.3. Sample target compositions were selected to span the range of the FCC phase field of the Cr-Fe-Mn-Ni system at 500 °C which was determined from CALPHAD calculations using the Pandat software equipped with the PanHEA database, illustrated previously in Figure 31. After synthesis, the additively manufactured compositional array was subjected to a homogenization heat treatment at 1000 °C for 48 hours in high vacuum (~1E-6 torr) to remove any microchemical segregation resulting from cooling from the liquid state during additive manufacturing. The samples in the compositional array were then machined to the same height from the back of the build plate using wire electrical discharge machining (EDM). The entire compositional array was mechanically polished progressively from 120 through 1200 SiC grit papers, followed by polishing with 3-μm and 1-μm diamond suspensions to produce the surface finish required for ion irradiation in accordance with ASTM E521-96 [194]. The traditional final polishing step using 0.04-μm colloidal silica was forgone to prevent

preferential etching of the grains. After polishing, sample compositions were measured via XRF using a SciAps X-200 series XRF detector which are shown in Table 7.5 in the Appendix.

The additively manufactured sample array was clamped onto the stainless stage system, described in detail in section 4.2, which is installed on the middle beamline of the UW-Madison IBL. A K-type thermocouple was placed in contact with the sample surface of one sample on the top row of the sample array and a molybdenum mask was affixed over the sample array, shown in Figure 51. The Mo mask serves two purposes: first, to mask a portion of each sample from the impinging ion beam during irradiation to produce a sharp irradiated/unirradiated interface, and second, to shield the thermocouple used for pyrometer calibration from the IR laser – since the thermocouple is unable to reject heat as efficiently as the samples, which are effectively welded to a large heat sink, the thermocouple is heated preferentially under the IR laser which can compromise the pyrometer calibration process. With the Mo mask and thermocouple in position, the pyrometer and IR laser were positioned such that they were coincident on the center of the unmasked surface of the sample with the thermocouple attached. By adjusting the IR laser power until thermocouple read 500 °C (the irradiation temperature) and stabilized, the emissivity of the sample was calculated, and the pyrometer was calibrated such that it read the same temperature as the thermocouple. For the sample with the thermocouple attached (Sample 3 in this case), the emissivity was found to be 0.267. Since all samples in the sample array are Cr-Fe-Mn-Ni based alloys which have been synthesized and mechanically polished under the same conditions, and since attaching a thermocouple to each sample in the vacuum chamber is intractable, differences in emissivities between the samples were assumed to be negligible. Sample positions were input into the Chronos program by the user along with the desired irradiation temperature (500 °C) and desired fluence (2.04E17 ions/cm^2, corresponding to a peak damage of 200 dpa via SRIM calculated using the same procedure in section 4.3), after which the irradiation was performed automatically using 4-MeV Ni^{2+} ions, only pausing optionally between samples to await a user confirmation as an added safety precaution. The entire ion irradiation campaign for the 25 samples was completed in less than 40 hours.

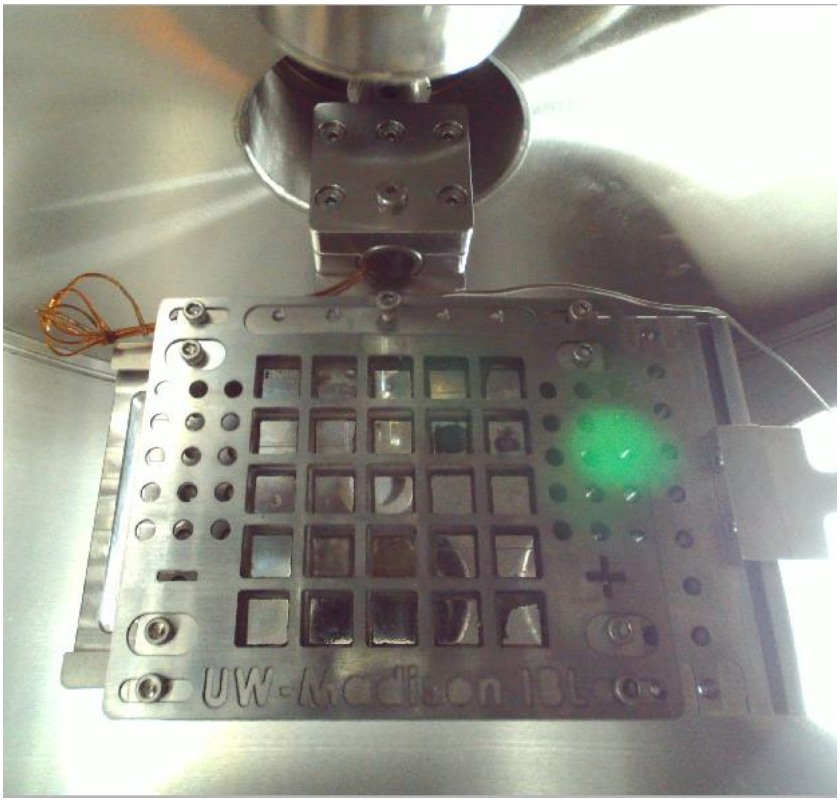

Figure 51*: Cr-Fe-Mn-Ni additively manufactured sample array loaded in the IBL middle beamline vacuum chamber with Mo mask and thermocouple attached.*

Following irradiation of every sample in the array, X-ray diffraction (XRD) was performed on the irradiated and unirradiated areas of each sample, using a Bruker D8 Discover X-ray diffractometer, to probe whether the ion irradiation had produced any significant phase changes in the materials. To assess the presence of void swelling, optical profilometry was performed using a Zygo NewView 9000 to map the variation in height between the unirradiated and irradiated regions of each sample. From the height map of each sample, the average height of the unirradiated and irradiated regions was determined by averaging over an area of 100 x 100 μm in each region and subtracting the unirradiated height from the irradiated height to calculate the average step height. Error in the step height value was calculated by standard error propagation using the average heights and standard deviations in height from each region.

5.4.2 Results

The phases identified in the irradiated and unirradiated region of each sample are given in Table 7.5 in the Appendix. The XRD analysis indicated that 22 of the 25 samples exhibited single-phase FCC crystal structures both with and without irradiation given the same thermal history (i.e., 48 hours at 1000 °C, followed by ~1.5 hours at 500 °C during irradiation). The three samples with the highest Fe contents (>78 at%) exhibited single-phase BCC crystal structures in the unirradiated regions, but two of these three samples, sample #2 and sample #6, were found to have FCC+BCC crystal structures in the irradiated condition. Since all of the samples were irradiated to a high dose using Ni^{2+} ions, it is unclear whether this difference in measured phases in the unirradiated and irradiated regions is caused by irradiation enhanced diffusion or is simply the result of injecting a non-negligible concentration of Ni atoms which can stabilize the FCC crystal structure. Also of interest is the fact that the unirradiated regions of sample #2 and sample #6, with Ni contents of 19.0 at% and 11.7 at%, respectively, were found to only exhibit a BCC crystal structure when compositions with such high Ni contents would be expected to exhibit a non-zero fraction of an FCC phase, based on previous CALPHAD calculations. It is possible that these low-alloying-content compositions undergo more rapid grain growth during the two-day, 1000 °C heat treatment which produces very large grains and decreases the number of grains sampled during XRD, but further microstructural characterization (namely microscopy) would be needed to confirm this.

Figure 52 shows a representative optical image and height map acquired from optical profilometry, in this case from sample #18. Here, the stark contrast can be seen between the irradiated region (left) and the unirradiated region (right), where the irradiated region appears much darker with the underlying grain structure visible. While the interface is jagged, owing to the water-jetted surface finish of the Mo mask, there is a steep change in height at the interface of more than 100 nm between the unirradiated and irradiated regions. The height map also indicates that individual grains in the irradiated region are at different heights, which contributes to the contrast seen in the optical image. Since grains in the unirradiated region are not seen with such contrast, the difference in height of the grains in the irradiated region is attributable to the

irradiation itself. Though the difference in height between the grains is likely due to differences in grain orientation, microstructural characterization (namely TEM) would be needed to determine if the height difference is due to preferential sputtering of the material under irradiation or changes in ion implantation depth and swelling behavior based on the grain orientation, as may be caused by ion channeling [217, 218].

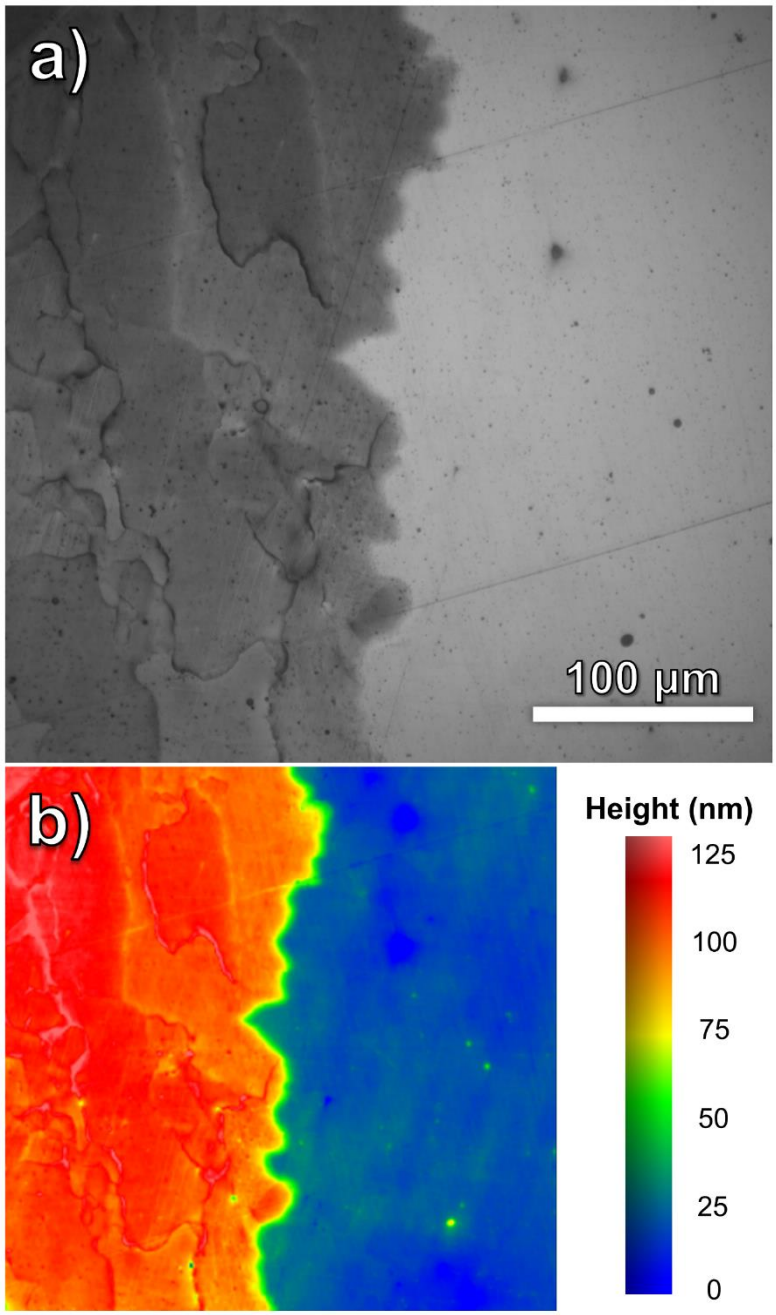

***Figure 52**: a) optical image and b) height map of sample #18 from optical profilometry.*

To further examine the irradiated/unirradiated interface, Figure 53 provides a 3D visualization of the step change in height between the two regions, in this case for sample #21. In addition to the differences in heights between grains in the irradiated region, small spikes can be in both regions and appear to decorate the grain boundaries as well as appear within the interior of some grains. Since single "hot" pixels have already been removed during the processing of the profilometry data, these spikes appear to be physical, and based on their distribution in both regions and along grain boundaries it is suspected that these are small oxide crystallites which have started to form while heated during the irradiation experiment. While the ion irradiation is performed in ultra-high vacuum (~10^{-7} torr), it is impossible to eliminate all of the oxygen within the vacuum chamber, and such oxide crystallites have been observed in previous unpublished studies of Cr-Fe-Mn-Ni alloys under irradiation at UW-Madison when studied using TEM.

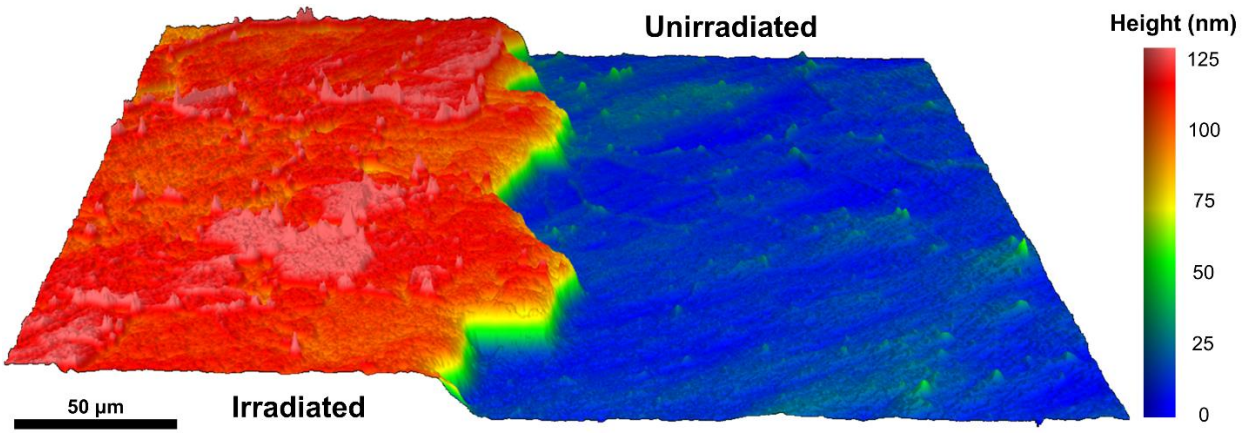

***Figure 53**: 3D visualization of sample #21 height map from optical profilometry. Height has been visually exaggerated by a factor of 10 for clarity.*

To calculate the apparent radiation-induced void swelling of each sample, the step height was divided by the estimated radiation-damage layer thickness, which was approximately 1.8 µm based on the SRIM profile in Figure 38, which is a simplification of the procedure given in ref [219] that yields an average void swelling value for the entire irradiated volume rather than a depth-resolved swelling which would require TEM characterization to deduce. To evaluate the compositional dependence of the void swelling across all of the samples in the array, the step height and calculated swelling percent were plotted as a function of each constituent element, shown in Figure 54. For the two minor alloying elements, Cr and

Mn, a positive correlation is observable resulting in increasing swelling with increasing Cr and Mn content, though the trend with Mn is much weaker than Cr. For the major alloying components, Fe and Ni, no definitive trend in swelling is observable as a function of Fe content, however, there is a strong negative correlation between Ni content and swelling starting at ~25-30 at% and continuing towards pure Ni. As is often the challenge with large multi-variable datasets, it is difficult to visualize the multidimensional relationships from the dataset, let alone collapse it to two dimensions on paper. In an attempt to conceptualize these results, Figure 55 shows the step height measurements for each sample plotted against the two elements which independently showed the strongest void swelling dependencies, Cr and Ni, and both raw data and as an alpha hull. Here, the contour of the step height data can be better captured where the step height measurements are seen to increase sharply with low Ni and high Cr content, while in the absence of Cr, changes to the Ni content have little impact on the step height measured. Additionally, from this plot, since any given X-Y (i.e., Cr-Ni) coordinate is not a unique composition, the thickness of the alpha hull in the step height direction illustrates the range of swelling behavior that can be produced by changing the relative Fe and Mn contents while the Cr and Ni contents are held constant.

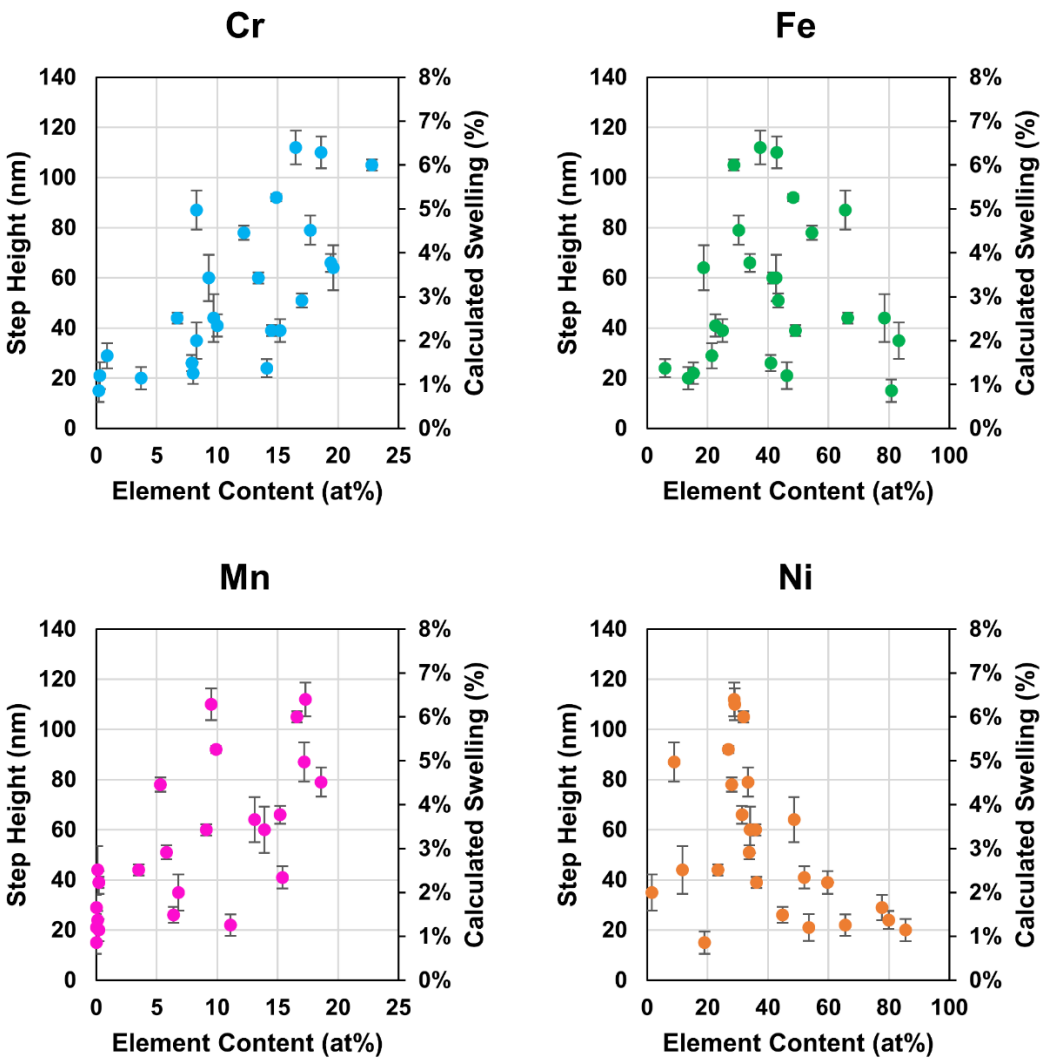

***Figure 54**: Measured step height and calculated swelling as a function of composition.*

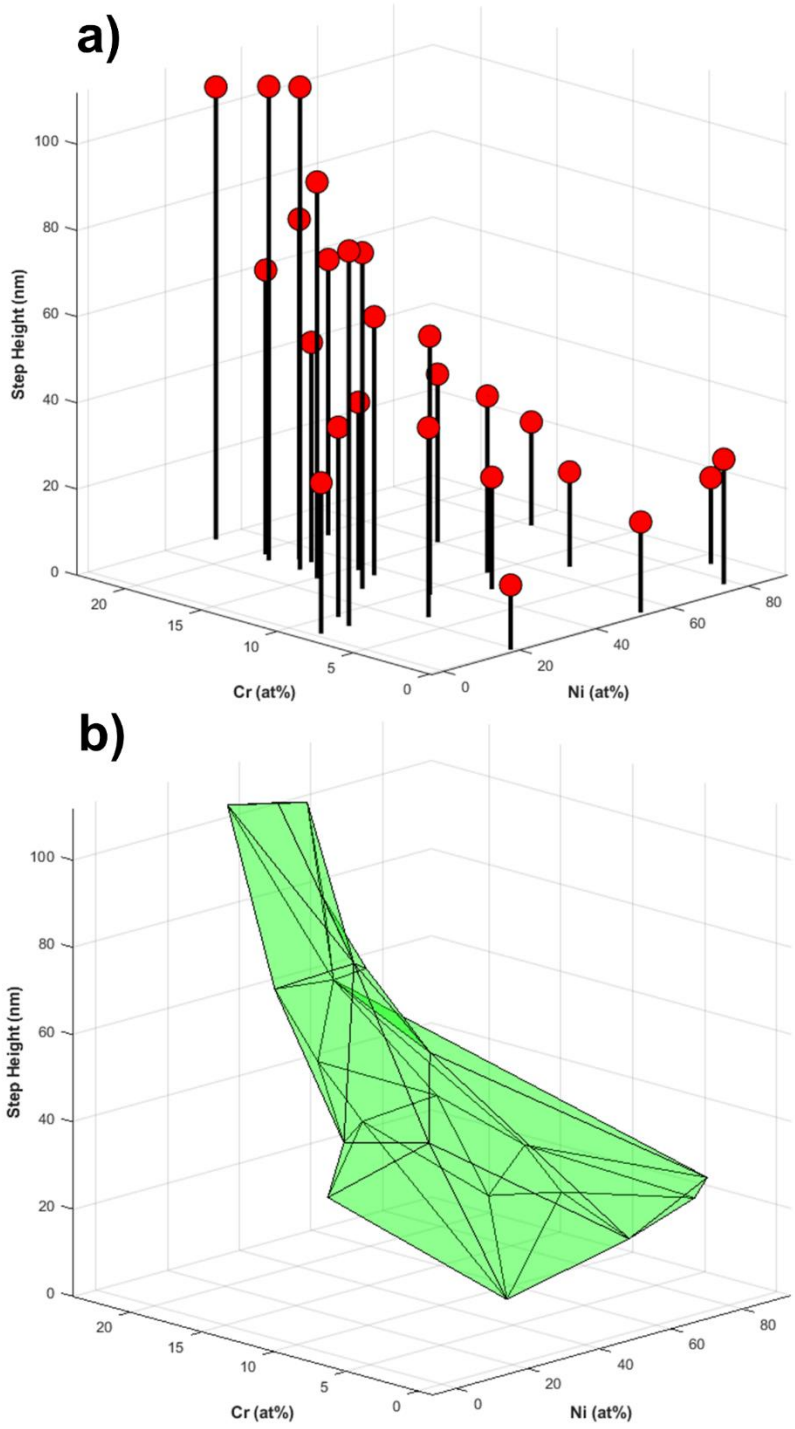

Figure 55*: Step height measurements for irradiated samples plotted against Cr and Ni content as a) raw data and b) as an alpha hull.*

Since high-throughput ion irradiation experiments are novel and feature substantially different heating and control systems than traditional ion irradiation experiments, it is important to validate that the process produces results similar previous experiments. To qualitatively examine this, Figure 56 illustrates

the swelling behavior of several Cr-Fe-Ni alloys irradiated using 5-MeV ions at 675 °C by Johnston et al. in 1974 [220]. While the 1974 was performed at higher temperatures and they alloys used did not contain Mn (which was shown to only weaking influence swelling behavior above), the same trends pertaining to Cr and Ni are observed in the 1974 study as in the recent high-throughput ion irradiation study presented herein. Swelling is seen to monotonically increase with increasing Cr content while decrease with increasing Ni content; additionally, the low-Cr alloys show little swelling at all and a minimal dependence on Ni content. Overall, the trends in the data from the 1974 study in Figure 56 bear a striking resemblance to the trends in the data from the current study presented in Figure 55, which supports the validity of the new high-throughput ion irradiation system and methodology.

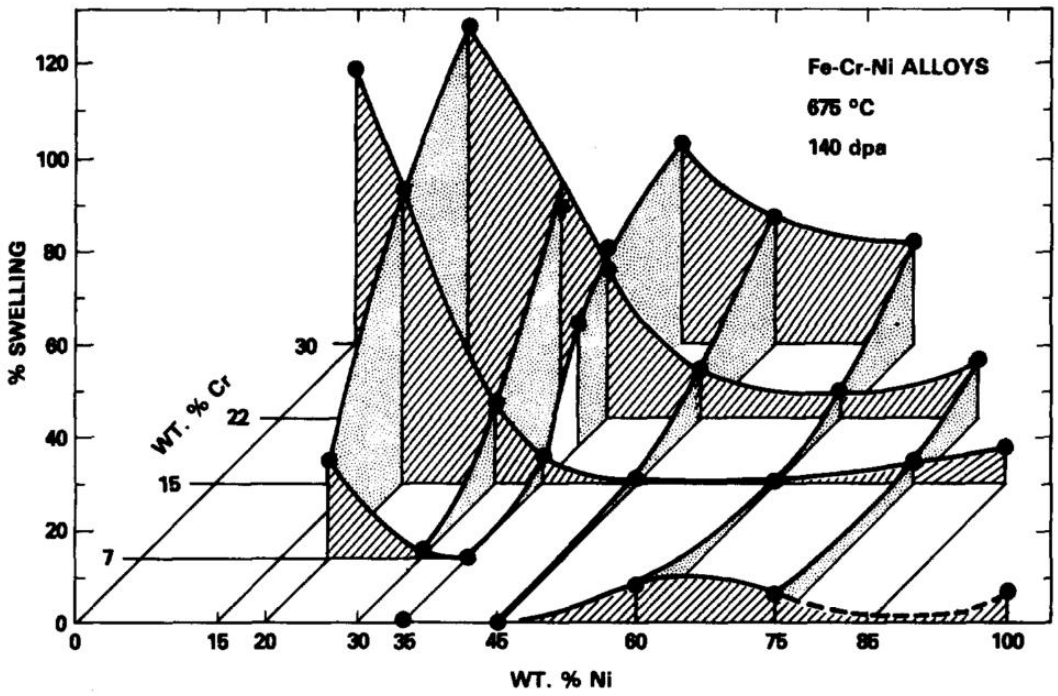

Figure 56*: Swelling behavior of several Cr-Fe-Ni alloys after 5-MeV Ni ion irradiation at 675 °C. Data from [220], figure adapted from [29].*

5.5 Discussion

The primary goal of implementing the high-throughput techniques presented herein, in essence, is to increase the number of ion irradiation experiments that can be performed in a single day. Presently, university-scale accelerator facilities can reliably produce ~1-5 μA of heavy-ion beam current which,

depending on ion energy and the sample material, can produce damage rates on the order of 1E-2 dpa/s. At such damage rates, samples can be subjected to >100 dpa in ~2-3 hours, conservatively. While this would imply that several irradiation experiments could be performed in a single day, in practice, irradiation experiments are often limited to one per day given the time required to exchange samples, bring the accelerator online, heat the samples, irradiate the samples, cool the samples, and finally bring the accelerator offline at the end of the day. By comparison, utilizing the stage and localized (IR laser) heating system above, the time to switch between samples mounted to the stage is reduced to seconds while heating a specific sample to the desired temperature can be achieved in minutes thereby enabling multiple irradiation experiments to occur within a workday. Moreover, utilizing the automated capabilities of the Chronos program, outfitted with passive safety features and monitoring, irradiation experiments can be safely run with little to no human supervision, thereby enabling the accelerator to be operated 24 hours a day as needed. The combination of reduced sample exchange time and the ability to operate the accelerator during extended hours results in nearly an order of magnitude time savings for performing a series of irradiation experiments, as has been demonstrated using a predecessor to the high-throughput irradiation system installed at the University of Wisconsin-Madison Ion Beam Laboratory [221].

Chronos was developed expressly with the intent of minimizing unnecessary user interaction for setting up and executing ion irradiation experiments. Besides providing time savings, the simplification of the otherwise arcane accelerator operation, ion irradiation setup, and ion irradiation execution process also lowers the barrier to entry for training new users to perform ion irradiation experiments. As the University of Wisconsin-Madison Ion Beam Laboratory is a part of the Nuclear Science User Facilities (NSUF) network, the implementation of Chronos opens up the possibility for outside users to be trained to perform their own customizable ion irradiation experiments. Additionally, once samples are loaded, remote access can be enabled to allow users to monitor and control their experiments from their home facility, if desired, thus improving the versatility and reducing the costs associated with performing ion irradiation experiments.

In addition to time savings for traditional irradiation experiments, the implementation of automated stage motion and localized temperature control also enables new types of high-throughput irradiation experiments. Such experiments could be used to rapidly generate swelling curves (i.e., void swelling % vs. irradiation dose and void swelling % vs. irradiation temperature) to be able to more thoroughly compare the irradiation response of different materials, as materials will have different incubation doses and different swelling-temperature profiles, the nuance of which is not captured by a single experimental data point. Typically, generating swelling-curve datasets has been reserved later in the alloy development process, due to the time and cost associated with performing a large battery of experiment. However, high-throughput irradiation experiments may enable swelling-curve data to be generated earlier as part of the materials discovery process, to allow for more informed down-selection and potentially discover new trends that would otherwise be missed if comprehensive irradiation experiments are reserved for later in the alloy development process. To demonstrate how this could be achieved, Figure 57 illustrates two possible high-throughput irradiation experiments made possible with this unique equipment. In Figure 57a, one end of the sample material is heated with the IR laser to the desired irradiation temperature. Once the ion irradiation commences (by actuating the Faraday cup), the stage begins to slowly move in the Y direction and accelerates. Since the stepper motor controlling motion in the Y direction uses a 50:1 geared torque multiplier, the velocity in the Y direction can be maintained at very slow speeds and precisely adjusted. As the sample material moves beneath the IR laser and ion beam spots, the PID controlling the IR laser maintains a constant irradiation temperature while the dwell time of the beam (and thus the dose) at any given point on the sample gradually decreases. The end result is a sample with a gradient of irradiation damage (i.e., dpa) from one end to the other, irradiated at constant temperature and dpa rate. Such an experiment could be used to examine the effects of different irradiation doses for a given sample material with all other parameters kept constant, and, for instance, be used to determine the incubation dose of a material before the onset of void swelling. In a similar fashion, Figure 57b illustrates a high-throughput irradiation experiment in which the stage velocity is held constant while the irradiation temperature is varied. Here, once the irradiation commences, the stage is moved at a constant velocity which along with

the ion beam spot size and flux determines the dose at any given location on the sample. As the sample is traversed by the ion beam and IR laser, Chronos commands the PID controller to gradually increase the irradiation temperature. The end result in this case is a sample with a gradient of irradiation temperature across the surface with a constant dose and dose rate at every point on the sample. Such an experiment could be used, among other things, to determine the peak void swelling temperature for a given material and dose rate. Additionally, if the annealing of irradiation damage becomes a major concern, such experiments could just as easily be performed on a row of discrete samples which would improve the thermal isolation.

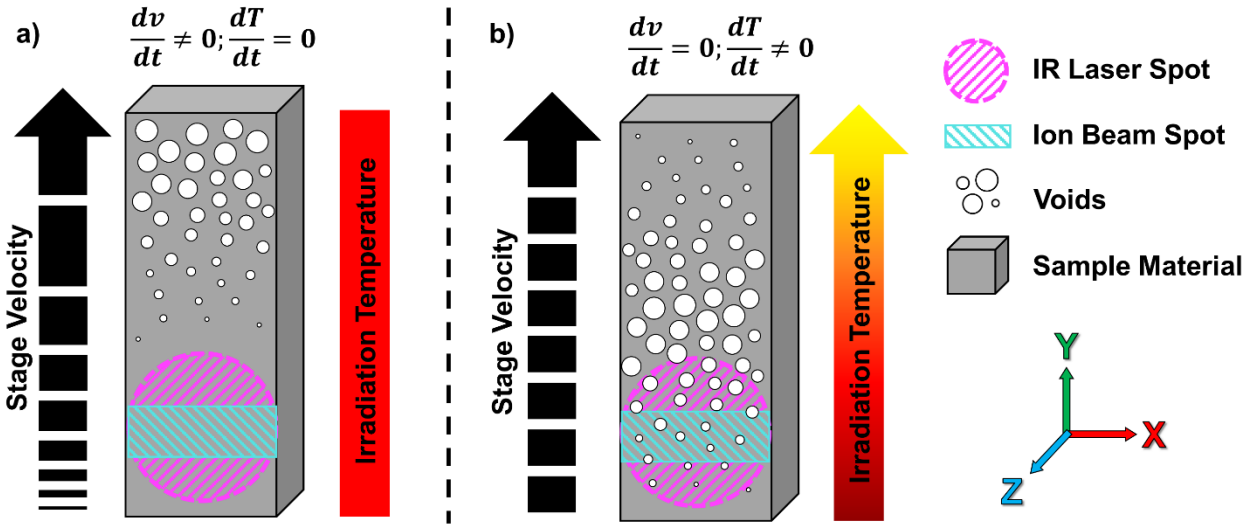

***Figure 57**: Potential high-throughput irradiation experiments made possible with stage motion, localized heating, and automated control. a) IR laser maintains constant irradiation temperature while stage is moved progressively faster to produce a damage (dpa) gradient. b) Stage is moved at a constant velocity while irradiation temperature is gradually increased to produce an irradiation temperature gradient with uniform irradiation damage.*

As with all new techniques, experimental validation is crucial, and by comparing trends in the swelling data from the irradiated Cr-Fe-Mn-Ni sample array to the Johnston Cr-Fe-Ni study from 1974 (i.e., Figure 55 vs. Figure 56), the high-throughput ion irradiation system and methodology appear promising, especially given that a similar number of samples were irradiated and examined in a few days versus what was likely well over a month. While additional validation tests are always desirable and improvements can still be made to the system, it is already possible to begin exploring some of the HEA and CCA composition spaces. So far, dozens of Cr-Fe-Mn-Ni alloy compositions have been irradiated at high-temperature using

the high-throughput ion irradiation system and trends are already observable in the data collect. For example, Figure 58 shows the step height measurements from every Cr-Fe-Mn-Ni alloy irradiated at high-temperature using the high-throughput ion irradiation system installed at the UW-Madison IBL to date; all experiments were to a peak dose of 200 dpa, at 500 °C, using 4-MeV Ni^{2+} ions. Contrary to what might appear to be conventional wisdom from literature, some of the most pronounced swelling behavior appears to occur in alloys near the center of the composition space. There are many possible reasons for this trend including differences in intrinsic properties such as the melting temperatures of the different alloys (likely leading to a higher homologous irradiation temperature near the center of the composition space), differences in vacancy and interstitial coefficients, and differences in thermal conductivity. Additionally, there are a number of microstructural features that could be playing a role such as grain size, oxide inclusions (from the additive manufacturing process), and phase distributions and morphologies. Unfortunately, many of these properties and features are not as rapidly measurable and identifiable without using comparatively slower characterization techniques – or at least, techniques that have not been adapted for high-throughput processing.

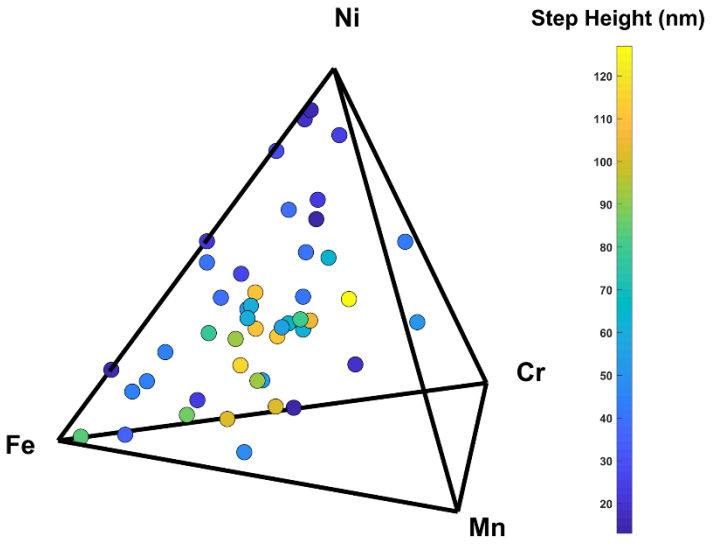

***Figure 58**: Step height measurements from every Cr-Fe-Mn-Ni alloy irradiated at high-temperature using the high-throughput ion irradiation system installed at the UW-Madison IBL to date. All experiments were to a peak dose of 200 dpa, at 500 °C, using 4-MeV Ni^{2+} ions.*

Whether viewed as unsatisfying or motivating, the question of why some HEAs and CCAs are more tolerant to irradiation damage than others still remains unanswered, and will be the subject of years of research and millions of dollars in research grants to come. However, in this pursuit, researchers now have a new set of tools and a proven methodology for being able to rapidly generate experimental data capturing the behavior of many different alloys under irradiation. Such large datasets not only help to accelerate existing analytical techniques and modeling, but also enable the employment of modern machine learning techniques which can find trends and dependencies not easily discerned by humans but require expansive datasets to be trained on and learn from.

5.6 Conclusions and Future Work

In summary, to ensure ion irradiation facilities are able to accommodate the growing use of large sample arrays produced using combinatorial and high-throughput synthesis techniques, a new high-throughput ion irradiation system was developed. By developing a custom stainless-steel stage system and coupling it with a 2-kW infrared (IR) laser, individual metallic samples can be heated to high temperatures (>800 °C) while adjacent samples remain cool enough to avoid appreciable annealing of extended irradiation defects. Stage motion, IR laser power control, temperature monitoring, and Faraday cup actuation are all controlled by a centralized program dubbed “Chronos” developed using LabVIEW, which enables the complete automation of ion irradiation experiments. By accommodating large sample arrays and performing high-throughput ion irradiation experiments, the time required to perform a series of ion irradiation experiments can be reduced by over an order of magnitude. Additionally, with precise stage motion and temperature control, new types of high-throughput ion irradiation experiments can be performed which traditionally would be infeasible.

Using this new high-temperature-capable, high-throughput irradiation system, dozens of Cr-Fe-Mn-Ni HEAs and CCAs have been irradiated using 4-MeV Ni^{2+} ions at 500 °C to a peak dose of 200 dpa. Samples from one additively manufactured compositional array, featuring alloys which exhibited primarily FCC microstructures, were shown to exhibit trends in swelling behavior that closely match historical ion

irradiation results from similar Cr-Fe-Ni alloys irradiated using Ni^{2+} ions. The trends indicate that swelling is greatly influenced by Cr content, whose increasing concentration leads swelling to increase monotonically, while swelling reaches a local maximum near ~25-30 at% Ni, after which swelling decreases with Ni additions. While swelling appears to only have a weak positive correlation with Mn content and virtually no dependence on Fe content, when examined in aggregate with other high-temperature, high-throughput irradiation data, it appears that some of the most pronounced swelling behavior occurs near the center of the composition space – contrary to what may be expected from trends from literature relating irradiation tolerance to compositional complexity. Many factors could contribute to this trend, including lower melting points of HEAs and CCAs compared to other less compositionally complex alloys which would cause the irradiation temperature to be at a higher homologous temperature leading to increased swelling since the irradiation temperature (500 °C) is likely on the lower end of the swelling curve for alloys in this system at such high dose rates. However, in addition to melting point, many other properties intrinsic to the alloy and many processing-dependent microstructural features may also play a significant role, and thus to progress this high-throughput methodology further, accelerated microscopy techniques combined with data analysis by machine learning are identified as promising directions for future work.

6 Concluding Remarks

To address design challenges for advanced nuclear reactors, and the challenges of sustainable energy production and environmental stewardship, new materials are needed. While the majority of alloy development historically has been focused on systems of few components and dilute concentrations, there is a vast untapped range of multi-principal-element alloys that have largely gone unexplored until the turn of the century. Several equimolar combinations of three, four, and five different elements have produced materials with promising properties, including high-temperature strength, high specific strength, and in some cases, a marked resistance to void swelling under irradiation. However, the vast range of alloy compositions, especially when considering non-equimolar alloys, makes exploration of this composition space using conventional experimental techniques temporally and fiscally intractable. The lack of large experimental databases spanning these ranges of alloy compositions also retards many modeling efforts, typically only leaving the more computationally expensive modeling techniques available – which still often rely on experimentally deduced potentials. Since experimental work to explore such alloys in both necessary and unavoidable, many researchers have turned to high-throughput synthesis techniques to rapidly produce samples of different alloy compositions, but unfortunately, many of these techniques do not produce materials with geometries, microstructures, or sufficient chemical homogeneity conducive for studies on irradiation performance. To fill this technological gap, the work presented herein details the efforts and achievements over the last five years developing a new high-throughput methodology for synthesizing, irradiating, and characterizing new alloy compositions. The following are highlights from each step of the process.

In situ Alloying via Additive Manufacturing

- Using a feedstock of elemental powders, arrays of different alloys compositions have been produced by additive manufacturing using a LENS MR-7.

- Through a process of composition calibration and the addition of remelting laser passes between layers, chemically homogeneous samples have been produced -typically within 5 at% of their target compositions.
- This new process has been used to produce hundreds of alloy compositions across different alloy systems including the Mo-Nb-Ta-W and Cr-Fe-Mn-Ni systems, among others.
- The high-throughput synthesis technique developed produces samples suitable for irradiation studies more than an order of magnitude faster than traditional synthesis techniques.

High-Throughput Phase Stability Assessment

- Using in situ alloying, 120 Cr-Fe-Mn-Ni samples were produced as 1-cm^2 samples several millimeters tall.
- The Cr-Fe-Mn-Ni sample arrays were heat treated for 24 hours at 1000 °C and an additional 24 hours at 700 °C, with laboratory XRD performed to identify the phases present after each step.
- For comparison, a Cr-Fe-Mn-Ni combinatorial thin film was heat treated at 500 °C for 4 hours, with phases identified using synchrotron XRD afterwards.
- Phases identified from the additively manufactured sample arrays were in agreement with CALPHAD predictions ~88% of the time while the CTF results were only in agreement ~27% of the time, likely due to the short heat treatment time.
- Even after the relatively short heat treatment, the CTF showed extensive microcracking and signs of delamination, while the additively manufactured arrays were still in excellent condition after longer heat treatments at higher temperatures.

Room-Temperature Ion Irradiation and Stage Development

- To fully utilize the parallelizable nature of the additively manufactured sample arrays, a stage system capable of accommodating the sample arrays was developed and installed in the middle beamline chamber at the UW-Madison Ion Beam Laboratory.

- The stage system is made entirely from stainless steel and positioned using stepper motors outside the chamber which minimizes sputtering and off-gassing making the stage amenable for irradiations over a wide range of temperatures while maintaining ultra-high vacuum conditions.
- To test the stage system and collect data on the irradiation behavior of select HEAs and CCAs, a sample array featuring every single element, equimolar binary alloy, equimolar ternary alloy in the Cr-Fe-Mn-Ni system was irradiated at room-temperature to a peak damage of 50 dpa.
- Nanoindentation was performed in the irradiated and unirradiated regions of each sample to measure changes in hardness due to irradiation.
- Many of the HEAs and CCAs were observed to have similar radiation-induced hardening (~1-1.5 GPa), however the Ni-rich FCC phase was observed to harden more than the Cr-rich BCC phase when the multiphase hardness data was analyzed in aggregate.

High-Temperature Ion Irradiation and Localized Heating System

- To perform high-temperature, high-throughput ion irradiations, an IR laser heating system was developed and installed in the UW-Madison Ion Beam Laboratory to heat samples individually while they are irradiated to preserve radiation-induced damage in adjacent samples.
- A LabView program (Chronos) was developed to automate stage motion, temperature measurement, laser heating, laser PID tuning, Faraday cup actuation, ion beam current measurement, and data logging enabling ion irradiations to be performed without user interaction.
- The new high-temperature-enabled, high-throughput irradiation system has been used to irradiate dozens of Cr-Fe-Mn-Ni HEAs and CCAs using heavy ions at 500 °C to a peak damage of 200 dpa.
- By covering a portion of each sample with a Mo mask, a sharp interface between the irradiated and unirradiated regions is produced, from which evidence of void swelling has been found using optical profilometry to measure the change in heigh across the interface.

- Cr additions were found to increase susceptibility to swelling while swelling appears to reach a maximum near 25-30 at% Ni, after which Ni additions led to a decrease in swelling; by comparison, Mn additions were found to weakly increase swelling while Fe additions had little effect.
- The trends in swelling measurements with composition from the high-temperature, high-throughput ion irradiation of the Cr-Fe-Mn-Ni sample array are in good agreement with historical data from Cr-Fe-Ni irradiations in 1974, which serves to validate the methodology.

As is discussed at the end of each chapter, there still remains much future work to be done. High-temperature, high-throughput ion irradiations using the systems developed herein are already planned for this remainder of this year and next, including irradiation campaigns of single compositions (e.g., Ni, or SS316) with varied irradiation parameters including, dose, dose rate, and temperature. Such experiments will not only serve to further validate and build confidence in the high-throughput methodology, but also produce high resolution swelling curves to provide rich datasets of swelling information over a range of possible reactor conditions. For the Cr-Fe-Mn-Ni alloys serving as the focus of this work, higher temperature irradiations are needed to promote greater amounts of swelling to better differentiate between alloy behavior, however, volatilization of Mn in these alloys at higher irradiation temperatures will likely require careful experiment planning to be addressed. While a global, comprehensive understanding of the compositional dependence of radiation damage and void swelling in HEAs and CCAs remains elusive within the research community, the tools developed here at UW-Madison and presented in this dissertation will enable the experiments to elucidate the answers to such questions.

7 Appendix

***Table 7.1**: Input RPMs, estimated incoming powder composition, printed sample composition measured via EDS, lattice parameter measured via XRD, and predicted lattice parameter from Vegard's law for each of the printed samples included in this study. Note the difference between input and actual powder hopper RPM, as this likely changes between systems and software versions. R(X).1 samples are from the first iteration, R(X).2 samples are from the second iteration, and BR(X) samples are from the third iteration. Also note that compositional predictions from the first iteration are increasingly prone to error at lower RPMs (e.g., sample R9.1) due to scatter in the mass flow rate measurements at low flow rates.*

		Input Powder Hopper RPM				Actual Powder Hopper RPM				Estimated Powder Composition (at%)				Measured Sample Composition (at%)				Lattice Parameter (Angstroms)	
Sample Index	Sample Name	Mo	Nb	Ta	W	Mo	Nb	Ta	W	Mo	Nb	Ta	W	Mo	Nb	Ta	W	Measured	Vegard's Law
1	R1.1	0.3	2.1	-0.4	2.2	2.7	1.7	2.2	1.8	46	10	32	12	21	27	27	24	3.218	3.203
2	R2.1	0.0	2.0	-0.4	2.8	2.5	1.6	2.2	2.2	41	8	32	19	18	22	28	31	3.216	3.198
3	R3.1	1.0	2.0	-0.4	2.2	3.3	1.6	2.2	1.8	51	8	30	11	27	24	25	24	3.214	3.227
4	R4.1	0.0	2.0	0.5	2.0	2.5	1.6	2.9	1.6	41	8	41	10	18	24	36	22	3.228	3.243
5	R5.1	1.0	2.5	-0.4	2.2	3.3	2.0	2.2	1.8	48	13	28	11	29	26	22	23	3.216	3.225
6	R6.1	0.0	2.5	0.5	1.8	2.5	2.0	2.9	1.4	40	14	40	7	20	28	33	18	3.233	3.213
7	R7.1	1.5	2.0	-0.8	2.2	3.7	1.6	1.9	1.8	56	8	25	11	31	28	17	24	3.214	3.221
8	R8.1	0.7	2.1	-0.4	2.5	3.1	1.7	2.2	2.0	47	9	30	15	23	24	25	28	3.220	3.227
9	R9.1	1.2	1.2	1.2	1.2	3.5	1.0	3.5	1.0	54	0	46	0	26	16	45	13	3.231	3.243
10	R10.1	0.7	2.5	-0.5	2.3	3.1	2.0	2.1	1.8	46	13	28	12	22	28	25	26	3.218	3.265
11	R1.2	-0.3	1.9	-0.2	2.4	2.3	1.5	2.3	1.9	40	8	36	15	19	38	15	28	3.218	3.233
12	R2.2	0.0	2.3	-1.1	2.5	2.5	1.8	1.6	2.0	44	13	26	16	21	42	9	28	3.224	3.230
13	R3.2	0.9	1.9	-1.4	2.3	3.2	1.5	1.4	1.8	56	7	22	14	32	36	4	28	3.209	3.214
14	R4.2	-0.2	2.3	-0.2	2.0	2.3	1.8	2.3	1.6	41	12	37	10	17	29	23	21	3.246	3.247
15	R5.2	0.6	1.9	-0.6	1.9	3.0	1.5	2.0	1.5	53	7	32	9	24	33	20	23	3.226	3.233
16	R6.2	0.9	2.2	-1.4	1.9	3.2	1.8	1.4	1.5	57	11	23	9	29	44	3	24	3.219	3.224
17	R7.2	1.6	1.8	-1.6	1.8	3.8	1.4	1.2	1.4	66	7	20	8	41	36	2	21	3.204	3.210
18	R8.2	0.0	2.7	-1.0	2.1	2.5	2.2	1.7	1.7	44	18	27	11	17	44	11	28	3.237	3.236
19	R9.2	-0.5	1.9	0.6	1.9	2.1	1.5	3.0	1.5	38	8	45	9	15	32	34	19	3.251	3.253
20	R10.2	-0.1	2.0	-1.1	2.9	2.4	1.6	1.6	2.3	43	9	26	22	17	38	10	35	3.217	3.226
21	R11.2	0.3	2.1	-0.8	2.2	2.7	1.7	1.9	1.8	49	10	29	12	21	34	18	27	3.222	3.231
22	BR2	-0.2	1.2	-0.6	2.2	2.3	1.0	2.0	1.8	25	28	18	29	18	28	26	28	3.228	3.235
23	BR3	0.5	0.5	-0.6	2.2	2.9	0.4	2.0	1.8	36	18	17	28	24	23	26	27	3.220	3.227
24	BR4	-0.2	1.2	0.0	1.5	2.3	1.0	2.5	1.2	25	28	27	20	18	24	39	20	3.231	3.247
25	BR5	0.6	0.5	-0.1	1.5	3.0	0.4	2.4	1.2	37	18	26	19	30	12	38	21	3.217	3.227
26	BR6	0.6	1.1	-0.6	1.4	3.0	0.9	2.0	1.1	37	27	17	19	28	27	29	15	3.236	3.236
27	BR7	1.3	0.5	-0.7	1.4	3.5	0.4	1.9	1.1	47	17	17	18	45	13	24	18	3.198	3.207
28	BR8	-0.2	1.8	-0.6	1.5	2.3	1.4	2.0	1.2	25	37	18	20	20	37	24	18	3.233	3.245
29	BR9	-0.2	0.6	0.6	1.5	2.3	0.5	3.0	1.2	25	19	36	20	20	15	45	19	3.239	3.244
30	BR10	-0.2	0.5	-0.6	3.0	2.3	0.4	2.0	2.4	25	18	18	39	16	12	30	42	3.208	3.219
31	BR11	0.2	0.8	-0.3	1.8	2.7	0.6	2.3	1.4	31	23	22	24	25	17	32	26	3.218	3.228

***Table 7.2**: Tabulated laser powers, target compositions, as-built compositions measured via EDS, measured compositions via XRF after homogenization, phases predicted by CALPHAD, and experimentally observed phases via XRD for each sample in the additively manufactured Cr-Fe-Mn-Ni compositional array.*

			Target Composition (at%)				As-Built Composition (at%)				Composition after Homogenization (at%)				Simulated at 1000 °C	After Homogenization
Sample #	Deposition Laser Power (W)	Remelt Laser Power (W)	Cr	Fe	Mn	Ni	Cr	Fe	Mn	Ni	Cr	Fe	Mn	Ni	Phases (CALPHAD)	Phases (XRD)
1	550	700	100	0	0	0	99.0	0.3	0.3	0.3	74.1	20.8	0.6	4.6	BCC	BCC
2	400	550	0	100	0	0	0.8	98.3	0.7	0.3	1.1	98.4	0.2	0.2	FCC	BCC
3	200	350	0	0	100	0	-	-	-	-	-	-	-	-	-	-
4	350	500	0	0	0	100	0.1	0.2	0.1	99.7	0.6	0.4	1.2	97.8	FCC	FCC
5	500	650	50	50	0	0	53.9	43.9	0.7	1.5	50.6	47.9	1.1	0.4	BCC	BCC
6	350	500	50	0	50	0	-	-	-	-	-	-	-	-	-	-
7	450	600	50	0	0	50	54.1	0.6	0.9	44.5	47.0	0.1	0.2	52.8	FCC+BCC	FCC
8	250	400	0	50	50	0	0.6	51.8	47.0	0.6	1.1	66.3	32.0	0.5	FCC	FCC+BCC
9	350	500	0	50	0	50	0.6	44.9	0.6	53.9	0.3	44.2	0.5	55.0	FCC	FCC
10	200	350	0	0	50	50	0.3	1.7	48.9	49.2	0.4	0.4	25.0	74.2	FCC	FCC
11	400	550	33	33	33	0	-	-	-	-	-	-	-	-	-	-
12	450	600	33	33	0	33	33.9	30.0	0.5	35.6	32.2	31.1	0.5	36.2	FCC	FCC
13	350	500	33	0	33	33	33.4	0.7	30.6	35.4	45.6	0.0	16.6	37.8	FCC+BCC	FCC+BCC
14	250	400	0	33	33	33	0.2	32.1	32.0	35.7	0.8	29.1	28.7	41.5	FCC	FCC
15	350	500	25	25	25	25	29.2	23.1	20.7	27.0	27.7	23.6	19.8	28.9	FCC	FCC+BCC
16	350	500	35	35	15	15	33.5	34.9	13.8	17.8	36.9	32.7	11.6	18.8	FCC+BCC	FCC+BCC
17	350	500	35	15	35	15	39.4	14.0	29.3	17.3	41.7	16.7	20.1	21.5	FCC+BCC	FCC+BCC
18	350	500	35	15	15	35	32.9	14.3	12.5	40.3	35.6	13.3	11.5	39.7	FCC+BCC	FCC+BCC
19	350	500	15	35	35	15	19.0	40.7	18.7	21.6	20.5	35.3	24.1	20.1	FCC	FCC
20	350	500	15	35	15	35	14.0	33.2	10.5	42.3	19.2	31.3	11.1	38.4	FCC	FCC
21	350	500	15	15	35	35	12.9	16.8	26.2	44.1	24.5	13.8	23.5	38.2	FCC	FCC
22	350	500	18	27	27	27	20.1	27.7	19.4	32.7	23.0	26.0	19.1	32.0	FCC	FCC
23	350	500	27	18	27	27	26.3	19.2	23.5	30.9	32.7	15.3	19.7	32.3	FCC+BCC	FCC+BCC
24	350	500	27	27	18	27	28.5	27.7	12.1	31.7	25.4	29.0	15.6	29.9	FCC	FCC+BCC
25	350	500	27	27	27	18	31.9	26.8	18.6	22.7	30.5	26.9	22.1	20.5	FCC+BCC	FCC+BCC

***Table 7.3**: Irradiation summary log output from Chronos following a 4-MeV Ni2+ irradiation of pure Fe to a peak damage of 200 dpa at 500 °C performed automatically.*

Index	3
Position Name	Sample 1
X(mm)	-116.25
Y(mm)	-67.73
Irradiate?	yes
Temperature (°C)	505
Target Fluence (ion/cm2)	2.04E+17
Aperture Area (cm2)	0.55
Ion Charge	2
Target Peak DPA	200
Target Plateau DPA	84.92
Start Time	8/9/2021 13:44
Time Under Irradiation (s)	6117.54
Current Measurement Time (s)	515.90
Pause Time (s)	49.55
End Time	8/9/2021 15:36
Total Time	00:01:51:23
Actual Fluence (ion/cm2)	2.04E+17
Min Current (uA)	0
Max Current (uA)	7.46
Average Current (uA)	4.79
Min Flux (ion/cm2/s)	2.58E+13
Max Flux (ion/cm2/s)	4.24E+13
Average Flux (ion/cm2/s)	2.72E+13
Min Peak DPA Rate (dpa/s)	2.53E-02
Max Peak DPA Rate (dpa/s)	4.15E-02
Average Peak DPA Rate(dpa/s)	2.67E-02
Min Plateau DPA Rate(dpa/s)	1.07E-02
Max Plateau DPA Rate(dpa/s)	1.76E-02
Average Plateau DPA Rate (dpa/s)	1.13E-02
Estimated Peak DPA	200.06
Estimated Plateau DPA	84.95
Min Temperature (°C)	496
Max Temperature (°C)	503
Average Temperature (°C)	502
Emissivity (0 to1)	0.267

***Table 7.4**: Beam current measurement log output from Chronos following a 4-MeV Ni2+ irradiation of pure Fe to a peak damage of 200 dpa at 500 °C performed automatically.*

Current Measurement Times	Delta Current Time (s)	Sample Flux (ions/cm2/s)	Integrated Fluence (ions/cm2)	Sample Peak DPA Rate (dpa/s)	Sample Average Plateau DPA Rate (dpa/s)
3:40:01 PM	0.00	4.17E+13	0.00E+00	4.09E-02	1.74E-02
3:50:07 PM	601.44	3.85E+13	2.41E+16	3.78E-02	1.61E-02
4:00:14 PM	601.50	3.62E+13	4.66E+16	3.56E-02	1.51E-02
4:10:21 PM	601.43	3.78E+13	6.89E+16	3.70E-02	1.57E-02
4:20:27 PM	601.24	3.30E+13	9.02E+16	3.24E-02	1.38E-02
4:30:34 PM	601.69	3.58E+13	1.11E+17	3.51E-02	1.49E-02
4:40:41 PM	601.73	4.03E+13	1.34E+17	3.95E-02	1.68E-02
4:50:48 PM	602.08	3.85E+13	1.57E+17	3.77E-02	1.60E-02
5:00:55 PM	601.82	3.84E+13	1.81E+17	3.77E-02	1.60E-02
5:11:02 PM	601.70	3.78E+13	2.04E+17	3.71E-02	1.57E-02
5:11:18 PM	10.56	3.60E+13	2.04E+17	3.53E-02	1.50E-02

***Table 7.5**: Tabulated high-temperature, high-throughput irradiation sample compositions and characterization results after irradiation with 4-MeV Ni^{2+} ions at 500 °C to a peak damage of 200 dpa.*

Sample Number	Cr (at%)	Fe (at%)	Mn (at%)	Ni (at%)	Unirradiated Phases (XRD)	Irradiated Phases (XRD)	Step Height (nm)	Calculated Swelling (%)
1	8.3	83.3	6.8	1.6	BCC	BCC	35 ± 7	1.94%
2	0.2	80.8	0	19	BCC	FCC+BCC	15 ± 4	0.83%
3	0.3	46.2	0	53.5	FCC	FCC	21 ± 5	1.17%
4	0.9	21.4	0	77.7	FCC	FCC	29 ± 5	1.61%
5	3.7	13.6	0.2	85.5	FCC	FCC	20 ± 4	1.11%
6	9.7	78.5	0.1	11.7	BCC	FCC+BCC	44 ± 9	2.44%
7	14.5	49.1	0.2	36.2	FCC	FCC	39 ± 2	2.17%
8	15.2	24.9	0.2	59.7	FCC	FCC	39 ± 4	2.17%
9	14.1	5.9	0.1	79.9	FCC	FCC	24 ± 4	1.33%
10	6.7	66.4	3.5	23.4	FCC	FCC	44 ± 2	2.44%
11	7.9	40.9	6.4	44.8	FCC	FCC	26 ± 3	1.44%
12	8	15.3	11.1	65.6	FCC	FCC	22 ± 4	1.22%
13	8.3	65.6	17.2	8.9	FCC	FCC	87 ± 8	4.83%
14	9.3	42.7	13.9	34.1	FCC	FCC	60 ± 9	3.33%
15	10	22.6	15.4	52	FCC	FCC	41 ± 4	2.28%
16	12.2	54.5	5.3	28	FCC	FCC	78 ± 3	4.33%
17	14.9	48.3	9.9	26.9	FCC	FCC	92 ± 1	5.11%
18	16.5	37.4	17.3	28.8	FCC	FCC	112 ± 7	6.22%
19	17	43.4	5.8	33.8	FCC	FCC	51 ± 3	2.83%
20	18.6	42.9	9.5	29	FCC	FCC	110 ± 6	6.11%
21	22.8	28.7	16.6	31.9	FCC	FCC	105 ± 2	5.83%
22	17.7	30.3	18.6	33.4	FCC	FCC	79 ± 6	4.39%
23	13.4	41.6	9.1	35.9	FCC	FCC	60 ± 2	3.33%
24	19.6	18.7	13.1	48.6	FCC	FCC	64 ± 9	3.56%
25	19.4	34	15.2	31.4	FCC	FCC	66 ± 4	3.67%

8 References

[1] WHO, Weekly operational update on COVID-19 - 6 September 2021, in: Emergency Situational Updates, World Health Organization, Online, 2021.
[2] CDC, COVID-19 Case Surveillance Public Data Access, Summary, and Limitations (version date: August 31, 2021), in: COVID-19 Response, Centers for Disease Control and Prevention, Online, 2021.
[3] IEA, Global Energy Review 2021: Assessing the effects of economic recoveries on global energy demand and CO2 emissions in 2021, in, International Energy Agency, Paris, 2021.
[4] IPCC, Climate Change 2021: The Physical Science Basis. Contribution of Working Group I to the Sixth Assessment Report of the Intergovernmental Panel on Climate Change, in, Intergovernmental Panel on Climate Change, Online, 2021.
[5] C. Bauer, K. Treyer, T. Heck, S. Hirschberg, Greenhouse Gas Emissions from Energy Systems, Comparison, and Overview☆, in: D.A. Dellasala, M.I. Goldstein (Eds.) Encyclopedia of the Anthropocene, Elsevier, Oxford, 2018, pp. 473-484.
[6] M. Taylor, Greenhouse gases and the nuclear fuel cycle: What emissions?, IAEA Bulletin, 39 (1997) 34-36.
[7] J. Duderstadt, L. Hamilton, Nuclear reactor analysis, in, 1976.
[8] GAO, Nuclear Fuel Reprocessing And The Problems Of Safeguarding Against The Spread Of Nuclear Weapons in: G.A. Office (Ed.), EMD-80-38, 1980.
[9] A. Hedin, Spent nuclear fuel - how dangerous is it? A report from the project 'Description of risk', in, Sweden, 1997, pp. 72.
[10] M. Sin, P. Oblozinsky, M. Herman, R. Capote, Fission cross section calculations of actinides with EMPIRE code, in, United States, 2010.
[11] R. MICHAL, Fifty years ago in December: Atomic reactor EBR-I produced first electricity, in: Nuclear News, American Nuclear Society, Online, 2001, pp. 28-29.
[12] D. Mohr, L.K. Chang, E.E. Feldman, P.R. Betten, H.P. Planchon, Loss-of-primary-flow-without-scram tests: Pretest predictions and preliminary results, Nuclear Engineering and Design, 101 (1987) 45-56.
[13] K.S. Krane, D. Halliday, Introductory nuclear physics, Wiley, New York, 1988.
[14] S.J. Zinkle, J.T. Busby, Structural materials for fission & fusion energy, Materials Today, 12 (2009) 12 - 19.
[15] A. Motta, A. Couet, R.J. Comstock, Corrosion of Zirconium Alloys Used for Nuclear Fuel Cladding, Annual Review of Materuals Research, 45 (2015) 311-343.
[16] F. Tanabe, Analyses of core melt and re-melt in the Fukushima Daiichi nuclear reactors, Journal of Nuclear Science and Technology, 49 (2012) 18-36.
[17] C. Kim, S. Jang, Y. Kim, FAST (floating absorber for safety at transient) for the improved safety of sodium-cooled burner fast reactors, Nuclear Engineering and Technology, 53 (2021) 1747-1755.
[18] R.B. Adamson, C.E. Coleman, M. Griffiths, Irradiation creep and growth of zirconium alloys: A critical review, Journal of Nuclear Materials, 521 (2019) 167-244.
[19] P.R. Morris, Irradiation Growth in Alpha-Uranium Single Crystals, Journal of Applied Physics, 33 (1962) 1611-1612.
[20] K. Nordlund, S.J. Zinkle, A.E. Sand, F. Granberg, R.S. Averback, R. Stoller, T. Suzudo, L. Malerba, F. Banhart, W.J. Weber, F. Willaime, S.L. Dudarev, D. Simeone, Improving atomic displacement and replacement calculations with physically realistic damage models, Nature Communications, 9 (2018) 1084.
[21] F.A. Garner, B.J. Makenas, S.A. Chastain, Swelling and creep observed in AISI 304 fuel pin cladding from three MOX fuel assemblies irradiated in EBR-II, Journal of Nuclear Materials, 413 (2011) 53-61.

[22] M. Bachhav, G. Robert Odette, E.A. Marquis, α′ Precipitation in neutron-irradiated Fe–Cr alloys, Scripta Materialia, 74 (2014) 48-51.
[23] F. Soisson, E. Meslin, O. Tissot, Atomistic modeling of α' precipitation in Fe-Cr alloys under charged particles and neutron irradiations: Effects of ballistic mixing and sink densities, Journal of Nuclear Materials, 508 (2018) 583-594.
[24] S.J. Zinkle, L.L. Snead, Designing Radiation Resistance in Materials for Fusion Energy, Annual Review of Materials Research, 44 (2014) 241-267.
[25] G.S. Was, P.L. Andresen, 3 - Mechanisms behind irradiation-assisted stress corrosion cracking, in: S. Ritter (Ed.) Nuclear Corrosion, Woodhead Publishing, 2020, pp. 47-88.
[26] W.S. Cunningham, J.M. Gentile, O. El-Atwani, C.N. Taylor, M. Efe, S.A. Maloy, J.R. Trelewicz, Softening due to Grain Boundary Cavity Formation and its Competition with Hardening in Helium Implanted Nanocrystalline Tungsten, Scientific Reports, 8 (2018) 2897.
[27] L.K. Mansur, Theory and experimental background on dimensional changes in irradiated alloys, Journal of Nuclear Materials, 216 (1994) 97-123.
[28] D.L. Porter, F.A. Garner, Irradiation creep and embrittlement behavior of AISI 316 stainless steel at very high neutron fluences, Journal of Nuclear Materials, 159 (1988) 114-121.
[29] F. Garner, Irradiation Performance of Cladding and Structural Steels in Liquid Metal Reactors, in: Materials Science and Technology, 2006.
[30] H. Wu, G. Niu, J. Cao, M. Yang, Annealing of strain-induced martensite to obtain micro/nanometre grains in austenitic stainless, Materials Science and Technology, 33 (2017) 480-486.
[31] X.H. Chen, J. Lu, L. Lu, K. Lu, Tensile properties of a nanocrystalline 316L austenitic stainless steel, Scripta Materialia, 52 (2005) 1039-1044.
[32] L. Heidari, M.J. Hadianfard, A.R. Khalifeh, D. Vashaee, L. Tayebi, Fabrication of nanocrystalline austenitic stainless steel with superior strength and ductility via binder assisted extrusion method, Powder Technology, 379 (2021) 38-48.
[33] G.R. Odette, M.J. Alinger, B.D. Wirth, Recent Developments in Irradiation-Resistant Steels, Annual Review of Materials Research, 38 (2008) 471-503.
[34] M.L. Lescoat, J. Ribis, Y. Chen, E.A. Marquis, E. Bordas, P. Trocellier, Y. Serruys, A. Gentils, O. Kaïtasov, Y. de Carlan, A. Legris, Radiation-induced Ostwald ripening in oxide dispersion strengthened ferritic steels irradiated at high ion dose, Acta Materialia, 78 (2014) 328-340.
[35] G.S. Was, D. Petti, S. Ukai, S. Zinkle, Materials for Future Nuclear Energy Systems, Journal of Nuclear Materials, 527 (2019) 151837.
[36] P. Hejzlar, R. Petroski, J. Cheatham, N. Touran, M. Cohen, B.A.O. Truong, R. Latta, M. Werner, T.O.M. Burke, J.A.Y. Tandy, M. Garrett, B. Johnson, T. Ellis, J.O.N. McWhirter, A.S.H. Odedra, P.A.T. Schweiger, D. Adkisson, J. Gilleland, Terrapower, LLC traveling wave reactor development program overview, Nuclear Engineering and Technology, 45 (2013) 731-744.
[37] R.N. Wright, Updated Draft ASME Boiler and Pressure Vessel Code Case for Use of Alloy 617 for Construction of Nuclear Components for Section III Division 5, in, United States, 2018.
[38] B. Cantor, I.T.H. Chang, P. Knight, A.J.B. Vincent, Microstructural development in equiatomic multicomponent alloys, Materials Science and Engineering: A, 375-377 (2004) 213-218.
[39] L.L. Xiao, Z.Q. Zheng, S.W. Guo, P. Huang, F. Wang, Ultra-strong nanostructured CrMnFeCoNi high entropy alloys, Materials & Design, 194 (2020) 108895.
[40] F. Zhang, Y. Wu, H. Lou, Z. Zeng, V.B. Prakapenka, E. Greenberg, Y. Ren, J. Yan, J.S. Okasinski, X. Liu, Y. Liu, Q. Zeng, Z. Lu, Polymorphism in a high-entropy alloy, Nature Communications, 8 (2017) 15687.
[41] J.W. Yeh, S.K. Chen, S.J. Lin, J.Y. Gan, T.S. Chin, T.T. Shun, C.H. Tsau, S.Y. Chang, Nanostructured High-Entropy Alloys with Multiple Principal Elements: Novel Alloy Design Concepts and Outcomes, Advanced Engineering Materials, 6 (2004) 299-303.
[42] W. Steurer, Single-phase high-entropy alloys – A critical update, Materials Characterization, 162 (2020) 110179.

[43] O.N. Senkov, S. Rao, K.J. Chaput, C. Woodward, Compositional effect on microstructure and properties of NbTiZr-based complex concentrated alloys, Acta Materialia, 151 (2018) 201-215.
[44] D.B. Miracle, Critical Assessment 14: High entropy alloys and their development as structural materials, Materials Science and Technology, 31 (2015) 1142-1147.
[45] T. Borkar, B. Gwalani, D. Choudhuri, C.V. Mikler, C.J. Yannetta, X. Chen, R.V. Ramanujan, M.J. Styles, M.A. Gibson, R. Banerjee, A combinatorial assessment of AlxCrCuFeNi2 ($0 < x < 1.5$) complex concentrated alloys: Microstructure, microhardness, and magnetic properties, Acta Materialia, 116 (2016) 63-76.
[46] Z. Wu, H. Bei, G.M. Pharr, E.P. George, Temperature dependence of the mechanical properties of equiatomic solid solution alloys with face-centered cubic crystal structures, Acta Materialia, 81 (2014) 428-441.
[47] S. Xia, C.M. Lousada, H. Mao, A.C. Maier, P.A. Korzhavyi, R. Sandström, Y. Wang, Y. Zhang, Nonlinear Oxidation Behavior in Pure Ni and Ni-Containing Entropic Alloys, Frontiers in Materials, 5 (2018).
[48] J.W. Yeh, Recent progress in high-entropy alloys, European Journal of Control, 31 (2006) 633 - 648.
[49] J.-W. Yeh, S.-Y. Chang, Y.-D. Hong, S.-K. Chen, S.-J. Lin, Anomalous decrease in X-ray diffraction intensities of Cu–Ni–Al–Co–Cr–Fe–Si alloy systems with multi-principal elements, Materials Chemistry and Physics, 103 (2007) 41-46.
[50] T. Löffler, H. Meyer, A. Savan, P. Wilde, A. Garzón Manjón, Y.-T. Chen, E. Ventosa, C. Scheu, A. Ludwig, W. Schuhmann, Discovery of a Multinary Noble Metal–Free Oxygen Reduction Catalyst, Advanced Energy Materials, 8 (2018) 1802269.
[51] C. Lu, T. Yang, K. Jin, N. Gao, P. Xiu, Y. Zhang, F. Gao, H. Bei, W.J. Weber, K. Sun, Y. Dong, L. Wang, Radiation-induced segregation on defect clusters in single-phase concentrated solid-solution alloys, Acta Materialia, 127 (2017) 98-107.
[52] D.B. Miracle, O.N. Senkov, A critical review of high entropy alloys and related concepts, Acta Materialia, 122 (2017) 448 - 511.
[53] E.P. George, D. Raabe, R.O. Ritchie, High-entropy alloys, Nature Reviews Materials, 4 (2019) 515-534.
[54] S. Guo, C.T. Liu, Phase stability in high entropy alloys: Formation of solid-solution phase or amorphous phase, Progress in Natural Science: Materials International, 21 (2011) 433-446.
[55] X. Yang, Y. Zhang, Prediction of high-entropy stabilized solid-solution in multi-component alloys, Materials Chemistry and Physics, 132 (2012) 233-238.
[56] Y. Zhang, Y.J. Zhou, J.P. Lin, G.L. Chen, P.K. Liaw, Solid-Solution Phase Formation Rules for Multi-component Alloys, Advanced Engineering Materials, 10 (2008) 534-538.
[57] Y. Dong, Y. Lu, L. Jiang, T. Wang, T. Li, Effects of electro-negativity on the stability of topologically close-packed phase in high entropy alloys, Intermetallics, 52 (2014) 105-109.
[58] D. King, Investigation of High-Entropy Alloys for use in Advanced Nuclear Applications, in, University of Technology Sydney, 2016.
[59] Z. Wang, Y. Huang, Y. Yang, J. Wang, C.T. Liu, Atomic-size effect and solid solubility of multicomponent alloys, Scripta Materialia, 94 (2015) 28-31.
[60] Z. Wang, W. Qiu, Y. Yang, C.T. Liu, Atomic-size and lattice-distortion effects in newly developed high-entropy alloys with multiple principal elements, Intermetallics, 64 (2015) 63-69.
[61] S. Guo, C. Ng, J. Lu, C.T. Liu, Effect of valence electron concentration on stability of fcc or bcc phase in high entropy alloys, Journal of Applied Physics, 109 (2011) 103505.
[62] W. Zhijun, S. Guo, C. T. Liu, Phase Selection in High-Entropy Alloys: From Nonequilibrium to Equilibrium, 2014.
[63] O.N. Senkov, G.B. Wilks, J.M. Scott, D.B. Miracle, Mechanical properties of Nb25Mo25Ta25W25 and V20Nb20Mo20Ta20W20 refractory high entropy alloys, Intermetallics, 19 (2011) 698-706.
[64] B. Gludovatz, A. Hohenwarter, D. Catoor, E.H. Chang, E.P. George, R.O. Ritchie, A fracture-resistant high-entropy alloy for cryogenic applications, Science, 345 (2014) 1153-1158.

[65] K.-C. Lo, Y.-J. Chang, H. Murakami, J.-W. Yeh, A.-C. Yeh, An oxidation resistant refractory high entropy alloy protected by CrTaO4-based oxide, Scientific Reports, 9 (2019) 7266.
[66] A.V. Kuznetsov, D.G. Shaysultanov, N.D. Stepanov, G.A. Salishchev, O.N. Senkov, Tensile properties of an AlCrCuNiFeCo high-entropy alloy in as-cast and wrought conditions, Materials Science and Engineering: A, 533 (2012) 107-118.
[67] Y. Xin, S. Li, Y. Qian, W. Zhu, H. Yuan, P. Jiang, R. Guo, L. Wang, High-Entropy Alloys as a Platform for Catalysis: Progress, Challenges, and Opportunities, ACS Catalysis, 10 (2020) 11280-11306.
[68] Y. Yuan, Y. Wu, X. Tong, H. Zhang, H. Wang, X.J. Liu, L. Ma, H.L. Suo, Z.P. Lu, Rare-earth high-entropy alloys with giant magnetocaloric effect, Acta Materialia, 125 (2017) 481-489.
[69] N.A.P.K. Kumar, C. Li, K.J. Leonard, H. Bei, S.J. Zinkle, Microstructural stability and mechanical behavior of FeNiMnCr high entropy alloy under ion irradiation, Acta Materialia, 113 (2016) 230-244.
[70] M.-R. He, S. Wang, K. Jin, H. Bei, K. Yasuda, S. Matsumura, K. Higashida, I.M. Robertson, Enhanced damage resistance and novel defect structure of CrFeCoNi under in situ electron irradiation, Scripta Materialia, 125 (2016) 5-9.
[71] S.Q. Xia, X. Yang, T.F. Yang, S. Liu, Y. Zhang, Irradiation Resistance in AlxCoCrFeNi High Entropy Alloys, JOM, 67 (2015) 2340-2344.
[72] K. Jin, C. Lu, L.M. Wang, J. Qu, W.J. Weber, Y. Zhang, H. Bei, Effects of compositional complexity on the ion-irradiation induced swelling and hardening in Ni-containing equiatomic alloys, Scripta Materialia, 119 (2016).
[73] S. Xia, M. Gao, T. Yang, P. Liaw, Y. Zhang, Phase stability and microstructures of high entropy alloys ion irradiated to high doses, Journal of Nuclear Materials, 480 (2016) 100 - 108.
[74] G.V. Y. Tong , S. Zhao , W. Guo , T. Yang, K. Jin, C. Lu, H. Bei, J.Y.P. Ko, D.C. Pagan, Y. Zhang, L. Wang, F.X. Zhang, Evolution of local lattice distortion under irradiation in medium- and high-entropy alloys, Acta Materialia, (2018) 1-9.
[75] O. El-Atwani, N. Li, M. Li, A. Devaraj, J.K.S. Baldwin, M.M. Schneider, D. Sobieraj, J.S. Wróbel, D. Nguyen-Manh, S.A. Maloy, E. Martinez, Outstanding radiation resistance of tungsten-based high-entropy alloys, Science Advances, 5 (2019) eaav2002.
[76] T. Yang, C. Li, S.J. Zinkle, S. Zhao, H. Bei, Y. Zhang, Irradiation responses and defect behavior of single-phase concentrated solid solution alloys, Journal of Materials Research, 33 (2018) 3077-3091.
[77] G.H. Kinchin, Pease, R.S., The displacement of atoms in solids by radiation, Reports on Progress in Physics, 18 (1955) 1.
[78] M.J. Norgett, Robinson, M.T. , Torrens, I.M. , A proposed method for calculating displacement dose rates, Nuclear Engineering and Design, 33 (1975) 50-54.
[79] P.K. Liaw, T. Egami, C. Zhang, F. Zhang, Y. Zhang, Radiation behavior of high-entropy alloys for advanced reactors. Final report, in, 2015.
[80] E.M. Criss, A.M. Hofmeister, Isolating lattice from electronic contributions in thermal transport measurements of metals and alloys above ambient temperature and an adiabatic model, International Journal of Modern Physics B, 31 (2017) 1750205.
[81] A.M. Stoneham, Energy transfer between electrons and ions in collision cascades in solids, Nuclear Instruments and Methods in Physics Research Section B: Beam Interactions with Materials and Atoms, 48 (1990) 389-398.
[82] F. Körmann, Y. Ikeda, B. Grabowski, M.H.F. Sluiter, Phonon broadening in high entropy alloys, npj Computational Materials, 3 (2017) 36.
[83] L.K. Béland, G.D. Samolyuk, R.E. Stoller, A. Caro, Lattice thermal conductivity of multi-component alloys, Journal of Alloys and Compounds, 648 (2015) 408 -413.
[84] L.K. Béland, C. Lu, Y.N. Osetskiy, G.D. Samolyuk, A. Caro, L. Wang, R.E. Stoller, Features of primary damage by high energy displacement cascades in concentrated Ni-based alloys, Journal of Applied Physics, 119 (2016) 085901.
[85] O.R. Deluigi, R.C. Pasianot, F.J. Valencia, A. Caro, D. Farkas, E.M. Bringa, Simulations of primary damage in a High Entropy Alloy: Probing enhanced radiation resistance, Acta Materialia, 213 (2021) 116951.

[86] S.V. Divinski, A.V. Pokoev, N. Esakkiraja, A. Paul, A Mystery of "Sluggish Diffusion" in High-Entropy Alloys: The Truth or a Myth?, Diffusion Foundations, 17 (2018) 69-104.
[87] K.Y. Tsai, M.H. Tsai, J.W. Yeh, Sluggish diffusion in Co–Cr–Fe–Mn–Ni high-entropy alloys, Acta Materialia, 61 (2013) 4887-4897.
[88] J. Dąbrowa, W. Kucza, G. Cieślak, T. Kulik, M. Danielewski, J.-W. Yeh, Interdiffusion in the FCC-structured Al-Co-Cr-Fe-Ni high entropy alloys: Experimental studies and numerical simulations, Journal of Alloys and Compounds, 674 (2016) 455-462.
[89] M. Vaidya, S. Trubel, B.S. Murty, G. Wilde, S.V. Divinski, Ni tracer diffusion in CoCrFeNi and CoCrFeMnNi high entropy alloys, Journal of Alloys and Compounds, 688 (2016) 994-1001.
[90] M. Vaidya, K.G. Pradeep, B.S. Murty, G. Wilde, S.V. Divinski, Radioactive isotopes reveal a non sluggish kinetics of grain boundary diffusion in high entropy alloys, Scientific Reports, 7 (2017) 12293.
[91] W. Kucza, J. Dąbrowa, G. Cieślak, K. Berent, T. Kulik, M. Danielewski, Studies of "sluggish diffusion" effect in Co-Cr-Fe-Mn-Ni, Co-Cr-Fe-Ni and Co-Fe-Mn-Ni high entropy alloys; determination of tracer diffusivities by combinatorial approach, Journal of Alloys and Compounds, 731 (2018) 920-928.
[92] Q. Li, W. Chen, J. Zhong, L. Zhang, Q. Chen, Z.-K. Liu, On Sluggish Diffusion in Fcc Al–Co–Cr–Fe–Ni High-Entropy Alloys: An Experimental and Numerical Study, Metals, 8 (2018) 16.
[93] K. Jin, C. Zhang, F. Zhang, H. Bei, Influence of compositional complexity on interdiffusion in Ni-containing concentrated solid-solution alloys, Materials Research Letters, 6 (2018) 293-299.
[94] S. Zhao, G.M. Stocks, Y. Zhang, Defect energetics of concentrated solid-solution alloys from ab initio calculations: Ni0.5Co0.5, Ni0.5Fe0.5, Ni0.8Fe0.2 and Ni0.8Cr0.2, Phys. Chem. Chem. Phys., 18 (2016) 24043-24056.
[95] S. Zhao, Defect properties in a VTaCrW equiatomic high entropy alloy (HEA) with the body centered cubic (bcc) structure, Journal of Materials Science & Technology, 44 (2020) 133-139.
[96] M. Jin, P. Cao, M.P. Short, Thermodynamic mixing energy and heterogeneous diffusion uncover the mechanisms of radiation damage reduction in single-phase Ni-Fe alloys, Acta Materialia, 147 (2018) 16-23.
[97] S. Zhao, T. Egami, G.M. Stocks, Y. Zhang, Effect of d electrons on defect properties in equiatomic NiCoCr and NiCoFeCr concentrated solid solution alloys, Physical Review Materials, 2 (2018) 013602.
[98] C. Lu, L. Niu, N. Chen, K. Jin, T. Yang, P. Xiu, Y. Zhang, F. Gao, H. Bei, S. Shi, M.-R. He, I.M. Robertson, W.J. Weber, L. Wang, Enhancing radiation tolerance by controlling defect mobility and migration pathways in multicomponent single-phase alloys, Nature Communications, 7 (2016) 13564.
[99] T.-n. Yang, C. Lu, K. Jin, M.L. Crespillo, Y. Zhang, H. Bei, L. Wang, The effect of injected interstitials on void formation in self-ion irradiated nickel containing concentrated solid solution alloys, Journal of Nuclear Materials, 488 (2017) 328-337.
[100] D.T.W. Fei, M.C. Gross, J.L. Lofgren, M. Mora-Worms, A.B. Chen, Cyclic AMP response to recombinant human relaxin by cultured human endometrial cells—A specific and high throughput in vitro bioassay, Biochemical and Biophysical Research Communications, 170 (1990) 214-222.
[101] G. Wu, S.K. Doberstein, HTS technologies in biopharmaceutical discovery, Drug Discovery Today, 11 (2006) 718-724.
[102] J.C. Zhao, X. Zheng, D.G. Cahill, High-throughput diffusion multiples, Materials Today, 8 (2005) 28-37.
[103] P. Wilson, R. Field, M. Kaufman, The use of diffusion multiples to examine the compositional dependence of phase stability and hardness of the Co-Cr-Fe-Mn-Ni high entropy alloy system, Intermetallics, 75 (2016) 15-24.
[104] A.D. Smigelskas, E.O. Kirkendall, Zinc diffusion in alpha brass, in: AIME Transactions, 1947, pp. 130-142.
[105] T. Gebhardt, D. Music, T. Takahashi, J.M. Schneider, Combinatorial thin film materials science: From alloy discovery and optimization to alloy design, Thin Solid Films, 520 (2012) 5491-5499.
[106] A. Marshal, K.G. Pradeep, D. Music, L. Wang, O. Petracic, J.M. Schneider, Combinatorial evaluation of phase formation and magnetic properties of FeMnCoCrAl high entropy alloy thin film library, Scientific Reports, 9 (2019) 7864.

[107] A. Akbari, T.J. Balk, Combinatorial thin film screening to identify single-phase, non-equiatomic high entropy alloys in the MnFeCoNiCu system, MRS Communications, 9 (2019) 750-755.
[108] H. Springer, D. Raabe, Rapid alloy prototyping: Compositional and thermo-mechanical high throughput bulk combinatorial design of structural materials based on the example of 30Mn–1.2C–xAl triplex steels, Acta Materialia, 60 (2012) 4950-4959.
[109] O.N. Senkov, D.B. Miracle, K.J. Chaput, J.-P. Couzinie, Development and exploration of refractory high entropy alloys—A review, Journal of Materials Research, 33 (2018) 3092-3128.
[110] Y. Shi, B. Yang, P. Liaw, Corrosion-Resistant High-Entropy Alloys: A Review, Metals, 7 (2017) 43.
[111] Y. Zhang, Preparation Methods of High-Entropy Materials, in: Y. Zhang (Ed.) High-Entropy Materials: A Brief Introduction, Springer Singapore, Singapore, 2019, pp. 65-75.
[112] S. Riva, S.G.R. Brown, N.P. Lavery, A. Tudball, K.V. Yusenko, Spark Plasma Sintering of High Entropy Alloys, in: P. Cavaliere (Ed.) Spark Plasma Sintering of Materials: Advances in Processing and Applications, Springer International Publishing, Cham, 2019, pp. 517-538.
[113] M. Vaidya, G.M. Muralikrishna, B.S. Murty, High-entropy alloys by mechanical alloying: A review, Journal of Materials Research, 34 (2019) 664-686.
[114] W. Li, P. Liu, P.K. Liaw, Microstructures and properties of high-entropy alloy films and coatings: a review, Materials Research Letters, 6 (2018) 199-229.
[115] A. Ludwig, R. Zarnetta, S. Hamann, A. Savan, S. Thienhaus, Development of multifunctional thin films using high-throughput experimentation methods, International Journal of Materials Research, 99 (2008) 1144 - 1149.
[116] P.J.S. Buenconsejo, A. Siegel, A. Savan, S. Thienhaus, A. Ludwig, Preparation of 24 Ternary Thin Film Materials Libraries on a Single Substrate in One Experiment for Irreversible High-Throughput Studies, American Chemical Society, 14 (2011) 25 - 30.
[117] T. Gebhardt, D. Music, T. Takahashi, J. Schneider, Combinatorial thin film materials science: From alloy discovery and optimization to alloy design, Thin Solid Films, 520 (2012) 5491 - 5499.
[118] D. König, J. Pfetzing-Micklich, J. Frenzel, A. Ludwig, Investigation of ternary subsystems of superalloys by thin-film combinatorial synthesis and high-throughput analysis, MATEC Web of Conferences, 14 (2014) 18002.
[119] D.C. Hofmann, J. Kolodziejska, S. Roberts, R. Otis, R.P. Dillon, J.-O. Suh, Z.-K. Liu, J.-P. Borgonia, Compositionally graded metals: A new frontier of additive manufacturing, Journal of Materials Research, 29 (2014) 1899-1910.
[120] P. Tsai, K.M. Flores, High-throughput discovery and characterization of multicomponent bulk metallic glass alloys, Acta Materialia, 120 (2016) 426-434.
[121] R.X. Li, P.K. Liaw, Y. Zhang, Synthesis of AlxCoCrFeNi high-entropy alloys by high-gravity combustion from oxides, Materials Science and Engineering: A, 707 (2017) 668-673.
[122] Y. Xu, Y. Bu, J. Liu, H. Wang, In-situ high throughput synthesis of high-entropy alloys, Scripta Materialia, 160 (2019) 44-47.
[123] M. Li, J. Gazquez, A. Borisevich, R. Mishra, K.M. Flores, Evaluation of microstructure and mechanical property variations in AlxCoCrFeNi high entropy alloys produced by a high-throughput laser deposition method, Intermetallics, 95 (2018) 110-118.
[124] D.J. Thoma, G.K. Lewis, R.B. Nemec, Solidification behavior during directed light fabrication, in, United States, 1995, pp. 7.
[125] O. Senkov, G. Wilks, J. Scott, D. Miracle, Mechanical properties of Nb25Mo25Ta25W25 and V20Nb20Mo20Ta20W20 refractory high entropy alloys, intermetallics, 19 (2011) 697 - 706.
[126] Y. Zou, S. Maiti, W. Steurer, R. Spolenak, Size-dependent plasticity in an Nb25Mo25Ta25W25 refractory high-entropy alloy, 2014.
[127] F. Körmann, M. Sluiter, Interplay between Lattice Distortions, Vibrations and Phase Stability in NbMoTaW High Entropy Alloys, Entropy, 18 (2016) 403.
[128] F. Körmann, A.V. Ruban, M.H.F. Sluiter, Long-ranged interactions in bcc NbMoTaW high-entropy alloys, Materials Research Letters, 5 (2017) 35-40.

[129] J.P. Oliveira, T.G. Santos, R.M. Miranda, Revisiting fundamental welding concepts to improve additive manufacturing: From theory to practice, Progress in Materials Science, 107 (2020) 100590.
[130] N.T. Aboulkhair, N.M. Everitt, I. Ashcroft, C. Tuck, Reducing porosity in AlSi10Mg parts processed by selective laser melting, Additive Manufacturing, 1-4 (2014) 77-86.
[131] J.B. Nelson, D.P. Riley, An experimental investigation of extrapolation methods in the derivation of accurate unit-cell dimensions of crystals, Proceedings of the Physical Society, 57 (1945) 160.
[132] L. Kaufman, H. Bernstein, Computer calculation of phase diagrams With special reference to refractory metals, Academic Press Inc, United States, 1970.
[133] U.R. Kattner, THE CALPHAD METHOD AND ITS ROLE IN MATERIAL AND PROCESS DEVELOPMENT, Tecnol Metal Mater Min, 13 (2016) 3-15.
[134] PanDat, Thermodynamic Calculations and Kinetic Simulations, in, CompuTherm LLC, 2019.
[135] H. Dobbelstein, M. Thiele, E.L. Gurevich, E. P.G., A. Ostendorf, Direct Metal Deposition of Refractory High Entropy Alloy MoNbTaW, Physics Procedia, 83 (2016) 624 - 633.
[136] D.A. Porter, K.E. Easterling, M.Y. Sherif, Phase transformations in metals and alloys, 2009.
[137] O. Senkov, G. Wilks, D. Miracle, C. Chuang, P. Liaw, Refractory high-entropy alloys, intermetallics, 18 (2010) 1758 - 1765.
[138] L.L. Parimi, R.G. A, D. Clark, M.M. Attallah, Microstructural and texture development in direct laser fabricated IN718, Materials Characterization, 89 (2014) 102-111.
[139] A. Raturi, J. Aditya C, N.P. Gurao, K. Biswas, ICME approach to explore equiatomic and non-equiatomic single phase BCC refractory high entropy alloys, Journal of Alloys and Compounds, 806 (2019) 587-595.
[140] R.J. Corruccini, J.J. Gniewek, Thermal expansion of technical solids at low temperatures; a compilation from the literature, U.S. Dept. of Commerce, National Bureau of Standards, Washington, 1961.
[141] L. Li, W.U.H. Syed, A.J. Pinkerton, Rapid additive manufacturing of functionally graded structures using simultaneous wire and powder laser deposition, Virtual and Physical Prototyping, 1 (2006) 217-225.
[142] H. Taheri, M.R.B.M. Shoaib, L.W. Koester, T.A. Bigelow, P.C. Collins, L.J. Bond, Powder-based additive manufacturing - a review of types of defects, generation mechanisms, detection, property evaluation and metrology, International Journal of Additive and Subtractive Materials Manufacturing, 1 (2017) 172-209.
[143] T. DebRoy, H.L. Wei, J.S. Zuback, T. Mukherjee, J.W. Elmer, J.O. Milewski, A.M. Beese, A. Wilson-Heid, A. De, W. Zhang, Additive manufacturing of metallic components – Process, structure and properties, Progress in Materials Science, 92 (2018) 112-224.
[144] A. Piglione, B. Dovgyy, C. Liu, C.M. Gourlay, P.A. Hooper, P. M.S., Printability and microstructure of the CoCrFeMnNi high-entropy alloy fabricated by laser powder bed fusion, Materials Letters, 224 (2018) 22 -25.
[145] S. Xiang, H. Luan, J. Wu, K.-F. Yao, J. Li, X. Liu, Y. Tian, W. Mao, H. Bai, G. Le, Q. Li, Microstructures and mechanical properties of CrMnFeCoNi high entropy alloys fabricated using laser metal deposition technique, Journal of Alloys and Compounds, 773 (2019) 387-392.
[146] J. Joseph, T. Jarvis, X. Wu, N. Stanford, P. Hodgson, D.M. Fabijanic, Comparative study of the microstructures and mechanical properties of direct laser fabricated and arc-melted AlxCoCrFeNi high entropy alloys, Materials Science and Engineering: A, 633 (2015) 184-193.
[147] H. Dobbelstein, E.L. Gurevich, E.P. George, A. Ostendorf, G. Laplanche, Laser metal deposition of a refractory TiZrNbHfTa high-entropy alloy, Additive Manufacturing, 24 (2018) 386-390.
[148] H. Dobbelstein, E.L. Gurevich, E.P. George, A. Ostendorf, G. Laplanche, Laser metal deposition of compositionally graded TiZrNbTa refractory high-entropy alloys using elemental powder blends, Additive Manufacturing, (2018).
[149] Y.H. Zhou, Z.H. Zhang, Y.P. Wang, G. Liu, S.Y. Zhou, Y.L. Li, J. Shen, M. Yan, Selective laser melting of typical metallic materials: An effective process prediction model developed by energy absorption and consumption analysis, Additive Manufacturing, 25 (2019) 204-217.

[150] W. Li, L. Yan, X. Chen, J. Zhang, X. Zhang, F. Liou, Directed energy depositing a new Fe-Cr-Ni alloy with gradually changing composition with elemental powder mixes and particle size' effect in fabrication process, Journal of Materials Processing Technology, 255 (2018) 96-104.
[151] A.B. Spierings, M. Voegtlin, T. Bauer, K. Wegener, Powder flowability characterisation methodology for powder-bed-based metal additive manufacturing, Progress in Additive Manufacturing, 1 (2016) 9-20.
[152] ASTM, Standard Practice for Investigating the Effects of Neutron Radiation Damage Using Charged-Particle Irradiation, in, 2018.
[153] R. Löbel, S. Thienhaus, A. Savan, A. Ludwig, Combinatorial fabrication and high-throughput characterization of a Ti–Ni–Cu shape memory thin film composition spread, Materials Science and Engineering: A, 481 - 482 (2008) 151 - 155.
[154] B. Cantor, I.T.H. Chang, P. Knight, A.J.B. Vincent, Microstructural development in equiatomic multicomponent alloys, Materials Science and Engineering: A, 375 - 377 (2004) 213 - 218.
[155] R. Kozak, A. Sologubenko, W. Steurer, Single-phase high-entropy alloys – an overview, in: Zeitschrift für Kristallographie - Crystalline Materials, 2015, pp. 55.
[156] B. Schuh, F. Mendez-Martin, B. Völker, E.P. George, H. Clemens, R. Pippan, A. Hohenwarter, Mechanical properties, microstructure and thermal stability of a nanocrystalline CoCrFeMnNi high-entropy alloy after severe plastic deformation, Acta Materialia, 96 (2015) 258-268.
[157] M. Elbakhshwan, W. Doniger, C. Falconer, M. Moorehead, C. Parkin, C. Zhang, K. Sridharan, A. Couet, Corrosion and Thermal Stability of CrMnFeNi High Entropy Alloy in Molten FLiBe Salt, Scientific Reports, 9 (2019) 18993.
[158] H. Chen, A. Kauffmann, S. Seils, T. Boll, C.H. Liebscher, I. Harding, K.S. Kumar, D.V. Szabó, S. Schlabach, S. Kauffmann-Weiss, F. Müller, B. Gorr, H.J. Christ, M. Heilmaier, Crystallographic ordering in a series of Al-containing refractory high entropy alloys Ta-Nb-Mo-Cr-Ti-Al, Acta Materialia, (2019).
[159] J.Q. Yao, X.W. Liu, N. Gao, Q.H. Jiang, N. Li, G. Liu, W.B. Zhang, Z.T. Fan, Phase stability of a ductile single-phase BCC Hf0.5Nb0.5Ta0.5Ti1.5Zr refractory high-entropy alloy, Intermetallics, 98 (2018) 79-88.
[160] R. Feng, P.K. Liaw, M.C. Gao, M. Widom, First-principles prediction of high-entropy-alloy stability, npj Computational Materials, 3 (2017) 50.
[161] D.J.M. King, P.A. Burr, E.G. Obbard, S.C. Middleburgh, DFT study of the hexagonal high-entropy alloy fission product system, Journal of Nuclear Materials, 488 (2017) 70-74.
[162] F. Tian, A Review of Solid-Solution Models of High-Entropy Alloys Based on Ab Initio Calculations, Frontiers in Materials, 4 (2017).
[163] C. Zhang, M.C. Gao, CALPHAD Modeling of High-Entropy Alloys, in: M.C. Gao, J.-W. Yeh, P.K. Liaw, Y. Zhang (Eds.) High-Entropy Alloys: Fundamentals and Applications, Springer International Publishing, Cham, 2016, pp. 399-444.
[164] F.G. Coury, P. Wilson, K.D. Clarke, M.J. Kaufman, A.J. Clarke, High-throughput solid solution strengthening characterization in high entropy alloys, Acta Materialia, 167 (2019) 1-11.
[165] S. Shukla, T. Wang, M. Frank, P. Agrawal, S. Sinha, R.A. Mirshams, R.S. Mishra, Friction stir gradient alloying: A novel solid-state high throughput screening technique for high entropy alloys, Materials Today Communications, 23 (2020) 100869.
[166] A. Ludwig, Discovery of new materials using combinatorial synthesis and high-throughput characterization of thin-film materials libraries combined with computational methods, npj Computational Materials, 5 (2019) 70.
[167] M. Moorehead, K. Bertsch, M. Niezgoda, C. Parkin, M. Elbakhshwan, K. Sridharan, C. Zhang, D. Thoma, A. Couet, High-throughput synthesis of Mo-Nb-Ta-W high-entropy alloys via additive manufacturing, Materials & Design, 187 (2020) 108358.
[168] B. Ruiz-Yi, J.K. Bunn, D. Stasak, A. Mehta, M. Besser, M.J. Kramer, I. Takeuchi, J. Hattrick-Simpers, The Different Roles of Entropy and Solubility in High Entropy Alloy Stability, ACS Combinatorial Science, 18 (2016) 596-603.

[169] C. Li, X. Hu, T. Yang, K.K. N.A.P., B.D. Wirth, S.J. Zinkle, Neutron irradiation response of a Co-free high entropy alloy, Journal of Nuclear Materials, 527 (2019) 151838.
[170] C. Parkin, M. Moorehead, M. Elbakhshwan, J. Hu, W.-Y. Chen, M. Li, L. He, K. Sridharan, A. Couet, In situ microstructural evolution in face-centered and body-centered cubic complex concentrated solid-solution alloys under heavy ion irradiation, Acta Materialia, 198 (2020) 85-99.
[171] K.M. Bertsch, G. Meric de Bellefon, B. Kuehl, D.J. Thoma, Origin of dislocation structures in an additively manufactured austenitic stainless steel 316L, Acta Materialia, 199 (2020) 19-33.
[172] A. Jacob, E. Povoden-Karadeniz, E. Kozeschnik, Revised thermodynamic description of the Fe-Cr system based on an improved sublattice model of the σ phase, Calphad, 60 (2018) 16-28.
[173] G. Laplanche, S. Berglund, C. Reinhart, A. Kostka, F. Fox, E.P. George, Phase stability and kinetics of σ-phase precipitation in CrMnFeCoNi high-entropy alloys, Acta Materialia, 161 (2018) 338-351.
[174] M. Strangwood, 6 - Fundamentals of ferrite formation in steels, in: E. Pereloma, D.V. Edmonds (Eds.) Phase Transformations in Steels, Woodhead Publishing, 2012, pp. 187-224.
[175] B. Sundman, Q. Chen, Y. Du, A Review of Calphad Modeling of Ordered Phases, Journal of Phase Equilibria and Diffusion, 39 (2018) 678-693.
[176] C. Günther, J. Vrijmoeth, R.Q. Hwang, R.J. Behm, Strain Relaxation in Hexagonally Close-Packed Metal-Metal Interfaces, Physical Review Letters, 74 (1995) 754-757.
[177] B. Roldan Cuenya, M. Doi, S. Löbus, R. Courths, W. Keune, Observation of the fcc-to-bcc Bain transformation in epitaxial Fe ultrathin films on Cu3Au(001), Surface Science, 493 (2001) 338-360.
[178] Y. Jiang, B. Wang, C. Xu, J. Zhang, Atomistic Simulation of the Strain Driven Phase Transition in Pure Iron Thin Films Containing Twin Boundaries, Metals, 10 (2020).
[179] M.A. Melia, S.R. Whetten, R. Puckett, M. Jones, M.J. Heiden, N. Argibay, A.B. Kustas, High-throughput additive manufacturing and characterization of refractory high entropy alloys, Applied Materials Today, 19 (2020) 100560.
[180] C. Manière, G. Lee, E.A. Olevsky, All-Materials-Inclusive Flash Spark Plasma Sintering, Scientific Reports, 7 (2017) 15071.
[181] P. Andrew, R. Hill, J. Gehin, D. Gougar, G. Strydom, F. Heidet, J. Kinsey, C. Grandy, A. Qualls, N. Brown, J. Powers, E. Hoffman, D. Croson, Advanced Demonstration and Test Reactor Options Study, in, Idaho National Lab., 2017.
[182] S. Taller, G. VanCoevering, B.D. Wirth, G.S. Was, Predicting structural material degradation in advanced nuclear reactors with ion irradiation, Scientific Reports, 11 (2021) 2949.
[183] Z. Yu, A. Couet, M. Bachhav, Irradiation-induced Nb redistribution of ZrNb alloy: An APT study, Journal of Nuclear Materials, 516 (2019) 100-110.
[184] S. Doriot, B. Verhaeghe, J.-L. Béchade, D. Menut, D. Gilbon, J.P. Mardon, J.-M. Cloué, A. Miquet, L. Legras, Microstructural evolution of M5™7 alloy irradiated in PWRs up to high fluences - Comparison with other Zr-based alloys, 2015.
[185] P. Scott, A review of irradiation assisted stress corrosion cracking, Journal of Nuclear Materials, 211 (1994) 101-122.
[186] J. Gan, D.D. Keiser, B.D. Miller, A.B. Robinson, D.M. Wachs, M.K. Meyer, Thermal stability of fission gas bubble superlattice in irradiated U–10Mo fuel, Journal of Nuclear Materials, 464 (2015) 1-5.
[187] C. Sun, Y. Gao, D.J. Sprouster, Y. Zhang, D. Chen, Y. Wang, L.E. Ecker, J. Gan, Disordering of helium gas bubble superlattices in molybdenum under ion irradiation and thermal annealing, Journal of Nuclear Materials, 539 (2020) 152315.
[188] R. Shimizu, S. Kobayashi, Y. Watanabe, Y. Ando, T. Hitosugi, Autonomous materials synthesis by machine learning and robotics, APL Materials, 8 (2020) 111110.
[189] F. Balbaud, C. Cabet, S. Cornet, Y. Dai, J. Gan, M. Hernández Mayoral, R. Hernández, A. Jianu, L. Malerba, S.A. Maloy, J. Marrow, S. Ohtsuka, N. Okubo, M.A. Pouchon, A. Puype, E. Stergar, M. Serrano, D. Terentyev, Y.G. Wang, A. Weisenburger, A NEA review on innovative structural materials solutions, including advanced manufacturing processes for nuclear applications based on technology readiness assessment, Nuclear Materials and Energy, 27 (2021) 101006.

[190] R.A. Roach, NMDQi Nuclear Materials Discovery and Qualification Initiative Conference Overview, in, United States, 2020.
[191] N. Teranishi, G. Fuse, M. Sugitani, A Review of Ion Implantation Technology for Image Sensors †, Sensors, 18 (2018) 2358.
[192] C. Schneider-Maunoury, L. Weiss, P. Acquier, D. Boisselier, P. Laheurte, Functionally graded Ti6Al4V-Mo alloy manufactured with DED-CLAD® process, Additive Manufacturing, 17 (2017) 55-66.
[193] N.A. Gokcen, The Mn-Ni (Manganese-Nickel) System, Journal of Phase Equilibria, 12 (1991) 313-321.
[194] A. International, Standard Practice for Neutron Radiation Damage Simulation by Charged-Particle Irradiation, E521 − 96 (Reapproved 2009), (2009).
[195] R.E. Stoller, M. Toloczko, G.S. Was, A. G. Certain, S. Dwaraknath, F. Garner, On the use of SRIM for computing radiation damage exposure, 2013.
[196] S. Gorsse, Senkov, O.N., About the Reliability of CALPHAD Predictions in Multicomponent Systems, Entropy, 20 (2018).
[197] X. Xiao, L. Yu, Nano-indentation of ion-irradiated nuclear structural materials: A review, Nuclear Materials and Energy, 22 (2020) 100721.
[198] R.E. Honig, VAPOR-PRESSURE DATA FOR THE SOLID AND LIQUID ELEMENTS, RCA Review, 23 (1962) 567.
[199] M. Li, K.M. Flores, Laser processing as a high-throughput method to investigate microstructure-processing-property relationships in multiprincipal element alloys, Journal of Alloys and Compounds, 825 (2020) 154025.
[200] L. Shao, J. Gigax, H. Kim, F.A. Garner, J. Wang, M.B. Toloczko, Carbon Contamination, Its Consequences and Its Mitigation in Ion-Simulation of Neutron-Induced Swelling of Structural Metals, in: J.H. Jackson, D. Paraventi, M. Wright (Eds.) Proceedings of the 18th International Conference on Environmental Degradation of Materials in Nuclear Power Systems – Water Reactors, Springer International Publishing, Cham, 2019, pp. 681-693.
[201] S.J. Zinkle, 1.03- Radiation-Induced Effects on Microstructure, Comprehensive Nuclear Materials, (2012) 66-93.
[202] A.F. Smith, R. Hales, Diffusion of Manganese in Type 316 Austenitic Stainless Steel, Metal Science, 9 (1975) 181-184.
[203] N. Sanaei, A. Fatemi, Defects in Additive Manufactured Metals and Their Effect on Fatigue Performance: A State-of-the-Art Review, Progress in Materials Science, (2020) 100724.
[204] S. Tammas-Williams, P.J. Withers, I. Todd, P.B. Prangnell, Porosity regrowth during heat treatment of hot isostatically pressed additively manufactured titanium components, Scripta Materialia, 122 (2016) 72-76.
[205] B.N. Singh, S.J. Zinkle, Defect accumulation in pure fcc metals in the transient regime: a review, Journal of Nuclear Materials, 206 (1993) 212-229.
[206] G.A. Kachurin, I.E. Tyschenko, L.I. Fedina, High-temperature ion implantation in silicon, Nuclear Instruments and Methods in Physics Research Section B: Beam Interactions with Materials and Atoms, 68 (1992) 323-330.
[207] G. Frech, W. Ensinger, H. Müller, M. Hans, G.K. Wolf, A multipurpose implanter with various target chambers for basic studies on the influence of ion bombardment on material properties, Nuclear Instruments and Methods in Physics Research Section B: Beam Interactions with Materials and Atoms, 68 (1992) 402-407.
[208] M.L. Crespillo, J.T. Graham, Y. Zhang, W.J. Weber, Temperature measurements during high flux ion beam irradiations, Review of Scientific Instruments, 87 (2016) 024902.
[209] B.H. Billings, D.E. Gray, American Institute of Physics handbook, McGraw-Hill, New York, 1972.
[210] G.W.C. Kaye, T.H. Laby, Tables of physical and chemical constants and some mathematical functions, 15th ed., Longman, London; New York, 1986.
[211] S. Takaki, J. Fuss, H. Kuglers, U. Dedek, H. Schultz, The resistivity recovery of high purity and carbon doped iron following low temperature electron irradiation, Radiation Effects, 79 (1983) 87-122.

[212] C.-C. Fu, J.D. Torre, F. Willaime, J.-L. Bocquet, A. Barbu, Multiscale modelling of defect kinetics in irradiated iron, Nature Materials, 4 (2005) 68-74.
[213] W. Van Renterghem, A. Al Mazouzi, S. Van Dyck, Influence of post irradiation annealing on the mechanical properties and defect structure of AISI 304 steel, Journal of Nuclear Materials, 413 (2011) 95-102.
[214] R.E. Stoller, S.I. Golubov, C. Domain, C.S. Becquart, Mean field rate theory and object kinetic Monte Carlo: A comparison of kinetic models, Journal of Nuclear Materials, 382 (2008) 77-90.
[215] K. Arakawa, K. Ono, M. Isshiki, K. Mimura, M. Uchikoshi, H. Mori, Observation of the One-Dimensional Diffusion of Nanometer-Sized Dislocation Loops, Science, 318 (2007) 956-959.
[216] S. Agarwal, Y. Lin, C. Li, R.E. Stoller, S.J. Zinkle, On the use of SRIM for calculating vacancy production: Quick calculation and full-cascade options, Nuclear Instruments and Methods in Physics Research Section B: Beam Interactions with Materials and Atoms, 503 (2021) 11-29.
[217] P. de Almeida, M. Victoria, Channeling effects in heavy-ion irradiated NiAl (100) single-crystals: a TEM assessment in cross-section geometry using weak-beam imaging, Solid State Communications, 125 (2003) 195-199.
[218] G. Velişa, K. Jin, Z. Fan, C. Lu, H. Bei, W.J. Weber, L. Wang, Y. Zhang, Multi-axial and multi-energy channeling study of disorder evolution in ion-irradiated nickel, Journal of Nuclear Materials, 525 (2019) 92-101.
[219] W.G. Johnston, J.H. Rosolowski, A.M. Turkalo, T. Lauritzen, A direct measurement of gross swelling in nickel-ion-bombarded stainless steel, Journal of Nuclear Materials, 46 (1973) 273-280.
[220] W.G. Johnston, J.H. Rosolowski, A.M. Turkalo, T. Lauritzen, An experimental survey of swelling in commercial Fe-Cr-Ni alloys bombarded with 5 MeV Ni Ions, Journal of Nuclear Materials, 54 (1974) 24-40.
[221] M. Moorehead, P. Nelaturu, M. Elbakhshwan, C. Parkin, C. Zhang, K. Sridharan, D.J. Thoma, A. Couet, High-throughput ion irradiation of additively manufactured compositionally complex alloys, Journal of Nuclear Materials, 547 (2021) 152782.